

FUSOGENIC LIPOSOME-ASSISTED DRUG DELIVERY ACROSS PHYSIOLOGICAL BARRIERS

Doctoral thesis

Submitted in partial fulfillment of the requirements for the degree of

Doctor rerum naturalium (Dr. rer. nat.)

of the

Faculty of Mathematics and Natural Sciences

of the

Rheinische Friedrich-Wilhelms-University Bonn

by

Tabea Wiedenhöft

from Marl

Bonn, 2021

Prepared with the permission of the Faculty of Mathematics and Natural Sciences of the
Rheinische Friedrich-Wilhelms-University Bonn.

1st referee: Prof. Dr. Rudolf Merkel

2nd referee: Prof. Dr. Ulrich Kubitscheck

Date of Submission: 3rd May 2021

Date of Oral Exam: 6th September 2021

Year of publication: 2021

1 Summary

Fusogenic liposomes (FL) are biocompatible, cationic nano-carriers, consisting of neutral and positively charged lipids, as well as an aromatic compound. They were previously used for the delivery of nucleic acids, proteins and functionalized lipids *in vitro*, highlighting their potential for drug delivery. Drugs and their delivery vehicles encounter a variety of interaction partners after administration. This includes components of the bloodstream and the vascular wall, as well as extracellular matrix (ECM) during tissue accumulation. Thus, an understanding of those interactions is highly relevant for FL-mediated drug delivery. In the present work, these interactions were investigated partially *in vitro* and *in vivo*, using epithelial cell lines and primary endothelial cells, as well as a mouse model of vascular aging.

FL enable the cell delivery of cargo by membrane fusion compared to commonly used liposomes using endocytosis. FL are thus permitting a direct release of cargo to the cytosol. The benefits of membrane fusion were investigated based on cargo localization inside the FL formulation and cargo basicity using confocal laser-scanning microscopy. Here, membrane fusion enabled passive uptake of membrane-impermeable cargo, although the latter was not entrapped in FL, presumably by induction of transient membrane pores. Additionally, anti-proliferative effects of anti-cancer therapeutics could be improved by direct release into the cytosol, if cargo was sensitive for lysosomal degradation due to higher basicity. This highlights the benefit of FL delivery for drugs with intracellular targets.

Basement membrane (BM) lesions and ECM remodeling are crucial markers for breast cancer progression. Nano-carriers that can adapt to the dynamically changing tumor matrix could therefore improve delivery of anti-cancer therapeutics. Interactions of FL with the ECM were thus examined in gels of ECM-relevant proteins. Furthermore, FL delivery was investigated in the MCF 10A acini model, mimicking breast acini with an adjustable BM, and spheroids of the highly invasive breast cancer cell line MDA-MB-231. Investigation of tracer dye uptake in the MCF 10A acini model using confocal laser-scanning microscopy and flow cytometry indicated a size-restrictive delivery of tracer dye. Furthermore, FL-mediated delivery of anti-cancer drug doxorubicin could improve anti-proliferative effects in comparison to commonly used liposomes if BM was lesioned or less matured. However, the passage of FL through ECM was vastly affected by opposed charges of FL and ECM, and protein secretion of the MDA-MB-231 spheroid model further reduced FL uptake. While this work demonstrated increasing drug

Summary

performance by FL delivery if BM is less matured, the formulation is still in need of further optimization to effectively traverse tumor matrix.

The ability to leave systemic circulation is highly relevant for tissue accumulation. It is critically affected by protein interactions and vascular permeability, which is vastly characterized by the endothelial cell barrier. In the present work, a model of the vascular endothelial barrier consisted of a primary human umbilical vein endothelial cell layer with two compartments to measure the passage of FL using fluorescence spectroscopy. Here, FL passage was increased if endothelial hyperpermeability was generated. Additionally, FL mediated the tracer dye delivery to endothelial cell layers, though membrane fusion was retarded by protein-liposome interactions.

Furthermore, the use of FL for endothelial delivery was evaluated. Pharmacologically relevant effects of the antioxidant resveratrol were investigated *in vitro* using fluorescence spectroscopy and plate reader measurements, as well as *in vivo* using laser speckle contrast imaging. Resveratrol delivery reduced an endothelial hyperpermeability *in vitro*, most likely due to the observed reduction of reactive oxygen species activity. *In vivo*, the adaptability of the vascular tone to neuronal stimulation could be rescued by FL-mediated resveratrol delivery in a mouse model of vascular aging.

In addition, biodistribution of FL was evaluated. The vascular delivery of liposomal tracer dye and cerebral circulation of FL were assessed by intravital imaging in a mouse model. Tracer dye was localized in the cerebral vasculature 1 h after injection of FL, with a decay after 24 h. Plate reader measurements of tracer dye fluorescence in dissected organs also demonstrated an accumulation of FL in the liver. Accordingly, FL clearance from the circulation within 24 h was postulated, presumably by hepatic elimination.

The present work provides a clearer understanding of FL interaction with the physiological barriers ECM and vascular wall. Steric and electrostatic interactions presumably modified FL passage through ECM *in vitro* and also modulated FL delivery and performance of drug cargo doxorubicin. Hyperpermeability increased FL passage through the endothelial barrier *in vitro*, indicating an enhanced permeability at target sites with leaky vasculatures. FL also enabled endothelial delivery of antioxidants *in vitro* and *in vivo* and are thus not only proposed as drug delivery vehicles for tissue accumulation in the periphery but for drug delivery to the vasculature, e.g., in cerebral endothelial dysfunction-related pathophysiology.

Table of Contents

1	<u>SUMMARY.....</u>	<u>1</u>
2	<u>ABBREVIATIONS</u>	<u>VI</u>
3	<u>INTRODUCTION</u>	<u>1</u>
3.1	NATURE OF LIPID BILAYERS AND THEIR APPLICATION FOR DRUG DELIVERY	2
3.1.1	BILAYER FORMATION AND CHARACTERISTICS.....	4
3.1.2	LIPOSOMES AS PHARMACEUTICAL VEHICLES	5
3.2	PHYSIOLOGICAL BARRIERS FOR BREAST CANCER PROGRESSION AND TREATMENT.....	11
3.2.1	EPITHELIAL TRANSITION TOWARDS MALIGNANCY	12
3.2.2	EXTRACELLULAR MATRIX INVOLVEMENT	13
3.3	THE ENDOTHELIAL BARRIER FOR MACROMOLECULE PASSAGE.....	16
3.3.1	ENDOTHELIAL BARRIER FORMATION AND COMPOSITION	16
3.3.2	ENDOTHELIAL REDOX BALANCE AND DYSFUNCTION	19
3.4	AIM OF THE THESIS	24
4	<u>MATERIAL AND METHODS.....</u>	<u>26</u>
4.1	MATERIAL	26
4.1.1	LIPIDS, LIPID DERIVATIVES AND DYES, AND LIPOSOME CARGO	26
4.1.2	CHEMICALS/KITS.....	29
4.1.3	OTHER CONSUMABLES	30
4.1.4	MEDIA AND BUFFERS	31
4.1.5	ANTIBODIES	33
4.1.6	INSTRUMENTS	33
4.1.7	SOFTWARE.....	34
4.2	METHODS	35
4.2.1	LIPOSOME FORMATION AND CHARACTERIZATION	35
4.2.2	CELL CULTURE AND ANIMAL HANDLING	39
4.2.3	IMAGING OF LIPOSOMAL TREATMENT AND PASSAGE	41
4.2.4	EVALUATION AND/OR QUANTIFICATION OF LIPOSOMAL CARGO AND DYE UPTAKE.....	45
4.2.5	QUANTIFICATION OF PHARMACOLOGICAL EFFECTS OF LIPOSOMAL CARGO.....	48
4.2.6	EVALUATION OF BIODISTRIBUTION OF FUSOGENIC LIPOSOMES	54
4.2.7	DATA ANALYSIS.....	56

5	<u>RESULTS</u>	<u>57</u>
5.1	IMPACT OF FUSOGENIC LIPOSOME-ASSISTED DELIVERY AT A CELLULAR LEVEL	58
5.1.1	PASSIVE ENTRY MEDIATED BY MEMBRANE FUSION	58
5.1.2	CIRCUMVENTION OF LYSOSOMAL SEQUESTRATION	60
5.2	FUSOGENIC LIPOSOME-ASSISTED DELIVERY ACROSS THE EXTRACELLULAR MATRIX	64
5.2.1	CULTURING OF THREE-DIMENSIONAL MODELS	64
5.2.2	PENETRATION OF THE BASEMENT MEMBRANE	67
5.2.3	FUSOGENIC LIPOSOME-ASSISTED DELIVERY OF ANTI-CANCER THERAPEUTICS	70
5.3	(TRANS-)ENDOTHELIAL DELIVERY MEDIATED BY FUSOGENIC LIPOSOMES	73
5.3.1	ESTABLISHMENT OF AN ENDOTHELIAL BARRIER MODEL	73
5.3.2	LIPOSOME PASSAGE THROUGH DYSFUNCTIONAL ENDOTHELIUM	74
5.3.3	FUSOGENIC LIPOSOME-ASSISTED DELIVERY OF RESVERATROL TO THE ENDOTHELIUM	77
5.4	FUSOGENIC LIPOSOME-ASSISTED DELIVERY BY SYSTEMIC ADMINISTRATION	79
5.4.1	IMPACT OF SERUM PROTEINS ON FUSOGENIC DELIVERY	79
5.4.2	BIODISTRIBUTION OF FUSOGENIC LIPOSOMES	80
5.4.3	FUNCTIONAL ASSESSMENT OF RESVERATROL IN FUSOGENIC LIPOSOMES <i>IN VIVO</i>	83
6	<u>DISCUSSION</u>	<u>86</u>
6.1	CONSIDERATIONS FOR FUSOGENIC LIPOSOMAL CARGO SELECTION	86
6.1.1	CIRCUMVENTION OF LYSOSOMAL CARGO SEQUESTRATION	87
6.1.2	TRANSIENT PERMEABILITY INDUCTION BY MEMBRANE FUSION	88
6.2	INTERACTIONS OF FUSOGENIC LIPOSOMES WITH EXTRA-CELLULAR MATRIX	91
6.2.1	CARGO UPTAKE MODIFIED BY LIPOSOME AND EXTRACELLULAR MATRIX INTERPLAY	91
6.2.2	CONSEQUENCES FOR DRUG DELIVERY	93
6.3	INTERACTIONS OF FUSOGENIC LIPOSOMES WITH VASCULAR ENDOTHELIUM AND THEIR BIODISTRIBUTION	96
6.3.1	EFFECTS OF ENDOTHELIAL BARRIER INTEGRITY	96
6.3.2	BIODISTRIBUTION OF FUSOGENIC LIPOSOMES	97
6.3.3	VASCULAR ENDOTHELIUM AS A THERAPEUTICAL TARGET	99
7	<u>CONCLUSION AND OUTLOOK</u>	<u>101</u>
8	<u>REFERENCES</u>	<u>104</u>
9	<u>FIGURES</u>	<u>118</u>
10	<u>TABLES</u>	<u>121</u>

11 **LIST OF PUBLICATIONS.....122**

2 Abbreviations

ACL	aclacinomycin a
AJ	adherens junction
BH4	tetrahydrobiopterin
BM	basement membrane
C4ase	collagenase IV
CAT	catalase
CH	cumene hydroperoxide
CM-H ₂ DCFDA	chloromethyl-2',7'-dichlorodihydrofluorescein diacetate
DMSO	dimethylsulfoxide
d	diameter
DOX	doxorubicin
ECM	extracellular matrix
EdU	5-ethynyl-20-deoxyuridine
EE	entrapment efficiency
EGF	epidermal growth factor
el	elution
EMT	epithelial-to-mesenchymal transition
eNOS	endothelial nitric oxide synthase
ER	estrogen receptor
FL	fusogenic liposomes
ft	flow through
FI	fluorescence intensity
hd	high-developed
HER2	human epidermal growth factor receptor 2
HUVECs	human umbilical vein endothelial cells
IGF	insulin-like growth factor
ld	low-developed
L-NAME	n ω - nitro-l-arginine methyl ester
LIPID MAPS	lipid metabolites and pathways strategy
miRNA	micro-RNA
MMP	matrix metalloproteinase

mtROS	mitochondrial reactive oxygen species
NO	nitric oxide
NOX	NADPH oxidase
Nrf-2	nuclear factor erythroid 2-related factor 2
PBS	phosphate-buffered saline
PEG	polyethylene glycol
PEG-EL	polyethylene glycol-coated, endocytic liposomes
PER	peroxidase
PDI	polydispersity index
PI	propidium iodide
ROS	reactive oxygen species
RSV	resveratrol
SIRT1	sirtuin-1
SOD	superoxide dismutase
TGF- β	transforming growth factor-beta
TJ	tight junctions
VE-Cad	vascular endothelial cadherin
VEGF	vascular endothelial growth factor
XOR	xanthine oxidoreductase
ZO-1	zonula occludens-1

3 Introduction

From the pioneering work in the 1970ies until today, drug delivery using nanoparticles has become a fundamental part of drug development, including technologies such as drug-conjugates with proteins, polymers, and antibodies; DNA- and polymer-drug complexes; micelles and liposomes. To date, over 50 nanomedicines are approved by the US food and drug administration, and the number of clinical trials has tripled from 2014 to 2017 (1). Prominent representatives of investigated nanomedicines are based on polymers and lipids. Especially the use of lipids for lipid nanoparticle formulation of mRNA vaccines against SARS-CoV-2 has emerged attention lately (2). Drug discovery is mandated to link the compound's molecular structure to its pharmacological effect. The design of drug delivery vehicles can be tailored to the active compound, administration route, and targeted tissue. Thus, this combinatorial freedom significantly accelerated the reformulation of already approved drugs with poor bioavailability, distribution, or immunogenicity (3, 4).

Systemically administered nanoparticles, as all endogenous macromolecules, encounter extra- and intracellular physiological barriers. Orally applied nanoparticles have to be absorbed by the intestinal barrier to enable distribution in the body. Intravenously applied and intestinally absorbed nanoparticles might encounter cells of the mononuclear phagocyte system. They can further be eliminated by renal or hepatic pathways. Nanoparticles need to leave the systemic circulation, commonly by extravasation, and enter the ECM of the recipient extravascular tissue. Additionally, they have to reach the site of action of the encapsulated cargo, which usually means the mediation of cellular uptake for intracellular drug targets. Hence, the application of nanoparticles in drug delivery adds even more complexity to the pharmacokinetics of an administered drug. Therefore, the formulation demands an extensive pre-clinical investigation, including physicochemical characterization, as well as efficacy, pharmacology and toxicology profiling. The investigation of interactions of the drug and its delivery system with the site of action is a substantial part of the drug development process. Thus, characterizing the interaction of nanoparticles with potential barriers on the way to the targeted epitope might enable increased combinatorial success to choose a suitable carrier delivering the drug to the site of action.

In the following subchapters, liposomes will be introduced as drug delivery vehicles. Malignant transition of breast epithelium and a dysfunctional vascular endothelium will be further

introduced with respect to pathophysiological contributions in disease onset well as their barrier properties concerning macromolecule passage and drug delivery.

3.1 Nature of lipid bilayers and their application for drug delivery

Lipids are ubiquitous biomolecules of living organisms. Though lipids share an amphiphilic scaffold, the diversity of their biological functions is expressed by the structural variety. A common classification of lipids was done by the Lipid Metabolites and Pathways Strategy (LIPID MAPS) consortium. Here, lipids are categorized by their structural backbone. Subsequently, eight categories emerged (**Figure 3.1**) that can be further subclassified (5).

Among these, glycerophospholipids are a category of amphiphilic molecule structures containing a glycerol backbone, though the polar head groups and the length and saturation of acyl chains can differ within different representatives (6). Glycerophospholipids are main components of biological membranes. An essential function of membrane lipids is the formation of the membrane bilayer, e.g., enabling energetic metabolism due to an electrochemical gradient at the mitochondrial membrane (7). Asymmetry of the lipid composition in the inner and outer leaflet of the cell membrane bilayer can further contribute to cellular signaling, e.g., by exposure of the glycerophospholipid phosphatidylserine on the surface of apoptotic cells, enabling immune cell recognition (8).

The packing of lipids inside the membrane bilayer is strongly affected by lipid geometry and the addition of sphingolipids and sterols such as cholesterol, which can further alter membrane fluidity. Sphingolipids are based on sphingosine, carbonyl-linked to acyl chains, and differing head groups. While glycerophospholipids frequently contain unsaturated fatty acid chains, sphingosine is mostly saturated. It is postulated that sphingolipids can form tightly packed lipid domains in the membrane in combination with sterols (9), mediating downstream signaling of membrane-associated proteins (10).

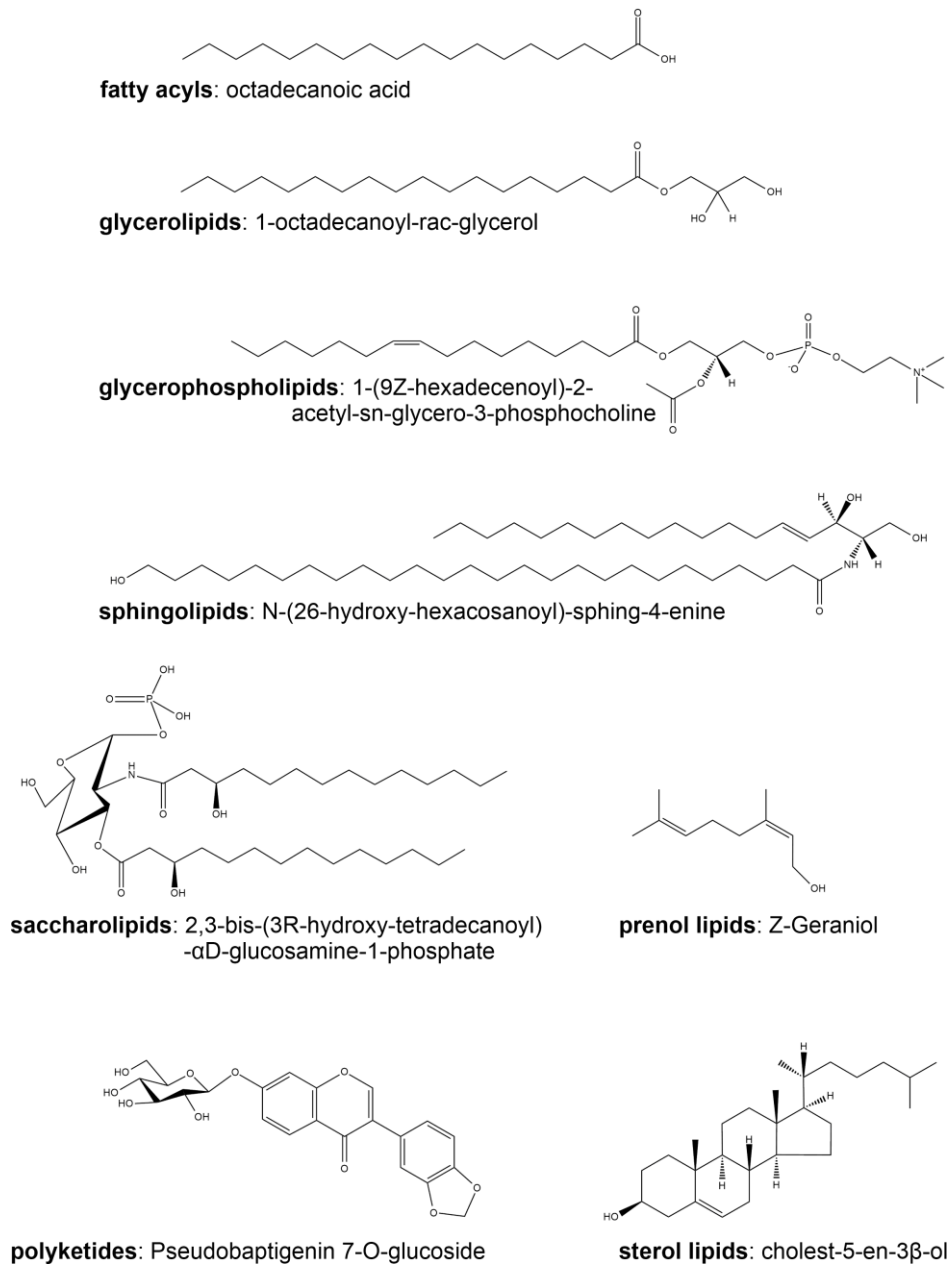


Figure 3.1. Representatives of lipid categories as proposed by the Lipid Metabolites and Pathways Strategy (LIPID MAPS) consortium. Systematic names of shown structures are given for each category.

3.1.1 Bilayer formation and characteristics

Though today, cell membranes of eukaryotic cells consist of a complex mixture of phospholipids, cholesterol, and membrane proteins, ancestral cell membranes most likely emerged from simple self-assembly of single-chained amphiphiles (11). The 'hydrophobic effect' describes the tendency of hydrophobic molecules to segregate from polar molecules (12). Amphiphilic lipids are partially hydrophilic and hydrophobic. Hence for lipids, the contact of the hydrophobic partial structure with an aqueous environment is minimized, e.g., by lipid bilayer assembly (13).

The molecular order of self-assembled lipids in an aqueous environment, the lipid phase, depends on the lipid structures, as well as the temperature of the solution and the hydration level of the self-assembly. While shorter, unsaturated acyl chains promote the lipid phase's fluidity, saturated acyl chains promote tight packing. Van der Waals interactions of acyl chains positively correlate with chain length, additionally enabling an ordered packing (14). Self-assembly of lipids can result in the formation of micelles and bilayers, behaving as lyotropic liquid crystals with, e.g., lamellar and hexagonal phases, amongst others (**Figure 3.2**).

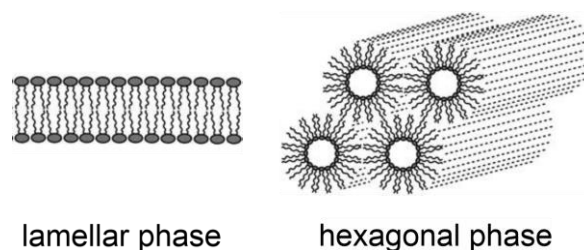


Figure 3.2. Schematic lipid assembly in lamellar and hexagonal phases. While cylindrically shaped lipids favor bilayer formation, cone-shaped lipids favor hexagonal phases due to their curvature evoking geometry. The figure is modified from (15).

The lamellar lipid phase is characterized by packing of lipids into bilayer sheets surrounded by an aqueous part. A further specification of lamellar phases is attributed to their polymorphic nature depending on the temperature and hydration level. At low water content and/or temperature, a crystalline phase can be formed, which resembles true crystals in long- and short-range, characterized by stiff lipid acyl chains and reduced lateral diffusion. An increase in temperature and water content can lead to the transition to gel-like and fluid phases,

characterized by an increase of rotational mobility of acyl chains and lateral diffusion. However, due to the polar head group's charge and geometry, different lipid phases are preferred. While the phosphocholine head group with cylindrical lipid geometry favors lamellar phase formation, smaller head groups, such as phosphoethanolamine, favor hexagonal phases with higher bilayer curvatures due to their conical lipid geometry (14). However, a mixture of hexagonal and lamellar phase preferring lipids can still form bilayers if there is enough present of the latter ones (16, 17).

3.1.2 Liposomes as pharmaceutical vehicles

Liposomes are spherical lipid bilayers enclosing an aqueous core. They were first observed using electron microscopy by Alec Bangham in 1964 (18). Early liposome research mainly focused on applying liposomes as biomimetic membrane models, making the fundamental properties of the membrane easily observable, such as water permeability and ion permeation (19, 20). Yet, the ability of liposomes to incorporate small molecules and deliver the cargo to mammalian cells was utilized shortly after, jumpstarting the entire field of colloidal drug delivery. This was highlighted by the first approval of a liposomal formulation of the anti-cancer drug doxorubicin in 1995 (21). To date, liposome technology still dominates approved nano-carrier-based drug formulations, improving bioavailability and biocompatibility of pharmacologically relevant substances with poor pharmacokinetics (22).

Liposomes can have one or several lipid bilayers and can encapsulate hydrophilic cargo in their aqueous core, while hydrophobic cargo can be incorporated into the lipid membrane (**Figure 3.3**). Another possibility for drug incorporation by liposomes is the functionalization of the lipid bilayer. Lipid modification can covalently link the liposomal bilayer to pharmacologically relevant antibodies, proteins, and other biomolecules. Surface functionalization of liposomes can reduce cargo leakage in the systemic circulation, e.g. by coating with polyethylene glycol (PEG) (23). Yet, it can also enable an active targeting of the recipient tissue, e.g., by ligand-dependent receptor binding. Currently, several liposomal formulations of anti-cancer drugs like doxorubicin are evaluated in clinical trials, e.g., targeting epitopes implicated in gastric and breast cancer (24-26).

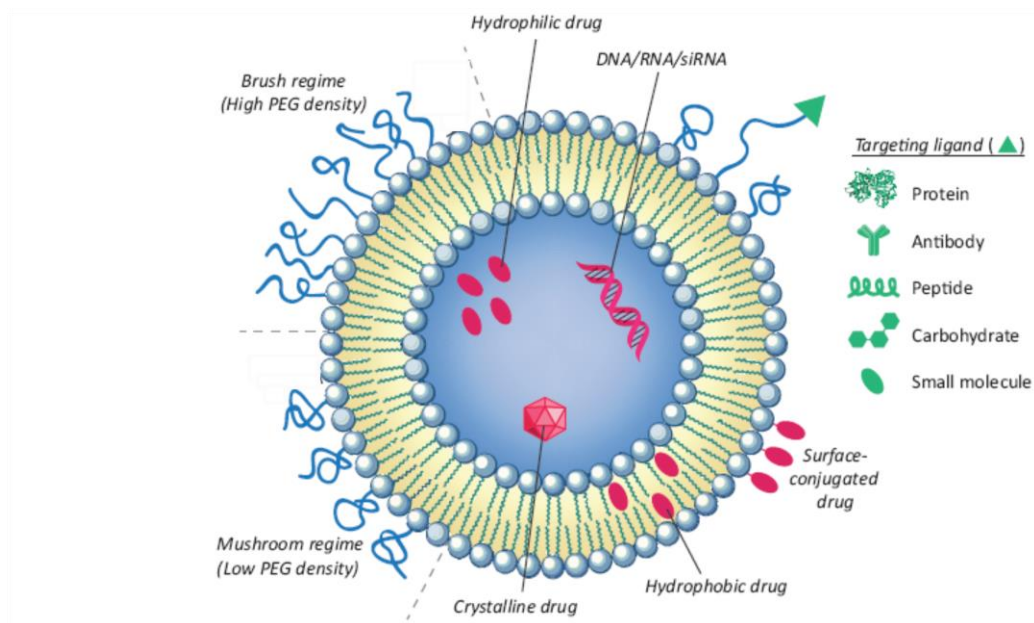


Figure 3.3. Different functionalizations of liposomes for drug delivery and diagnostics. Figure was modified from (27).

While a rapid metabolism or elimination of the pharmacologically active cargo can be decreased due to liposome encapsulation, the drug carrier was demonstrated to interact with the host defense system as well. Following systemic administration, liposomes are rapidly bound by circulating serum proteins forming a protein corona, which can be recognized by the mononuclear phagocyte system, enabling degradation of the drug carrier (28). The efficacy of drugs in conventional liposomes and liposomal active targeting drugs, which require proximity of drug carrier and targeted epitope, can be impeded by protein corona formation (29). The characteristics of the formed protein corona are heavily influenced by liposome composition, e.g., the incorporation of cholesterol, commonly added for bilayer stabilization, was demonstrated to increase binding of complement proteins, which are initiating liposomal clearance from the circulation (30). Subsequently, the liposomal formulation should not only consider an optimized interaction with the target site but favorable pharmacokinetics, frequently hampered by liposome protein interaction. Pegylation of liposomes and other biomolecules with pharmaceutical relevance was demonstrated to increase circulation half-life, therefore, enabling increased therapy performance by delayed systemic clearance.

The liposomal surface is often masked by conjugation to a biocompatible polymer to reduce the interaction with the mononuclear phagocyte system. This modification is referred to as 'stealth technology' (31). PEG is a water-soluble polymer widely used as a coating agent in

drug delivery. Owing to its hydrophilicity, PEG was introduced to reduce protein adsorption. Thus, a recognition by the immune system is avoided and circulation time can be prolonged (4). The surface density of PEG on the liposome surface can be modified by adjustment of the molar ratio of PEG to lipid. Increasing the polymer density by an amplified molar fraction ultimately results in a transition from a mushroom regime of single, non-interacting coils to a brush regime of interacting, stretched out chains with increased density and layer thickness. This transition is eventually destabilizing the liposomal bilayer and counteracting the intent of PEG modification (**Figure 3.3**) (32). Consequently, the molar fraction of PEG is critical for increased retention in circulation and the steric stabilization of the liposomal bilayer. Therefore, pharmaceutically relevant stealth liposomes predominantly contain <10 mol % PEG (21, 33).

The utilization of stealth liposomes as drug delivery vehicles has been broadly successful in cancer therapy. Here, therapy-related toxicities could be reduced compared to conventional drug formulations, as was demonstrated for Doxil, a formulation of stealth liposomes encapsulating doxorubicin (3, 4). Additionally, accumulation of liposomes by extravasation out of leaky tumor vasculature is described (enhanced permeability and retention effect) (34). While doxorubicin's safety profile was optimized, adverse reactions could be observed as well, including stealth liposome-induced complement activation and hypersensitivity reactions. After PEG treatment, IgM antibodies specific for PEG and PEG-primed T cells were found *in vivo* (35, 36). Additionally, IgE antibody-mediated allergy to PEG is discussed in the literature (37). As adverse reaction following treatment with Doxil, interaction of PEG and the host immune response is manifested as hand-foot syndrome, causing swelling, pain, and inflammation of hand palms and feet soles (38). The aforementioned studies suggest a protein interaction of stealth liposomes exists despite or even especially due to PEG modification. Though the stealth technology ultimately benefitted the safety profile of previously established drugs, drawbacks and adverse reactions remain, leaving room for innovative technologies.

3.1.2.1 Fusogenic liposomes

In the recent search for innovative drug delivery systems, the optimization of cellular cargo entry received more attention. While stealth liposomes are primarily entering cells by endocytosis, liposomal formulations recently emerged that can more efficiently deliver cargo

to the recipient cells, e.g., mediated by increased endosomal escape or membrane fusion as a cellular uptake mechanism. Here, current research has focused on temperature-, light-, and pH-sensitive, as well as FL (39-44). The latter are in focus of this thesis.



Figure 3.4. Schematic representation of fusogenic liposomes (FL). A schematic representation of the used FL composition is shown, consisting of neutral lipids and positively charged lipid derivatives in addition of a lipid dye. The scheme sketches the molecular composition and not the lipid phase of FL.

FL used in this work are three-component liposomes of neutral lipids, positively charged lipid derivatives, and aromatic molecules (**Figure 3.4**). The latter ones are either fluorophores like lipid dyes or substituted by the aromatic cargo that is to be delivered (41). Previous studies of the molecular composition of FL demonstrated that a lipid derivative of positive net charge and conical shape is required for membrane fusion (45), possibly owing to the need for close proximity to the negatively charged cell membrane. Thus, fusion is presumably enabled by electrostatic attraction and the probability of spontaneous curvature formation. Another required component is the aromatic molecule, although its function in fusion induction remains elusive (45). FL were first described as delivery vehicles of fluorescently labeled lipids into mammalian cells. Here, fusion enabled a direct membrane insertion of the lipid-coupled fluorophores (41). To date, the application of FL broadened to delivery of small molecules (46), proteins (47), nucleic acids, and radionuclides. These applications are relevant as biological tools, e.g., for the transfection of *in vitro* cultures with DNA and RNA (48), or as drugs, e.g., in cancer therapy (44, 49).

Membrane fusion can be mediated by proteins, as observed for cellular entry of viruses, or protein-independent if the liposomal composition enables fusion induction (45). Bilayer

curvature, which can be enabled by beneficial lipid shapes, plays an essential role in the fusion of one membrane with another. This is also postulated for the 'stalk mechanism' of membrane fusion (50). Here, the merging of two membranes requires the proximity of the apposed bilayers. The 'stalk mechanism' suggests a hemifusion of the outer leaflet of membranes in close distance, followed by the formation of a fusion pore (Figure 3.5). The ability of hemifusion and fusion pore formation most likely requires the membrane's ability to form spontaneous curvatures, as observed in the intermediate states of the postulated fusion process. While biologically observed fusion most often involves fusion mediators such as SNARE proteins (51), protein-independent fusion was described for bilayer of conically shaped lipids, enabled by lamellar/inverse phase transition (52). The fusion of lipid bilayers with the cell membrane, far more complex in structure, required the presence of conically shaped lipids. Further, a positive net charge and an aromatic chromophore seemed obligatory for efficient fusion of FL with the cell membrane, presumably due to its net negative charge (45). In contrast to commonly observed protein-dependent fusion of biological membranes, e.g. for viral cell entry, the fusion induced by FL with the cell membrane is protein-independent.

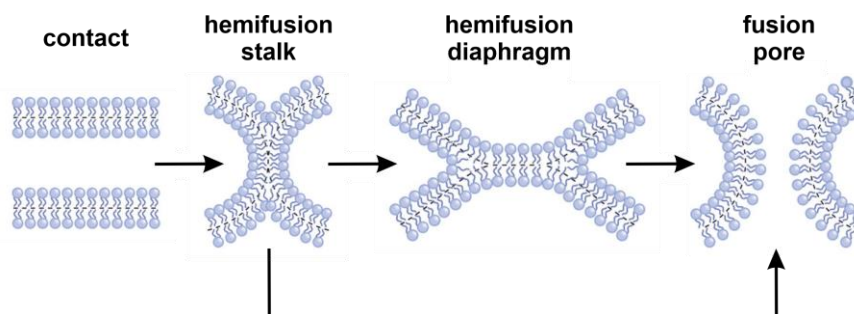


Figure 3.5. Proposed stalk mechanism of lipid bilayer fusion. Contact of apposed membranes is established, and the outer membrane leaflets fuse to form a hemifusion stalk, in which inner leaflets remain intact. The expansion of the outer leaflet merging and thus the membrane stalk yields a diaphragm. The formation of a fusion pore is characterized by the unification of volumes previously contained by each bilayer. The figure is modified from (53).

Cargo delivered to the recipient cell by membrane fusion is directly released into the cytosol, while the liposomal bilayer is merging with the cell membrane (Figure 3.6). Hence FL cargo does not enter the endosomal pathway. In endocytosis, macromolecules are engulfed by the cell membrane and trafficked along the endosomal pathway. The endosome content can be degraded by processing in lysosomes, as well as recycled or transcytosed to the extracellular

environment. Furthermore, it can be released into the cytosol. Most drugs in liposomal formulations depend on a release to the cytosol since their site of action is situated outside the endosomal machinery but inside the cell. Hence, the endocytosis-mediated uptake of drugs is prone to reduce the availability of the drug at the intracellular target site, thereby decreasing pharmacological effects and efficacy. Accordingly, cell uptake by membrane fusion might impact the therapeutic performance of drugs with poor intracellular availability.

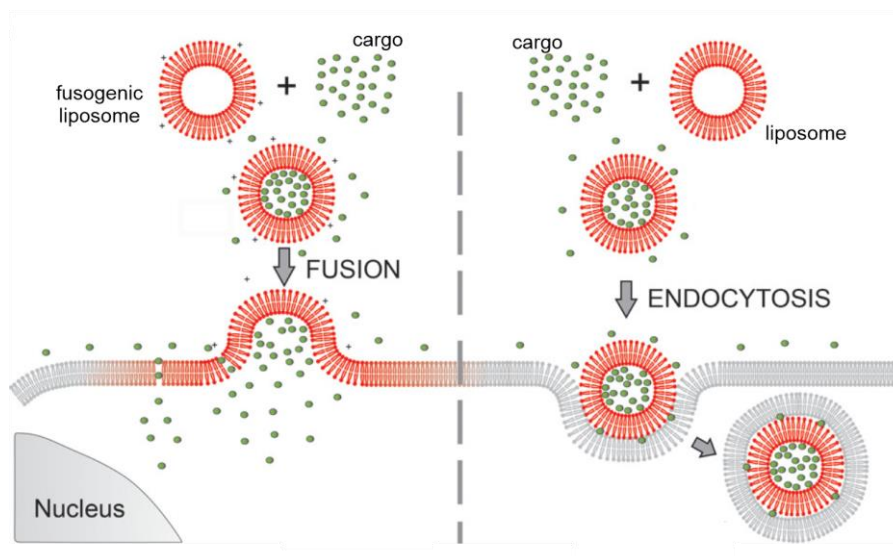


Figure 3.6. Comparison of cellular cargo uptake mediated by membrane fusion or endocytosis. During fusion, the membranes of fusogenic liposomes and the cell merge, enabling a direct release of cargo to the cytosol. If commonly used liposomes are taken up by endocytosis, they are engulfed by cell membrane, subsequently leading to endosomal trafficking and a possible lysosomal degradation of cargo. Figure was modified from (47).

3.2 Physiological barriers for breast cancer progression and treatment

In 2020, female breast cancer became the leading cause of global cancer incidence and the fifth leading cause of cancer mortality in both sexes combined (54). Due to its high frequency and subsequent mortality, breast cancer is a popular target for drug development. However, drug performance is largely affected by remodeling of the tumor environment. Thus, drug delivery vehicles are used to optimize therapeutic efficacy and side effects of already established anti-cancer therapeutics.

The mammary gland is a mammalian, exocrine gland specialized in lactation, i.e., the secretion of milk to nourish offspring. A schematic anatomical representation is visualized in **Figure 3.7**. The mammary gland's smallest organizational units are acinar alveoli, lined by a single layer of luminal, cuboidal epithelium and surrounded by myoepithelial cells. While mammary glands and the possibility of lactation and nursing define mammals morphologically, the mammary gland is also a frequent origin of malignancies and carcinoma. The latter originate from mammary epithelial cells.

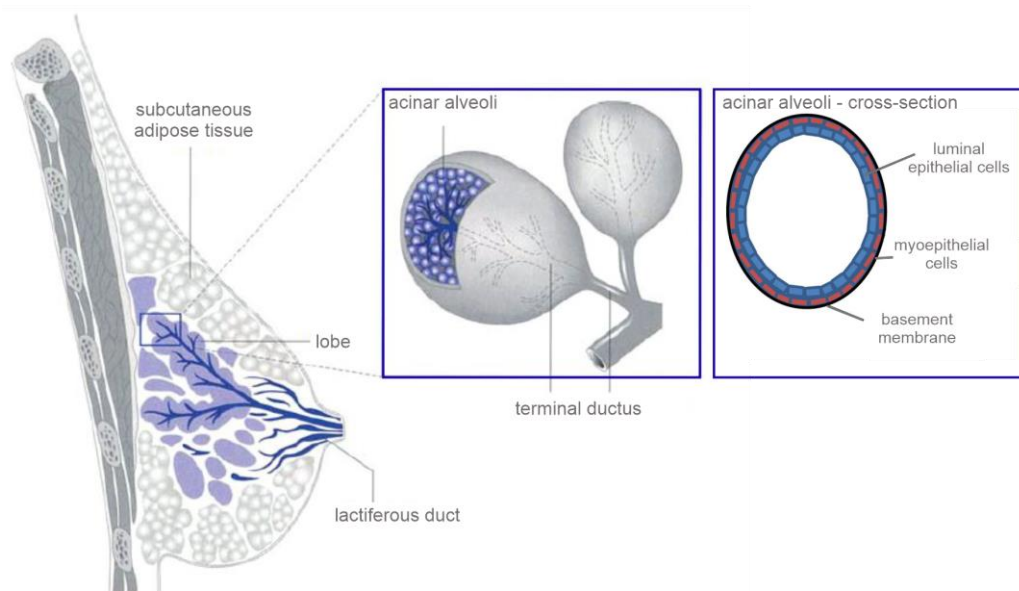


Figure 3.7. Anatomy of the human mammary gland. Several acinar alveoli are organized in lobes and connected by the terminal duct. Ducti are combined in the lactiferous duct draining into the nipple. The mammary gland is surrounded by connective and subcutaneous adipose tissue. Further a cross section of acinar alveoli is shown, displaying the layer of luminal epithelial cells, followed by myoepithelial cells and enclosed by a basement membrane. Figure is modified from (55) and (56).

3.2.1 Epithelial transition towards malignancy

The transition to malignancy is marked by cells acquiring autonomy of exogenously derived growth factors and insensitivity to anti-growth signals. This process subsequently leads to deregulated cell proliferation, paired with additional alterations of the telomere/telomerase machinery, enabling unlimited replicative potential. Additionally, genetic alterations can cause the evasion of apoptosis and subsequent inhibition of cell death. In malignant cells of breast epithelial origin, genes encoding proteins that modulate the cell cycle are most frequently altered.

Proliferative and pro-survival signaling in breast epithelial cells can arise from the hormones estrogen and progesterone by binding their respective nuclear receptors. Constitutive activity of the estrogen receptor ER α was prevalent in 60 % of breast cancer samples (57). In 13 -15 % of breast cancers, the ERBB2 gene encoding the HER2 receptor was amplified, leading to cell proliferation and survival (58). However, triple-negative breast cancer is clinically defined by the absence of estrogen, progesterone, and HER2 receptors, and a worse treatment prognosis than other subtypes (59). This is caused, among other reasons, by the resistance to commonly used anti-cancer therapeutics actively targeting above mentioned receptors, e.g., the selective estrogen receptor modulator tamoxifen (60). Consequently, the application of systemic chemotherapeutics, such as anthracyclines, is still part of the treatment regime for a variety of cancers. Here, therapy-related toxicities are minimized by modification of biodistribution using drug delivery vehicles (3, 4, 21).

While the endogenous ligand of the HER2 receptor remains unknown, a relative of the HER2 receptor, epidermal growth factor (EGF) receptor, is targeted by EGF and six additional ligands by paracrine signaling of stromal cells. EGF receptor activation is closely linked to cell proliferation, survival, and apoptosis by multi-faceted downstream signaling. EGF receptor is commonly overexpressed or constitutively activated in breast cancer, including triple-negative breast cancer. This can further dictate a poor prognosis of outcome (61), e.g., by promoting epithelial-to-mesenchymal transition, making breast cancer with altered EGF receptor signaling an attractive target of cancer research and respective drug development for breast cancer with poor prognosis.

Furthermore, to enable nutrient and oxygen supply to the tumor, vascularization can be established by the recruitment of endothelial cells triggered by expression of vascular

endothelial growth factor (VEGF). VEGF promotes endothelial cell migration into the tumor and the formation of new blood vessels and enhanced vascular permeability (62). Thus, EGF and VEGF are important growth factors for tumor progression.

3.2.2 Extracellular matrix involvement

Breast carcinoma are either classified as *in situ* carcinoma, which are non- or pre-invasive carcinoma residing in the ducti or lobes of the mammary gland; or invasive breast cancer, which is characterized by the invasion of malignant cells through the BM into the surrounding tissue. Therefore, the BM, which is lining epithelial cells of the ducti and lobes of the mammary gland, is a fundamental initial barrier for tumor cells to overcome and an important histological marker of breast cancer progressing from one class to another. The implications of BM integrity and thickness were further investigated in a three-dimensional *in vitro* model of breast acini (63, 64). Here, rupture of the BM and growth factor stimulation correlated with invasion onset (65).

The ECM is composed of the BM and the interstitial matrix. The interstitial matrix provides structural support and tensile strength to embedded epithelial tissue, and the former is mainly consisting of fibrillar collagen, fibronectin, and elastin. The connection of epithelial cells to the BM, separating epithelial cells from the interstitial matrix, is crucial for epithelial cell polarity and homeostasis. During tumorigenesis, the ECM is remodeled by additional deposition and chemical modification of pre-existing ECM. Tumorigenic remodeling of the ECM was previously described to limit the effectiveness of anti-cancer therapeutics by decreased tumor penetration depth (66). Thus, investigating the interaction of drugs and their delivery vehicles with the changing ECM is highly relevant in drug delivery and development. Consequently, establishing FL as drug delivery vehicles in cancer therapy requires a closer understanding of FL/ECM interactions.

3.2.2.1 Tumorigenic remodeling

Progression of breast cancer is linked to ECM stiffening based on increased deposition and crosslinking of ECM components by interplaying cancer cells, cancer-associated fibroblasts, and immune cells. In triple-negative breast cancer, an increased collagen deposition and matrix stiffening was found in human samples compared to non-invasive carcinoma. This

observed matrix remodeling was accompanied by an increased influx of pro-tumorigenic macrophages and presumed ECM deposition by cancer-associated fibroblasts (67, 68).

Furthermore, the ECM is also partially degraded, breaking down cell migration barriers and providing proliferative and migratory stimuli. The latter can be done by liberating ECM-bound growth factors, induced by matrix metalloproteinase (MMP) activity (69). Upregulation of BM component laminin 332 was reported in breast cancer lesions. EGFR-mediated MMP-2 activity was demonstrated to fragmentize laminin 332, exposing an EGF-like domain that can activate EGFR, creating a pro-migratory and pro-invasive positive feedback loop (70). Furthermore, MMP-2 and MMP-9 were demonstrated to degrade the collagen IV meshwork of the BM, while activation of heparanase is inducing heparan sulfate proteoglycan breakdown. This is further promoting ECM remodeling and subsequent invasion of neighboring tissue (71, 72).

3.2.2.2 Macromolecule passage across basement membranes

While the BM has a pivotal role as a restrictive barrier for cell migration and invasion in tumor progression, the ability of drugs to pass this barrier is of equal importance for treating epithelium-borne diseases, such as breast carcinoma. The BM is a three-dimensional protein meshwork of collagen IV and laminin, interconnected by proteins such as nidogen and perlecan, and heparan sulfate proteoglycans (73). Pore sizes of this meshwork were demonstrated to range from a few nanometers in the glomerular BM up to several micrometers in bronchial epithelium (74, 75), highlighting the variability of BM restrictiveness upon tissue specialization. Several studies indicate a molecular sieving effect of the BM, most prominently demonstrated for the glomerular BM, which separates endothelial cells and podocytes at the filtration site in the renal glomerulus (76). Here, it was postulated that the gel-like BM restricts size-dependent macromolecule passage through the meshwork by diffusion according to the gel permeation principle (77), experimentally supported by retardation of macromolecule permeation in correlation with their molecular weight and radii (78-80).

The diffusion of particles through the BM, and ECM in general, is influenced by steric interactions as previously mentioned. Yet, diffusion can also be hindered by electrostatic interactions of charged particles and ECM components. Heparan sulfate proteoglycans presumably determine the BM's negative charge (81). Particle binding by heparan sulfate proteoglycans previously indicated a decrease of effective diffusivity (82, 83). For the well-

investigated glomerular capillary wall, negative charge within the glomerular BM is discussed to form a barrier to anionic macromolecule passage. This is supported by accumulation of cationic ferritins at sub-endothelial layers of the glomerular BM in comparison to anionic ferritins *in vivo* (84), possibly due to electrostatic attraction to the anionic sites. Yet, a similar charge selectivity for spherical Ficoll and Ficoll sulfate particles was not observed in isolated, glomerular BM (85). Furthermore, electrostatic repulsion was proposed to affect diffusivity of particles in addition of hydrodynamic effects (86). However, in matrices with large fibers, such as collagen, this effect was proposed negligible. This is in accordance with recent theoretical and experimental studies focusing on the determination of diffusion coefficients of probe molecules diffusing hydrogels (87). Here, particle diffusion was significantly hindered by electrostatic attraction and not electrostatic repulsion. Thus, interactions of particles with the ECM are highly complex and require an investigation specific for the vehicle, which is to be utilized for drug delivery, and ECM of the targeted tissue.

As briefly mentioned in **3.2.2.1**, heparan sulfate proteoglycan breakdown promotes ECM remodeling and progression of invasion in breast cancer, thus, affecting the anionic sites in the tumor stroma. Yet, the implication of altered charges within the ECM for macromolecule passage in breast cancer remains elusive. Furthermore, lesions of the epithelial BM in breast cancer decrease the 5-year survival rate from 99 % to 85 % (88). While the breakdown of ECM is promoted by MMPs and heparanase, a proposed mode for a protease-independent invasion of the BM utilizes its mechanical viscoplasticity. A physical force-driven widening of the BM mesh is enabled by invasive cancer cells (89). The perforation of the BM by proteases and physical force was demonstrated to enable cellular passage for invasion; however, its relevance for macromolecule passage and drug delivery is also not yet understood.

3.3 The endothelial barrier for macromolecule passage

The vessel wall is lined by vascular endothelium in all organ beds, mediating tissue-to-fluid homeostasis by vascular tone regulation and macromolecule entry as well as cellular transmigration restriction. During *de novo* vasculogenesis in embryonal development, endothelial cells differentiate from mesoderm-derived angioblasts. This process is to an extent mediated by VEGF, to form blood vessels by further recruitment of mesenchymal cells, mediated by angiopoietin-1, platelet-derived growth factors, and heparin-binding EGF (90-92). In a TGF- β dependent manner, the mesenchymal progenitors can differentiate into smooth muscle cells and pericytes, accompanied by matrix deposition and reduced proliferation of endothelial cells (92, 93). The cardiovascular system is the first functional system during embryonal development. Still, angiogenesis, the growth of vessels from pre-existing vasculature, is relevant throughout the organism's lifetime. Angiogenesis enables the adaptation of nutrient availability to metabolic activity of each specific tissue. While the endothelial barrier is of high importance for the nutrient restriction and supply, it can further regulate the elimination of metabolites, e.g., at the glomerular wall. Exogenous macromolecules, such as drug delivery systems, face this barrier as well. Within the following chapter, the structure of the endothelial barrier and its relevance in health and disease will be introduced, followed by the relevance of a (dys)functional vasculature for drug development and delivery.

3.3.1 Endothelial barrier formation and composition

The vessel wall is structured into three layers from the luminal to basolateral site: *tunica intima*, *tunica media*, and *tunica adventitia* (94, 95). The thinnest layer, *tunica intima*, consists of a layer of endothelial cells supported by an underlying BM, followed by a connective tissue layer with pericytes near the endothelial cells and an internal lamina. *Tunica media* varies in composition and size respective to the vessel function but mainly consists of elastic fibers and residing smooth muscle cells, executing vascular contractility. The outer layer of the vessel wall, *tunica adventitia*, is innervated by the sympathetic nervous system and its composition vastly depends on vessel size (95, 96). Due to the lining of the luminal site of the vessel wall, the integrity of the endothelial monolayer is highly relevant for the permeability restriction of macromolecules from blood to the surrounding tissue.

3.3.1.1 Intercellular junctions

Endothelial cells are connected to adjacent cells by intercellular junctions, namely tight, adherens, and gap junctions. The relevance of adherens junctions (AJ) and tight junctions (TJ) for the restrictiveness of the endothelial barrier has been characterized (97, 98), while gap junctions provide the ability for electrical and chemical communication within the endothelial monolayer and with smooth muscle cells for vascular tone synchronization (99, 100). The structure of cellular junctions characterizing the endothelial barrier function is schematically presented in **Figure 3.8**.

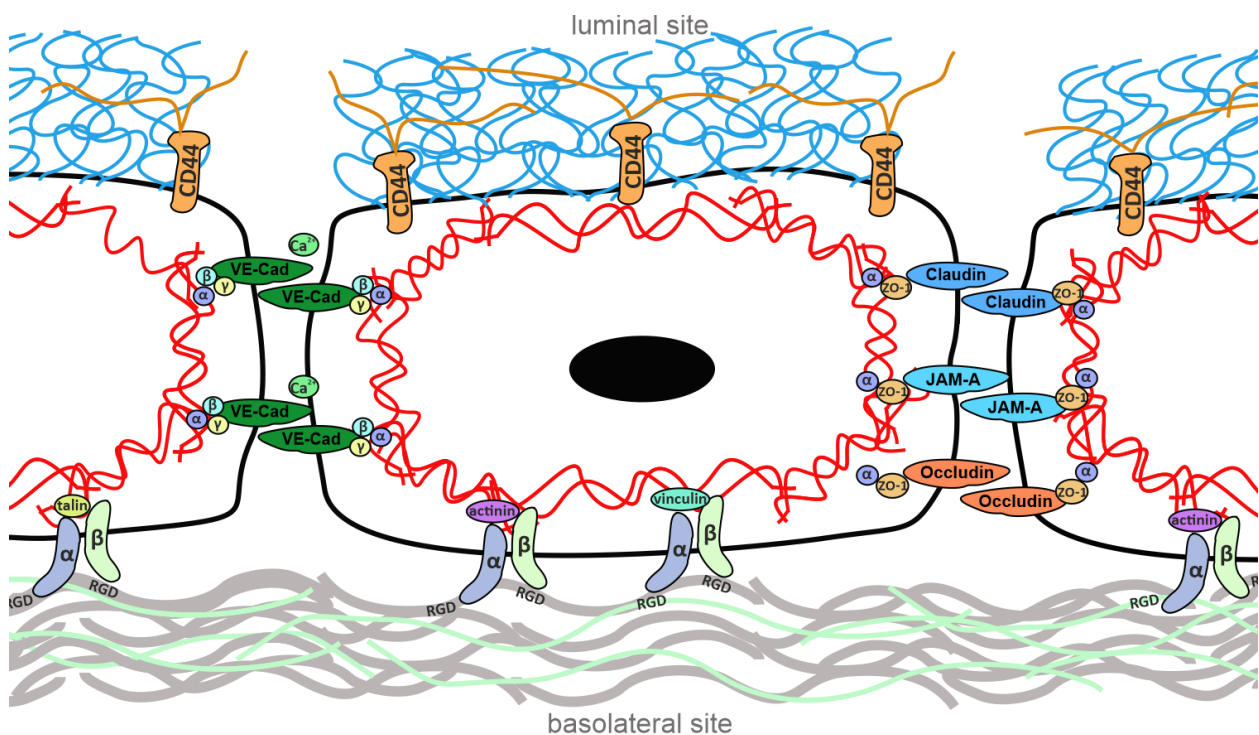


Figure 3.8. Schematic representation of endothelial junctions to adjacent cells, the extracellular matrix, and the glycocalyx. The formation of adherens junctions by homotypic binding of VE-cadherin (VE-Cad) is calcium-dependent. VE-Cad is connected to β - and γ -catenins, which link to the actin cytoskeleton via α -catenin. Tight junctions are formed by homotypic binding of adjacent endothelial cells by claudin, occludin, or JAM-A. Zonula occludens-1 (ZO-1) serves as a scaffolding protein, which connects tight junctions to the actin skeleton via α -catenin. Endothelial cells are attached to the extracellular matrix by α -/ β -heterodimeric integrins that can bind the RGD-motif of proteins of the extracellular matrix. Intracellularly, integrins can be connected to the actin cytoskeleton by actinin, talin, or vinculin. On the endothelial cell's luminal site, proteoglycans are anchoring the glycocalyx in the cell membrane, and CD44 binds to hyaluronan. In this figure, the representation of endothelial cell connections is reduced to junctions involved in the endothelial cell layer's barrier function.

The composition of intercellular junctions dictates the paracellular permeability of the endothelial cell layer. AJ are linked with cortical actin that forms a ring-like structure in the cell periphery. Respective to the tissue-specialized endothelium, TJ are connected with the actin cytoskeleton as well; however, continuous TJ are predominantly found in specialized tissue with highly restrictive characteristics, as for instance the blood-brain-barrier. In peripheral vascular endothelium, paracellular permeability is dictated by AJ with rather discontinuous TJ distribution (101). Various factors influence the formation and disruption of intercellular junctions. In response to VEGF as an angiogenesis mediator stimulating endothelial migration and/or proliferation, adherens junctional protein clusters of VE-cadherin (VE-Cad) are disrupted by internalization using β -arrestin mediated endocytosis (102). VE-Cad regulates the formation of tight junctions by increasing expression of claudin-5 via inhibition of nuclear accumulation of FoxO1 and β -catenin, which are inhibitory promoters of claudin-5 (103, 104). *In vitro*, VEGF was thus shown to decrease localization of occludin, VE-Cad, and ZO-1 at junctional sites of endothelial cells (105). *In vivo*, induction of endothelial fenestration and vesicular vacuolar organelles was observed as well (106). Hence, VEGF might not solely regulate paracellular permeability but additionally enables increased transcellular passage.

3.3.1.2 Extracellular matrix and glycocalyx deposition

Focal adhesions link endothelial cells to the BM on the basolateral site by binding to RGD-motifs within ECM proteins collagen, laminin, fibronectin, and vitronectin (107, 108). These are serving as structural support and anchor of the cellular monolayer. While their involvement in permeability modulation is not understood so far, the mechanotransduction of shear stress and the angiogenic activity of endothelial cells has been described to be modulated integrin-dependently (108, 109). On the luminal site of endothelial cells, proteoglycans, such as Syndecan-1, are anchored to the membrane, providing the main structure of the endothelial glycocalyx, and further connect to glycosaminoglycans. Thereby, a complex and tissue-dependently highly variable network of heavily glycosylated proteins and glycolipids is formed, which lines the luminal surface of endothelial cells. In addition to proteoglycans' cellular attachment, hyaluronan can bind the endothelial CD44 receptor, attracting water to the glycocalyx and enabling its gel-like state. The binding of serum proteins, growth factors and cytokines to the glycocalyx makes it a bioactive surface layer of endothelial

cells, involved in regulation of cellular adhesion, endothelial activation and, thus, vascular permeability (110).

3.3.2 Endothelial redox balance and dysfunction

In addition to the selective barrier function between vessel lumen and interstitial space, the vascular endothelium contributes to vascular homeostasis by a balanced expression of vasodilatory and antithrombotic factors, such as nitric oxide (NO) and prostacyclin. This equilibrium is further influenced by the expression and synthesis of angiotensin II, endothelin-1 and reactive oxygen species (ROS), which exert vasoconstrictive effects; while von Willebrand-factor and plasminogen activator inhibitor-1 are able to induce prothrombotic activity (111-116). An endothelial dysfunction, enabled by an imbalance of those factors favoring vasoconstrictive and prothrombotic effects, is a crucial feature of cardiovascular diseases, e.g., atherosclerosis, hypertension, and stroke (117-119).

3.3.2.1 Maintenance of endothelial function

A decrease in synthesis, activity, or release of endothelial NO is the main characteristic of a disturbance of endothelial homeostasis. Endothelium-derived NO can mediate vasodilation of the vasculature by diffusion to smooth muscle cells and subsequent cGMP-mediated extrusion of Ca^{2+} from the cytosol, thus inhibiting vasoconstriction. While the coupling of endothelial to smooth muscle cells directly affects the vascular tone and deregulation can subsequently lead to hypertension, the functional connection of vascular cells in the blood-brain barrier is completed by neuronal cells amongst others. In neurovascular coupling, the vasculature can directly respond to an alteration in neuronal activity by modification of NO generation. Subsequently, vascular tone is adjusted, enabling a local supply of active neurons with nutrients and oxygen (120). Neurovascular coupling is exemplary for the impact of endothelial homeostasis on various specialized tissues.

Reduced availability of NO can be a consequence of uncoupling, modification, or decreased synthesis of NO-generating enzymes, as well as peroxynitrite formation. This can be mediated by ROS, such as superoxide anion and hydrogen peroxide (121) (**Figure 3.9**), from which secondary radical species can be generated, e.g., by nitration of cellular proteins or lipid peroxidation. ROS are a byproduct of aerobic metabolism but also essential mediators of cell

signaling by modulation of protein kinases and phosphatases (122), transcription factors (123), and ion channels (124, 125).

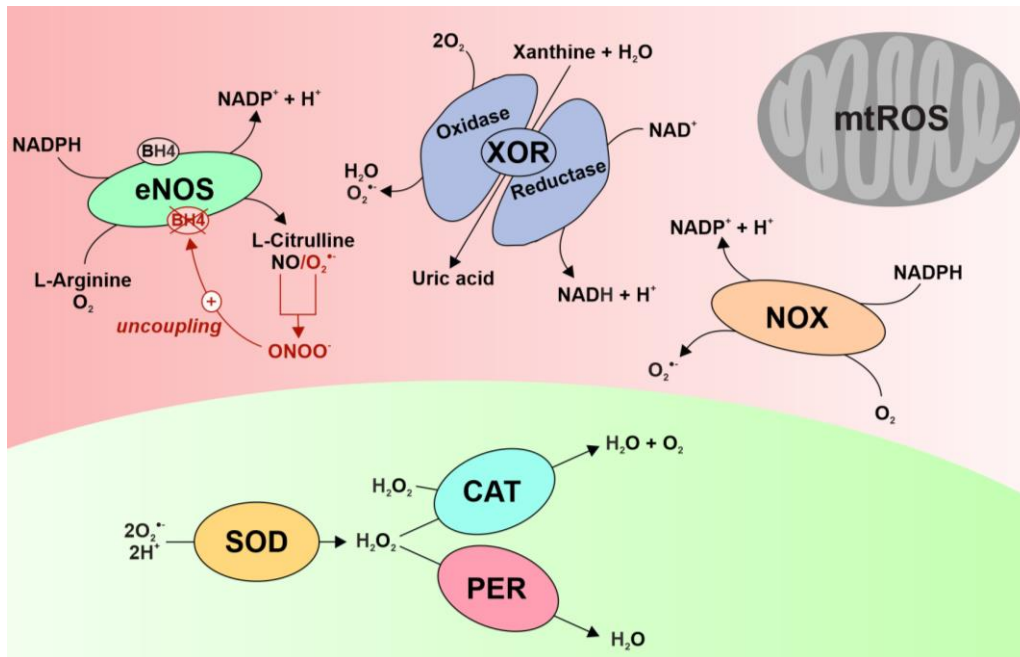


Figure 3.9. Schematic representation of reactive oxygen species (ROS) generation and scavenging. Endothelial nitric oxide synthase (eNOS) catalyzes the formation of nitric oxide (NO) tetrahydrobiopterin (BH₄)-dependently from the substrates L-Arginine and molecular oxygen. ROS presence oxidizes BH₄, resulting in uncoupling of eNOS and formation of superoxide anion (O₂•⁻) instead of NO. NO and O₂•⁻ can form peroxynitrite (ONOO⁻), further enabling uncoupling of eNOS. Xanthine oxidoreductase (XOR) catalyzes uric acid formation by its reductase activity and conversion of NAD⁺. Inflammation and oxidation of the oxidoreductase switch the enzyme to its oxidative form, resulting in a synthesis of O₂•⁻ and hydrogen peroxide (H₂O₂). During oxidative phosphorylation, ROS are produced in mitochondria for ATP generation. A dysfunctional mitochondrial electron transport chain might promote electron leakage and excessive mitochondria-derived ROS (mtROS) formation. NADPH Oxidases (NOX) solely produce ROS by conversion of molecular oxygen to O₂•⁻. NOX are required for redox signaling in endothelial cells, promoting cell survival, proliferation, and tube formation. NOX can have a vasoprotective or –damaging effect; this dual role is not entirely understood yet. ROS can be scavenged by conversion of O₂•⁻ to H₂O₂ catalyzed by superoxide dismutase (SOD), which can be transformed to water by catalases (CAT) and peroxidases (PER).

In a physiological state, an excess of ROS within endothelial cells is avoided by buffering of ROS scavenging enzymes. Superoxide dismutases can catalyze the conversion of superoxide anion to hydrogen peroxide, which can further be converted to molecular oxygen and water by catalases and peroxidases (**Figure 3.9**) (121). However, in an imbalanced state, an excess of ROS can be triggered by modulation of the antioxidant defense system of scavenging enzymes, e.g., by regulating transcription factors of the FoxO family and nuclear factor E2-

related factor 2 (Nrf2) (126, 127). In addition to intracellular changes, endothelial glycocalyx, covering the luminal site of the endothelium, can be remodeled due to exogenous ROS and endothelial dysfunction (128, 129).

The VEGF family comprises five members with different functions and expression levels during an organism's lifetime. VEGF-A is the first identified and most extensively studied member of the family, exerting previously mentioned effects on the vasculature (see **3.3.1.1**) and has been implicated in various diseases, including cancer, diabetic retinopathy, and rheumatoid arthritis. During diabetic nephropathy, VEGF-A levels are increased, resulting in proteinuria induced by VEGF-A-mediated glycocalyx shedding and thinning. VEGF-C, restricts macromolecular protein passage through the glycocalyx of glomerular endothelium by altering glycosaminoglycan sulfation, demonstrating the reciprocal relationship of members of the VEGF family in vascular homeostasis (130).

In summary, endothelial dysfunction is hallmarked by increased proinflammatory and prothrombotic effects, as well as increased vascular permeability and deregulation of vascular tone. These processes are fueled by deregulation of endothelial redox balance, external glycocalyx remodeling and alteration of adhesion sites at the vessel wall.

3.3.2.2 Therapeutical implications of endothelial dysfunction

In various cancers, VEGF is expressed by tumor cells, inducing nitric oxide synthase and subsequent NO formation in the vasculature (131). VEGF is also elevating superoxide anion levels by induction of endothelial NAPDH oxidase (132). In addition to the permeability-increasing effect of VEGF discussed in **3.3.1.1**, as well as its implication in endothelial dysfunction (**3.3.2**), it thus ultimately promotes endothelial proliferation, migration, and tube formation. VEGF can also enable nutrient and oxygen supply to malignant cells by tumor angiogenesis and increased leakiness of pre-existing and newly formed vasculature. The remodeling of the vasculature in tumor angiogenesis is accompanied by degradation of the endothelial BM and ECM catalyzed by MMPs (133). Due to the importance of these processes for supplying nutrients and oxygen to the tumor, the tumor vasculature recently became a target for pharmaceutical approaches in cancer therapy. Owing to the critical relevance of VEGF in tumor angiogenesis, several strategies for cancer therapy rely on inhibition of VEGF signaling: The monoclonal antibody Bevacizumab targets and inactivates VEGF-A, being the

first approved anti-vascular cancer drug (134, 135). Other clinically approved drugs inhibit the VEGFR tyrosine kinase or its downstream signaling pathway (136-138).

While the re-establishment of a physiological vasculature is relevant in anti-angiogenic and anti-vascular therapy, a transient opening of epithelial and endothelial barriers can also be a suitable strategy for improvement of drug delivery. Sodium caprate can act as an absorption enhancer for orally applied drugs by dilating tight junctions of the epithelial intestinal barrier (139) and is currently investigated as a reversible modulator of the blood-brain barrier (140, 141). Lobradimil is a synthetic bradykinin analog transiently opening the blood-brain barrier by a hyperosmolar dilation of cell junctions. In a clinical trial of glioma, a combination treatment of lobradimil with the cancer drug carboplatin was investigated (142). Although there is no substance for the transient opening of endothelial barriers approved yet, the combinatory treatment with barrier modulators and pre-existing drugs for 'hard-to-reach targets' might be a promising approach for drug delivery improvement. However, the transient opening of endothelial barriers, such as the blood-brain barrier, should be closely monitored, due to possibilities of unspecific macromolecule passage, possibly compromising the therapeutic's toxicity profile.

Previous studies have further indicated that the vasodilatory function of endothelial cells is declining in the aging organism (143, 144). In addition to endothelial dysfunction observed in pathologies such as cancer, ROS formation in endothelial cells increases with advanced age in model organisms and humans. This age-correlating increase is presumably due to reduced availability of NO by uncoupling and decreased expression of eNOS (145), induction of NADPH oxidase (146), as well as mitochondrial dysfunction (147) and subsequent mtROS formation. Consequences of these alterations are inflammatory processes in the aged vasculature, such as proinflammatory cytokine and MMP secretion. Transcription factor Nrf2 regulates the expression of ROS scavenging enzymes and was shown to be dysfunctional in the aging vasculature, reducing the buffer capacity of the antioxidant defense system to oxidative stress (148). Senescence is an observed phenomenon in aged vascular endothelial and smooth muscle cells, i.e., cells enter an irreversible cell cycle arrest, accompanied by a profound secretion of proinflammatory cytokines (senescence-associated secretory phenotype). The sirtuin enzyme family was demonstrated to regulate mitochondrial function and the DNA damage repair machinery. Sirtuin enzyme SIRT1 was reported to suppress senescence in endothelial cells triggered by oxidative stress, while its inhibition promoted endothelial

senescence. During the aging of endothelial cells, SIRT1 is downregulated by autophagosome-lysosome degradation, enhancing mitochondrial impairment and inflammatory effects (149). Thus, sirtuins are popular targets of longevity improving drug development implicated in cardiovascular and metabolic diseases such as arrhythmia, hypertension, diabetes, and dyslipidemia. Resveratrol is a naturally occurring polyphenol with radical-scavenging activity (150), which was shown to activate Nrf2 (46, 151) as well as the SIRT1 signaling pathway (152, 153), ameliorating the antioxidant defense system of aging endothelial cells while reducing endothelial senescence. Resveratrol was also demonstrated to improve coupling of neuronal activity to vasoadaptation of the cerebral microcirculation in aged rodents (154). However, its potential for clinical application is limited due to its low aqueous solubility and bioavailability as well as rapid systemic elimination (155). Hence synthetic activators of SIRT1 have been developed, facilitating SIRT1 activation by allosteric binding (156). Other therapeutic approaches for vascular aging involve the use of senolytics that can remove senescent cells. A combinatory treatment of quercetin and dasatinib decreased senescent cell burden in adipose tissue in a clinical study focusing on idiopathic pulmonary fibrosis (157). While there is growing evidence that senolytical treatment is relevant for vascular aging-related pathologies, further research is necessary to confirm their beneficial effects specific to the vasculature.

3.4 Aim of the thesis

The previous chapters introduced the relevance of liposomes as pharmaceutical vehicles and the therapeutic potential of emerging technologies, such as FL. They were previously shown to enable an efficient uptake of cargo by mammalian cells, mediated by membrane fusion and direct cytosolic delivery. Even though an increased uptake efficiency might translate to enhanced pharmacological cargo effects compared to stealth liposome technology, comprehensive knowledge of interactions with further physiological barriers after administration is missing.

Hence, the purpose of this thesis was to promote the understanding of interactions that FL and their cargo encounter on the way to their respective site of action; and how this can influence therapeutic efficacy of the cargo. FL have been previously characterized as delivery vehicles for various biomolecules. Yet, in this work, the consequence of different chemical characteristics of cargo had to be explored. This had to be done by investigating the pharmacological efficacy of clinically relevant anti-cancer therapeutics of a similar scaffold but different basicity. Furthermore, the relevance of cargo incorporation into FL for cellular uptake required an investigation by delivery of membrane-impermeable cargo.

A key application of liposomal formulations in clinically relevant contexts is the delivery of anti-cancer therapeutics to the tumor. Here, liposomal stealth technology has been dominating the field over the last three decades. A preferential accumulation of these liposomes at the tumor site, mediated by the enhanced permeability and retention effect, is accompanied by reduced adverse reactions, and often not by increased efficacy. Consequently, innovative delivery strategies are investigated that focus on an optimized cellular uptake of liposome cargo. A goal of this work was to further examine the application of FL for drug delivery to the tumor, which is highly dependent on the passage of nanoparticles through the tumor matrix, as well as the intracellular availability of delivered drugs. FL interactions with ECM had to be explored in a first step. In a second step, cargo performance had to be evaluated in a three-dimensional cell model with an ECM that can be manipulated in thickness and integrity. In breast cancer, lesions of the BM are features of cancer progression; thus, the BM is a crucial physiological barrier in cancer therapy by the protection of untransformed cells in contrast to the exposure of invasive cells infiltrating neighboring tissue. Accordingly, the uptake of a liposomal tracer dye and the performance of anti-cancer

therapeutics must also be evaluated concerning the thickness and integrity of the BM in a comparative study of FL and stealth liposomes.

For systemic administration of liposomes as drug delivery vehicles, additional important parameters are the interaction with blood content and their biodistribution and passage of the vascular endothelium. Previous investigations of FL interaction with blood content need to be complemented by investigating endothelial fusion efficiencies after serum addition *in vitro*. Furthermore, the passage of FL through vascular endothelial cell layer as an important physiological barrier had to be investigated with and without compromised intercellular junctions. These mimic physiological and pathophysiological endothelial states by manipulation of the redox balance and stimulation with cancer-relevant VEGF. Here, the application of FL as direct mediators of endothelial cargo delivery required additional attention, exemplarily shown by the delivery of a commonly used antioxidant and the investigation of its functional effects *in vitro* and in a mouse model of vascular aging. Moreover, the study of systemic FL administration had to be concluded with an investigation of FL tissue localization and circulation time *in vivo*, enabling a more detailed view of FL's pharmacokinetic profile.

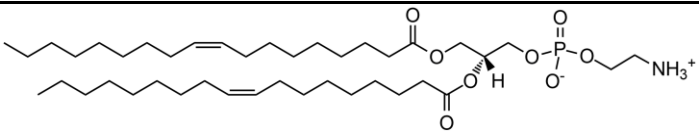
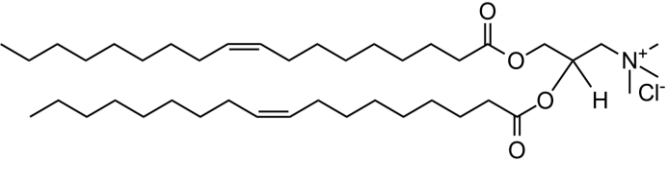
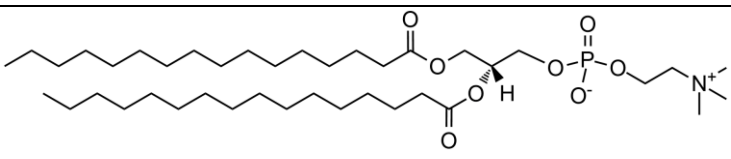
4 Material and methods

4.1 Material

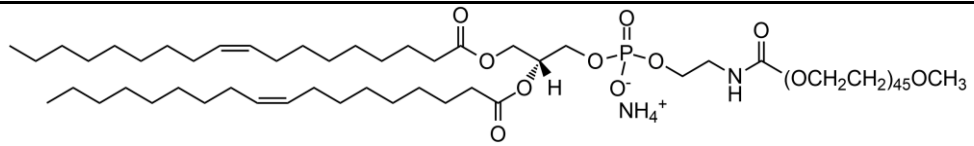
4.1.1 Lipids, lipid derivatives and dyes, and liposome cargo

Lipids and lipid derivatives were purchased from Avanti Polar Lipids, Inc. (Alabaster, AL, USA) in chloroform at 10 mg/mL. The carbocyanine dyes 3,3'-dioctadecyloxacarbocyanine perchlorate (DiO; D275), 1,1'-dioctadecyl-3,3,3',3'-tetramethylindocarbocyanine perchlorate (DiI; D3911), 1,1'-dioctadecyl-3,3,3',3'-tetramethylindodicarbocyanine, 4-chlorobenzene-sulfonate salt (DiD; D7757) and 1,1'-dioctadecyl-3,3,3',3'-tetramethylindotricarbocyanine iodide (DiR; D12731) (all ThermoFisher Scientific, Waltham, MA, USA) and aclacinomycin A (Santa Cruz Biotechnology, Dallas, TX, USA) were dissolved in chloroform at 1 mg/mL. Doxorubicin hydrochloride (Sigma-Aldrich, St. Louis, MO, USA) was dissolved in a 9/1 (v/v) mixture of chloroform and ethanol absolute at 1 mg/mL, propidium iodide (Sigma-Aldrich) was dissolved in dimethylsulfoxide (DMSO) at 1 mg/mL, and resveratrol (Sigma-Aldrich) was dissolved in ethanol absolute at 1 mg/mL. All derivatives are shown in **Table 4.1**.

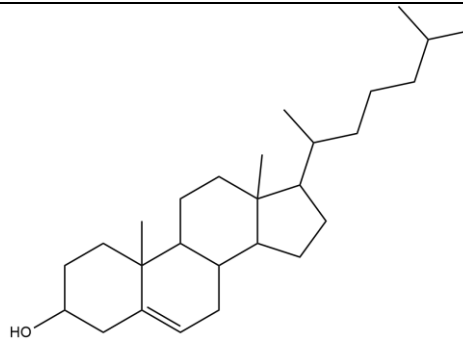
Table 4.1. Lipids, lipid derivatives and dyes, and liposomal cargo. Abbreviations and chemical structures are shown, as well as IUPAC nomenclature or trivial names in brackets.

Lipids, lipid derivatives and dyes, and liposomal cargo	
	DOPE (1,2-dioleoyl-sn-glycero-3-phosphoethanolamine)
	DOTAP (1,2-dioleoyl-3-trimethylammonium-propane; chloride salt)
	DPPC (1,2-dipalmitoyl-sn-glycero-3-phosphocholine)

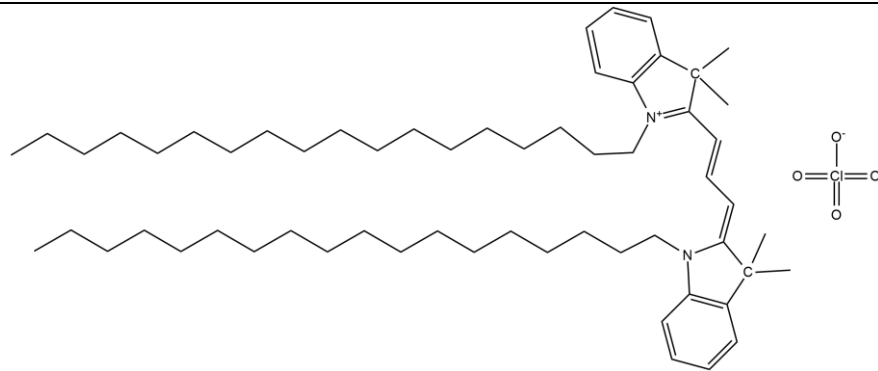
Lipids, lipid derivatives and dyes, and liposomal cargo



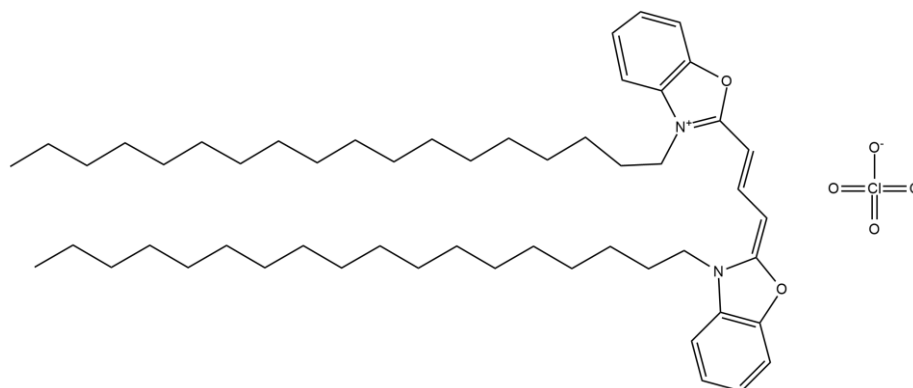
PEG-PE 1,2-dioleoyl-sn-glycero-3-phosphoethanolamine-N-[methoxy(polyethylene glycol)-2000] (ammonium salt)



cholesterol ((3β)-cholest-5-en-3-ol)

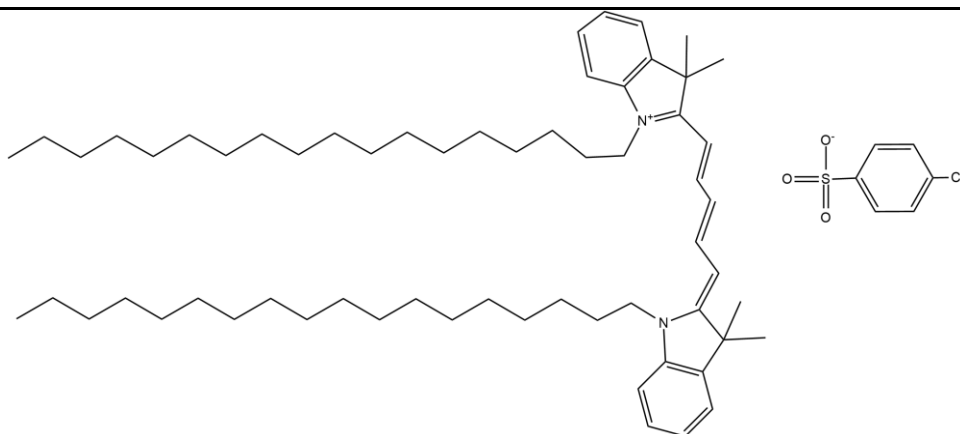


DiI (1,1'-dioctadecyl-3,3,3',3'-tetramethylindocarbocyanine perchlorate)

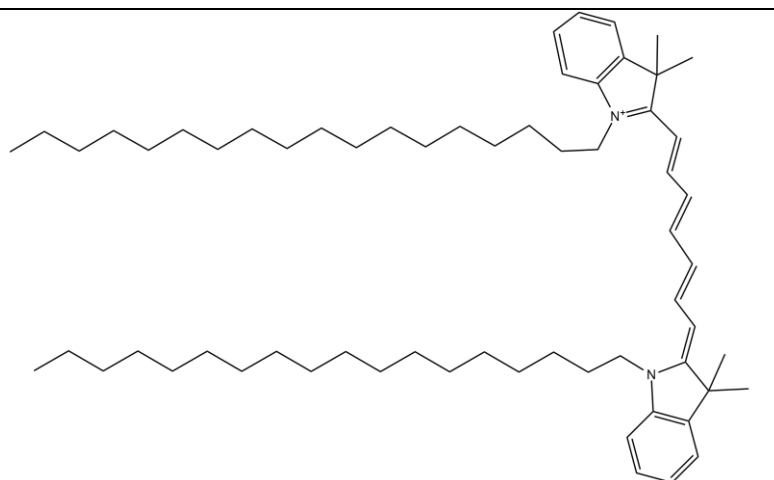


DiO (3,3'-dioctadecyloxocarbocyanine perchlorate)

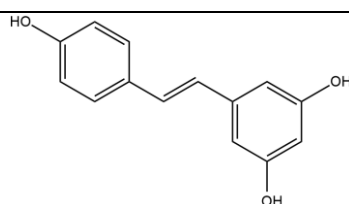
Lipids, lipid derivatives and dyes, and liposomal cargo



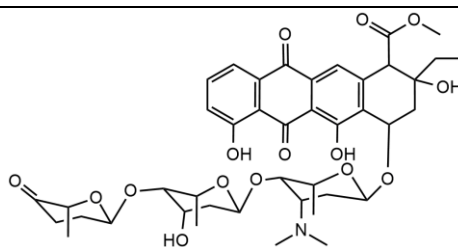
DiD (1,1'-dioctadecyl-3,3,3',3'-tetramethylindodicarbocyanine, 4-chlorobenzenesulfonate salt)



DiR (1,1'-dioctadecyl-3,3,3',3'-tetramethylindotricarbocyanine iodide)

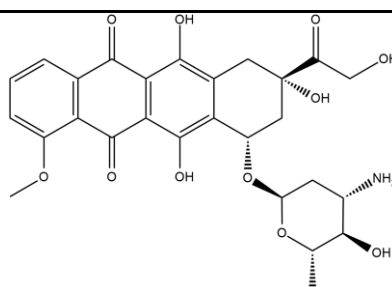


RSV (resveratrol; trans-3,5,4'-trihydroxystilben)

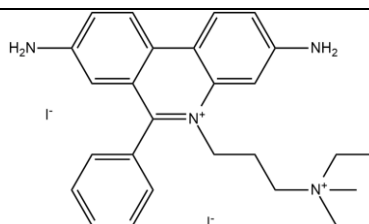


ACL (aclacinomycin a; aclarubicin)

Lipids, lipid derivatives and dyes, and liposomal cargo



DOX (doxorubicin; adriamycin)



PI (propidium iodide)

4.1.2 Chemicals/kits

Chemical/kit	Company
Fix & Perm cell fixation and permeabilization kit	ThermoFisher Scientific, Waltham, MA, USA
Click-iT™ EdU Imaging Kit with Alexa Fluor™ 488	ThermoFisher Scientific, Waltham, MA, USA
Ascorbic Acid	Sigma-Aldrich, St. Louis, MO, USA
Basic fibroblast growth factor (bFGF), recombinant, expressed in <i>E. coli</i>	Sigma-Aldrich, St. Louis, MO, USA
Chloroform zur Analyse EMSURE® ACS, ISO, Reag. Ph Eur	Merck, Darmstadt, Germany
Cholera toxin from <i>vibrio cholera</i> , 5 %	Sigma-Aldrich, St. Louis, MO, USA
Collagen I, rat tail	Enzo Life Sciences, Farmingdale, NY, USA
Collagenase IV	Worthington, Lakewood, NJ, USA
Cumene hydroperoxide	Sigma-Aldrich, St. Louis, MO, USA
DMEM/F12 Glutamax	ThermoFisher Scientific, Waltham, MA, USA
DRAQ5	ThermoFisher Scientific, Waltham, MA, USA
Epidermal growth factor (EGF), hEGF, recombinant, expressed in <i>E. coli</i>	Sigma-Aldrich, St. Louis, MO, USA

Material and methods

Chemical/kit	Company
Endothelial cell growth medium 2 ready-to-use	Promocell, Heidelberg, Germany
Fetal bovine serum, qualified, Brazil	ThermoFisher Scientific, Waltham, MA, USA
Fibronectin	Corning Life Sciences, New York, NY, USA
Fluorescein isothiocyanate–dextran (500 kDa)	Sigma-Aldrich, St. Louis, MO, USA
Geltrex™ LDEV-Free Reduced Growth Factor Basement Membrane Matrix	ThermoFisher Scientific, Waltham, MA, USA
Goat serum	Sigma-Aldrich, St. Louis, MO, USA
HEPES	VWR, Radnor, PA, USA
Horse serum, New Zealand origin	ThermoFisher Scientific, Waltham, MA, USA
Hydrocortisone, suitable for cell culture	Sigma-Aldrich, St. Louis, MO, USA
Insulin	Sigma-Aldrich, St. Louis, MO, USA
Milk powder	Carl Roth, Karlsruhe, Germany
N ω - Nitro-L-arginine methyl ester	Sigma-Aldrich, St. Louis, MO, USA
Nucblue	ThermoFisher Scientific, Waltham, MA, USA
Penicillin/Streptomycin	Sigma-Aldrich, St. Louis, MO, USA
Paraformaldehyde (PFA)	Merck Millipore, Burlington, MA, USA
Poly-L-lysine, 0.01%, sterile-filtered	Sigma-Aldrich, St. Louis, MO, USA
Skim milk powder	Sigma-Aldrich, St. Louis, MO, USA
Texas Red–dextran (10, 70 kDa)	ThermoFisher Scientific, Waltham, MA, USA
Triton X-100	Sigma-Aldrich, St. Louis, MO, USA
Trypsin/EDTA 0.05	ThermoFisher Scientific, Waltham, MA, USA
Tween® 20	Sigma-Aldrich, St. Louis, MO, USA
Vascular endothelial growth factor (VEGF), recombinant human VEGF 165 protein	R&D Systems, Minneapolis, MN, USA

4.1.3 Other consumables

Consumable material	Company
Nanosep® centrifugal devices with a 100 K Omega Membrane	Pall, NY, USA
Cell culture insert plates, pore size 3 μ m	VWR, Radnor, PA, USA
Cell culture plates, 96-wells, flat bottom	ThermoFisher Scientific, Waltham, MA, USA
Cell culture plates, 96-wells, round bottom	Greiner Bio-one, Frickenhausen, Germany

Consumable material	Company
Falcon tissue culture flask sterile, vented, canted	Corning®, NY, USA
Glass coverslips	Thomas Scientific, Swedesboro, NJ, USA
High-precision microscopy glass	ThermoFisher Scientific, Waltham, MA, USA
Immersion oil 518 F and W	Carl Zeiss, Jena, Germany
Serological pipettes, stripette® (5 mL, 10 mL, 25 mL, 50 mL)	Corning®, NY, USA
Jet Set-4 dental acrylic resin	Lang Dental, Wheeling, IL, USA
Pipette tips (10 µL, 200 µL, 1250 µL)	StarLab, Hamburg, Germany
Reaction tube 1.5 mL, 2 mL	Eppendorf, Hamburg, Germany
Reaction tube 15 mL, 50 mL	Greiner Bio-one, Frickenhausen, Germany
Quartz glass cuvette	Hellma, Mühlheim, Germany

4.1.4 Media and buffers

All buffers were prepared in purified, degassed, and filtrated water (Milli-Q, Merck Millipore, Burlington, MA, USA), pH was adjusted with aqueous solutions of HCl or NaOH.

Cytoskeletal buffer (CB), pH 6.1

Components	Concentration
EGTA	5 mM
Glucose	5 mM
MES (2(N-morpholino)-ethanesulfonic acid)	1.95 g/L
MgCl ₂	10 mM
NaCl	150 mM
Streptomycin	1.72 mM
in purified, degassed, and filtrated water	

Phosphate-buffered saline (PBS), pH 7.4

Components	Concentration
NaCl	137 mM
KCl	2.7 mM
Na ₂ HPO ₄	10 mM
KH ₂ PO ₄	1.8 mM
in purified, degassed, and filtrated water	

Material and methods

HEPES buffer, pH 7.4

Components	Concentration
HEPES (2-(4-(2-hydroxyethyl)-1-piperazinyl)-ethanesulfonic acid) in purified, degassed, and filtrated water	20 mM

MCF 10A growth medium

Components	Concentration
Horse serum	5 % (v/v)
EGF	20 ng/mL
Hydrocortisone	0.5 µg/mL
Cholera toxin	100 ng/mL
Insulin	10 µg/mL
Penicillin/Streptomycin in DMEM/F12 Glutamax	100 U/mL

MCF 10A assay medium

Components	Concentration
Horse serum	2 %
EGF (optional)	5 ng/mL
Hydrocortisone	0.5 µg/mL
Cholera toxin	1 ng/mL
Insulin	10 µg/mL
Penicillin/Streptomycin in DMEM/F12 Glutamax	100 U/mL

MDA-MB-231 growth medium

Components	Concentration
Fetal bovine serum	10 %
Penicillin/Streptomycin in DMEM/F12 Glutamax	100 U/mL

HUVEC endothelial cell growth medium-2

Components	Concentration
Fetal calf serum	2 %
EGF	5 ng/mL
Hydrocortisone	0.2 µg/mL
Basic fibroblast growth factor	10 ng/mL
Insulin-like growth factor	20 ng/mL

Components	Concentration
Vascular endothelial growth factor	0.5 ng/mL
Ascorbic acid	1 µg/mL
Heparin	22.5 µg/mL
in Endothelial cell growth medium 2	

4.1.5 Antibodies

Antibodies	Company
Anti-laminin-5 clone D4B5 (MAB19562)	Merck Millipore, Burlington, MA, USA
Anti-type IV collagen (ab6586)	Abcam, Cambridge, UK
Anti-claudin 1 (37-4900)	ThermoFisher Scientific, Waltham, MA, USA
Anti-VE-cadherin (D87F2) XP® (2500T)	Cell Signaling Technologies, Danvers MA, USA
Donkey anti-mouse Alexa Fluor™ 546	ThermoFisher Scientific, Waltham, MA, USA
Goat anti-rabbit Alexa Fluor™ 488	ThermoFisher Scientific, Waltham, MA, USA
Chicken anti-rabbit Alexa Fluor™ 488	ThermoFisher Scientific, Waltham, MA, USA
Goat anti-mouse Alexa Fluor™ 488	ThermoFisher Scientific, Waltham, MA, USA

4.1.6 Instruments

Hardware	Company
Sonicator Sonocool SC 255	Bandelin, Berlin, Germany
Nano ZS Zetasizer	Malvern Instruments, Malvern, UK
Cell culture centrifuge Sigma 3-16L	Sigma Laborzentrifugen, Osterode am Harz, Germany
Cell culture Microscope Axiovert 40 CFL and Axiovert A1	Carl Zeiss, Jena, Germany
Table-top centrifuge	Eppendorf, Hamburg, Germany
Spectrometer Fluorolog-3	Horiba Jobin Yvon, Kyoto, Japan
Flow Cytometer Guava Easy Cyte 8HT	Merck Millipore, Burlington, VT, USA
Flow Cytometer CytoFlex S	Beckman Coulter, Brea, CA, USA
FluoView 1000 MPE two-photon microscope	Olympus, Tokyo, Japan
Infinite® 200 PRO plate reader	Tecan Life Sciences, Maennedorf, Switzerland
Laser Scanning Microscope(LSM) 710	Carl Zeiss, Jena, Germany
Laser Scanning Microscope (LSM) 880	Carl Zeiss, Jena, Germany
Laser speckle contrast imager	Perimed, Järfälla, Sweden

Material and methods

Hardware	Company
MouseVent G500	Kent Scientific Co, Torrington, CT, USA
Pneumatic dental drill	Foredom, Blackstone Industries, Bethel, CT, USA
Pico plasma cleaner	Diener Electronics, Ebhausen, Germany
Thermostatic heating pad	Kent Scientific Co, Torrington, CT, USA
Spark® plate reader	Tecan Life Sciences, Maennedorf, Switzerland
Stereo Microscope Stemi 508	Carl Zeiss, Jena, Germany
Stereotactic frame	Leica Microsystems, Buffalo Grove, IL
Surgivet Classic T3 vaporizer	Smiths Medical, Minneapolis, MN, USA

4.1.7 Software

Software name	Company
BioDraw Ultra 12.0	CambridgeSoft, Cambridge, MA, USA
Corel draw 2019	Corel, Ottawa, Kanada
CytExpert 2.3	Beckman Coulter, Brea, CA, USA
Graph Pad Prism 7	GraphPad Software, San Diego, USA
i-control™	Tecan Life Sciences, Maennedorf, Switzerland
Image J	Wayne Rasband, U.S. National Institutes of Health, Bethesda, MD, USA (158, 159)
Imaris 9.5.0	Bitplane, Zürich, Switzerland
Guava® InCyte	Merck Millipore, Burlington, VT, USA
Matlab R2019b	MathWorks, MA, USA
Origin 2019	OriginLab Corporation, Northampton, MA, USA
Zen black 2012	Carl Zeiss, Jena, Germany
Zen blue 2012	Carl Zeiss, Jena, Germany
Zetasizer Software	Malvern Instruments, Malvern, UK

4.2 Methods

4.2.1 Liposome formation and characterization

Fusogenic and endocytic liposomes were prepared by solvent evaporation of the lipid composition of choice and subsequent film hydration. If needed, cargo for cellular delivery was added to the lipid mixture in an organic solvent to achieve passive loading of liposomes. The obtained multilamellar vesicles were further vortexed vigorously and sonicated to obtain a homogeneous population of unilamellar vesicles (**Figure 4.1**) (160).

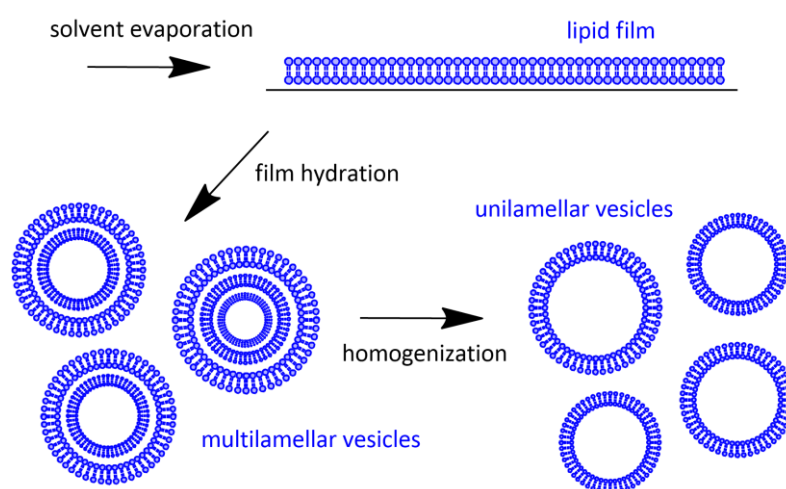


Figure 4.1. Preparation of liposomes. A lipid film is produced by organic solvent evaporation of a lipid mixture. The lipid film is further hydrated and vortexed generating multilamellar vesicles, with further sonication to homogenize liposomes to unilamellar vesicles.

4.2.1.1 Liposome Preparation

In more detail, to prepare FL, DOPE and DOTAP were mixed in chloroform 1:1 (w/w). A carbocyanine dye (DiO, DiI, DiD, or DiR) was added to the lipid mixture at 2 – 4 mol %. To prepare pegylated and endocytic liposomes (PEG-EL), DPPC, PEG-PE and cholesterol were mixed in chloroform 3:1:1 (w/w/w) under addition of DiR at 2 mol %. For loading of the liposomal formulations, cargo was added to the lipid mixture before solvent evaporation and subsequent film hydration. ACL and DOX were added to a final treatment concentration of 0.6 μM and 1.8 μM , respectively. PI was added to a final treatment concentration of 1.5 μM , and RSV was added to the lipid mixture 2:3 (total lipids:RSV; w/w). Solvents were removed, and lipid films were generated by vacuum evaporation overnight. Subsequent film hydration

was done with HEPES buffer to a total lipid concentration of 2 mg/mL. Liposomal solutions were further sonicated in an ultrasonic bath for 20 min at 4 °C.

4.2.1.2 Characterization of size and zeta potential

Dynamic and electrophoretic light scattering were used to evaluate size and zeta potential distributions. Dynamic light scattering measures the fluctuation rate of the scattered light's intensity, linking the speed of particle diffusion to the size of liposomes due to the size-dependency of the diffusion coefficient of Brownian motion (161), as described in the Stokes-Einstein equation (see **Equation 1.1**) for spherical particles. Here, the hydrodynamic diameter of spherical particles (d_H) is displayed as the quotient of the Boltzmann constant k_B multiplied with temperature T and the product of solvent viscosity η and the diffusion coefficient D .

$$d_H = \frac{k_B T}{3\pi\eta D} \quad (1.1)$$

For the displayed measurements, Z-averaged sizes of liposomes are presented to increase data robustness, and polydispersity indices are shown to indicate the size distribution width. For calculation of the zeta potential (ζ), a concept describing the electrical potential at the shear plane of a colloid in solution, electrophoretic light scattering is used to measure electrophoretic mobility. The electrophoretic mobility (U_E) or velocity of a particle motion in an oscillating electrical field depends on zeta potential and is measured as a beat frequency compared to a reference frequency and the corresponding phase shift, followed by a conversion to zeta potential (162), as described in Henry's equation (see **Equation 1.2**). Here, ϵ is the dielectric constant and $F(ka)$ is the Henry's equation, with ka displaying the ratio of particle radius to double layer thickness. Henry's equation is estimated at 1.5 if ka is large, as can be assumed for large particles with thin double layers formed in highly diluted water-based solutions.

$$U_E = \frac{2\epsilon\zeta F(ka)}{3\eta} \quad (1.2)$$

In brief, samples were diluted 1:10 (v/v) in purified, degassed, and filtrated water for size distribution measurements and 1:45 (v/v) for zeta potential measurements using a Nano ZS Zetasizer equipped with a HeNe laser (633 nm). Collection of backscattered light was done at a constant angle of 173°. Measurements were performed of at least three independently prepared samples with constant measurement conditions and data were analyzed using the instrument's software. Data are presented as mean Z-averages of liposome size (nm) and

mean peak position of the zeta potential distribution curve (mV) with standard deviation of at least three independently prepared samples. Examples of distribution plots of FL and PEG-EL for both measurements are exemplarily shown in **Figure 4.2**.

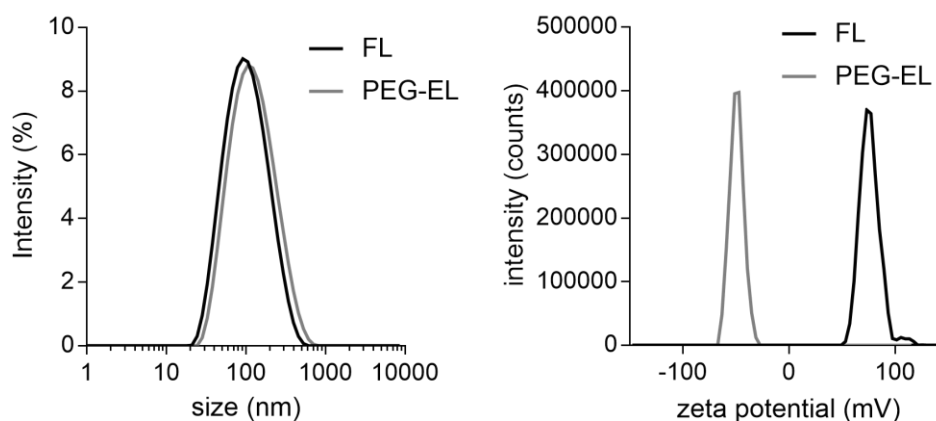


Figure 4.2. Exemplary size and zeta potential distribution plots of fusogenic liposomes (FL) and pegylated, endocytic liposomes (PEG-EL) are shown.

4.2.1.3 Characterization of entrapment efficiency

The evaluation of the entrapment efficiency (EE) was modified from a previously published method (163), using the ultrafiltration of liposomal formulations and subsequent measurement of untrapped fluorescent small molecule cargo. Measurement of fluorescence emission spectra for EE determination was done using the fluorescence spectrometer Fluorolog-3 using a quartz glass cuvette (excitation/emission path length 3mm/10mm), and recorded according to the excitation and emission ranges indicated in **Table 4.2**. Excitation/emission slit widths and integration time were kept constant during each fluorophore measurement. Linearity of the measurement was ensured by dilution of samples to an absorption of ≤ 0.1 and fluorescence intensity measurements below detector saturation. In brief, liposomal formulations were diluted 1:10 (v/v) in PBS and centrifuged in Nanosep[®] centrifugal devices for 6 min at 12000x g and 4 °C. Percentages of entrapped doxorubicin (DOX) and propidium iodide (PI) were detected by analysis of the flow through (ft) and calibration measurements of free compound. The more hydrophobic aclacinomycin A (ACL) and resveratrol (RSV) had to be further eluted by addition of 0.5% bovine serum albumin (BSA) in PBS. For all measurements, the amount of free compound in ft or el was quantified using a

calibration curve of fluorescence intensities (FI) of free compound, which was filtrated under similar conditions (**Figure 4.3**). The amount of entrapped compound was calculated as the difference of used to free compound and displayed as percentages (**Equations 2.1 and 3.2**; equations were partially published in (43)).

$$EE_{DOX}(\%) = 100 \% - DOX_{ft}(\%) \quad DOX_{ft}(\%) = \frac{FI_{(557\text{ nm})} - 2070}{8055} \quad (2.1)$$

$$EE_{PI}(\%) = 100 \% - PI_{ft}(\%) \quad PI_{ft}(\%) = \frac{FI_{(620\text{ nm})} - 1209}{3397} \quad (2.2)$$

$$EE_{ACL}(\%) = 100 \% - ACL_{el}(\%) \quad ACL_{el}(\%) = \frac{FI_{(580\text{ nm})} - 10318}{187.4} \quad (3.1)$$

$$EE_{RSV}(\%) = 100 \% - RSV_{el}(\%) \quad RSV_{el}(\%) = \frac{FI_{(420\text{ nm})} - 30700}{5725} \quad (3.2)$$

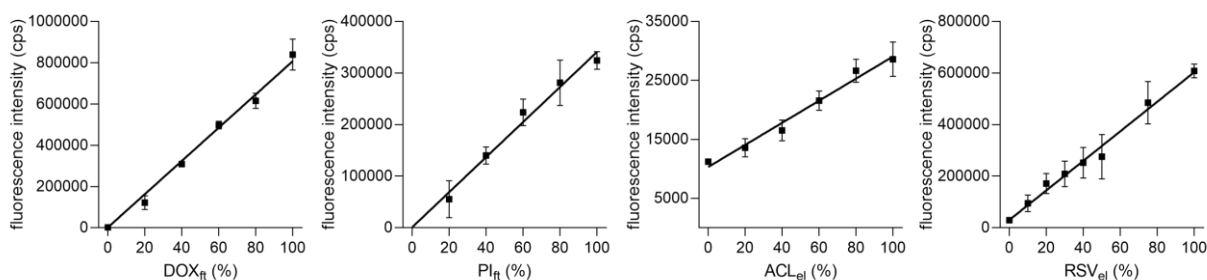


Figure 4.3. Plots of calibration measurements of fluorescence intensities of doxorubicin (DOX), propidium iodide (PI), aclacinomycin a (ACL) and resveratrol (RSV). Means with standard deviation and linear regressions are shown, which were used for calculation of entrapment efficiency in equations 2.1 – 3.2.

Table 4.2. Excitation wavelengths and emission ranges for the fluorophores measured with a spectrometer for entrapment efficiency determination.

Fluorophore	Excitation wavelength (nm)	Emission range (nm)
DiO	484	500 - 650
DiD	633	650 – 800
DiR	633	650 – 800
ACL	488	500 – 800
DOX	488	500 – 800
PI	488	500 – 800

Fluorophore	Excitation wavelength (nm)	Emission range (nm)
RSV	360	375 - 500

4.2.2 Cell culture and animal handling

4.2.2.1 Formation of cell culture substrates

For preparation of ECM-like substrates, Geltrex and collagen I were used for thick gel layer formation under sterile conditions. Geltrex is a commercially available mixture of BM components derived from Engelbreth-Holm-Swarm tumor, primarily composed of laminin, collagen IV, and entactin (64). For Geltrex gel formation, it was thawed at 4 °C overnight, gently mixed, and 40 $\mu\text{l}/\text{cm}^2$ Geltrex was used for coating of prechilled, cold plasma-pretreated glass substrates. Geltrex coating was incubated for 25 min at 37 °C and 5 % CO_2 for temperature-dependent gel formation. For collagen I gel formation, it was gently mixed with water and 10x PBS to a final 1x PBS solution with 2 mg/mL collagen I; the mixture was then neutralized with 1 N NaOH on ice. A volume of 40 $\mu\text{l}/\text{cm}^2$ collagen I was coated onto prechilled, cold plasma-pretreated glass substrates and incubated for 1 h at 37 °C and 5 % CO_2 .

4.2.2.2 MCF 10A cell line

The MCF 10A cell line is a non-tumorigenic epithelial cell line from the human mammary gland (164). It was purchased from ATCC and cultured in MCF 10A growth medium. Cells were passaged every three to four days, not exceeding 15 passages. For the culture of MCF 10A acini, a previously published protocol was used (165). Briefly, 200 cells/ cm^2 were seeded onto a preformed Geltrex bed and cultivated for nine days in EGF-supplemented MCF 10A assay medium with a media change every three to four days. From day nine, the EGF-deprived MCF 10A assay medium was used for media changes. Acini cultivation did not exceed 21 days.

4.2.2.3 MDA-MB-231 cell line

The MDA-MB-231 cell line is derived from a metastatic adenocarcinoma site in the human mammary gland and is described as poorly differentiated and mesenchymal-like, yet highly invasive (166). It is also referred to as a triple-negative breast cancer cell line due to the absence of HER2, estrogen, and progesterone receptors (167). Experiments were performed using the MDA-MB-231 cell line purchased from ATCC and cultured in the MDA-MB-231 growth medium. Cells were passaged every three to four days. For the culture of MDA-MB-

231 spheroids, 400 cells/cm² were seeded onto a preformed Geltrex bed and cultivated in MDA-MB-231 growth medium with a media change every three to four days. Spheroid cultivation did not exceed 12 days.

4.2.2.4 Primary HUVECs

Primary human umbilical vein endothelial cells (HUVECs) are non-immortalized endothelial cells. Experiments were performed using cells purchased from Lonza and cultured in endothelial cell growth medium-2. Cells were passaged every three to four days until passage six. For measurements of nanoparticle penetration through endothelial cell layers, 180 000 HUVECs/cm² were seeded on poly-l-lysine coated cell culture insert plates. After 96 h, the cell culture medium was changed to medium deprived of EGF, IGF, VEGF, and heparin for differentiation of cell contacts; and incubated for an additional 48 h.

4.2.2.5 Animal handling

The following studies of FL biodistribution and *in vivo* measurements of functional effects of FL loaded with RSV were done in cooperation with the group of Prof. Zoltan Ungvari and Prof. Anna Csiszar at University of Oklahoma Health Science Center during a 2-month research stay.

Male C57BL/6 mice of 3 months and 24 months were purchased from the aging colony maintained by the National Institute on Aging at Charles River Laboratories (Wilmington, MA, USA). Animals were housed with unlimited access to water and fed a standard AIN-93G diet under photoperiods of 12 h light/dark cycles in pathogen-free barrier conditions in the Rodent Barrier Facility at University of Oklahoma Health Science Center. All *in vivo* procedures were approved by the Institutional Animal Use and Care Committees of the University of Oklahoma Health Sciences Center (IACUC # 17-049-NSIL).

4.2.3 Imaging of liposomal treatment and passage

Fusion of liposomes with mammalian cells is enabled by a direct contact of the liposomal and the cell membrane. While the fusion process can be observed for various cell lines and primary cells *in vitro*, the microenvironment of cells *in vivo* might hinder a contact of liposomes and cell membrane, thereby modulating the fusion-mediated cellular delivery of cargo. Here, the effect of BM-associated protein secretion and ECM-like substrates were investigated to evaluate the influence of the ECM as a modulator of drug delivery. Additionally, the penetration of FL through an endothelial monolayer was investigated with a modulation of cell contact formation.

4.2.3.1 Imaging across extracellular matrix-like substrates

To visualize penetration of FL through ECM-like substrates, Geltrex and collagen I gels were formed on fluorescein-linked bovine serum albumin (BSA) coated microscopy glass as described in 4.2.2.1. FL labeled with the liposomal tracer dyes Dil or DiR were diluted 1:10 (v/v). Differently labeled liposomes were administered to the ECM gel with a delay of 24 h between treatments, enabling to monitor the possible penetration of the first applied FL through the ECM gel by a changed localization in the ECM gel in comparison to the second applied, differently labeled FL. The confocal laser scanning microscope LSM710 equipped with a Plan-Apochromat 20x/0.8 Air objective was used for imaging. Fluorescein, Dil and DiR were excited and respective emissions were detected according to **Table 4.3**. Ortho- and XY-projections were done of confocal imaging stacks covering the fluorescein BSA-coated microscopy glass and FL front, then mean grey values per frame were plotted normalized on the maximum intensity in each channel to facilitate comparison of the mean peak position in z-direction.

Table 4.3. Excitation wavelengths and emission ranges for the fluorophores detected with confocal laser-scanning microscopy in 4.2.3.1.

Fluorophore	Excitation wavelength (nm)	Emission range (nm)
Fluorescein	488	493 – 562
Dil	543	560 – 797
DiR	633	651 – 797

4.2.3.2 Imaging in a breast (cancer) model

Liposomal formulations were diluted to 40 µg/mL of total lipid concentration in PBS and incubated with 40 000 MCF10A cells/cm² seeded on fibronectin-coated high-precision microscopy glass for 10 min at 37 °C and 5 % CO₂. For liposomal treatment of MCF 10A acini and MDA-MB-231 spheroids, both were transferred to Geltrex-coated high-precision microscopy glass. Acini were transferred after 10 days (low developed; ld) or 20 days (highly developed; hd) of culture and incubated with or without EGF, representing low- or high-development states of the BM, respectively (**Figure 4.4**). Acini were either directly treated with liposomal formulations or incubated for another 30 h supplemented with 20 ng/mL EGF to promote increased proliferation of cells, as well as loss of acinar polarization and BM lesions as published previously (65, 165). Acini and spheroids were further treated for 30 min at 37 °C and 5 % CO₂ with 40 µg/mL of total lipid concentration of liposomes in PBS.

After liposomal treatment, samples were washed with PBS and either cultured in a corresponding medium for live-cell imaging or fixed with 3.7 % paraformaldehyde in CB for 20 min at room temperature, followed by a staining with NucBlue in CB (2 drops/mL) for 20 min at room temperature. To visualize BM components, acini were transferred and either directly fixed or pretreated with 290 U/mL collagenase IV, followed by immunofluorescence. In brief, acini were permeabilized with 0.3 % Tween 20 for 20 min at room temperature, followed by washing with CB and blocking for 2 h at room temperature in 5 % milk powder in CB. For visualization of collagen IV and laminin 332 secretion of MDA-MB-231 spheroids, immunofluorescence was done in the Geltrex bed without transfer. Here, spheroids were fixed and subsequently permeabilized with 0.5 % Triton X-100 in CB for 20 min at room temperature, followed by blocking with 5 % skim milk in CB for 2 h at room temperature. All samples were further incubated with primary antibodies anti-laminin-5 (1:300 in CB, note that laminin-5 is described as laminin332 in recent nomenclature) and/or anti-type IV collagen (1:200 in CB) overnight at 4 °C, followed by washing with CB and subsequent coupling to secondary antibodies goat or chicken anti-rabbit Alexa Fluor™ 488 and/or donkey anti-mouse Alexa Fluor™ 546/ goat anti-mouse Alexa Fluor™ 488 (all 1:200 in CB), followed by nucleus counterstaining with NucBlue or DRAQ5.

For visualization, the confocal laser scanning microscopes LSM880 equipped with a C-Apochromat 40x/1.2 objective and Plan-Apochromat 63x/1.4 objective, and LSM710 equipped

with an EC Plan-Neofluar 40x/1.30 objective were used. Utilized excitation and emission ranges are indicated in **Table 4.4** for each fluorophore.

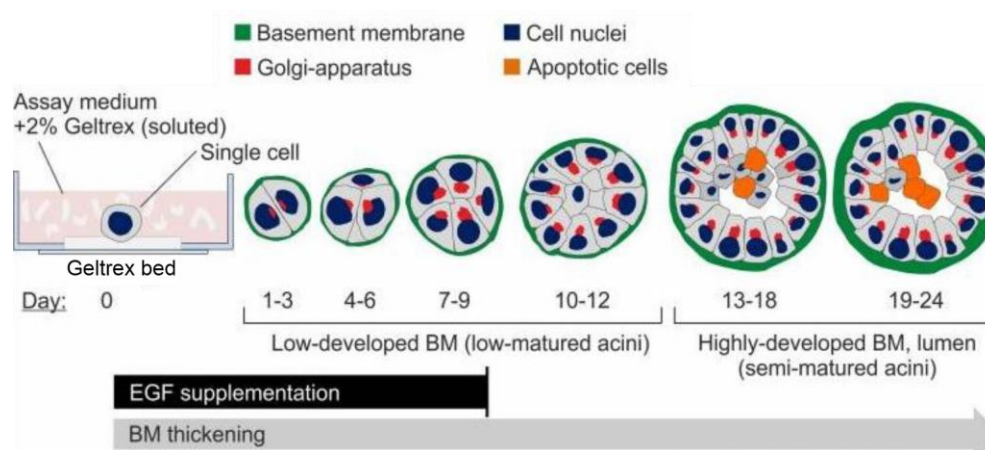


Figure 4.4. Differentiation process of MCF 10A acini during cell cultivation on a Geltrex bed, derived from single MCF 10A cells. Figure is modified from (165).

Table 4.4. Excitation wavelengths and emission ranges for the fluorophores detected with confocal laser-scanning microscopy in 4.2.3.2.

Fluorophore	Excitation wavelength (nm)	Emission range (nm)
NucBlue	405	410 – 499
DRAQ5	633	641 – 797
ACL/DOX	488	499 – 597
Alexa Fluor™ 488	488	499 – 597; 495 - 599
Alexa Fluor™ 546	561	588 – 695
DiR	633	659 – 797 (LSM710)
		651 – 758 (LSM880)

4.2.3.3 In an endothelial barrier model

To measure the penetration ability of FL and Texas Red-labeled dextran (TR-dextran) through an endothelial monolayer, primary HUVEC cells were seeded in cell culture inserts with pore size of 3 μm as described in 4.2.2.4. After cells reached confluency and medium was deprived of growth factors for cell contact differentiation, cells were treated with 50 $\mu\text{g}/\text{mL}$ FL or TR-dextran in cell culture medium for 1 h at 37 $^{\circ}\text{C}$ and 5 % CO_2 . For the measurement of

macromolecule passage, the fluorescence spectrometer Fluorolog-3 was used. Samples were taken from the basolateral compartment of the endothelial barrier model (**Figure 4.5**) and measured without further dilution in a quartz glass cuvette. Initial treatment solutions were diluted 1:3 in endothelial cell growth medium-2 as a reference. For all measurements, DiD was excited with 633 nm wavelength, and excitation was detected at 670 nm. TR was excited at 561 nm, and emission was detected at 610 nm. Integration time was 0.1 s, excitation and emission slit widths were kept constant for FL at 3 and 4 nm, and for TR-dextran at 2 and 3 nm. The fluorescence intensities of TR-dextran and FL were normalized to the fluorescence intensities of the reference treatment solution to demonstrate a potential barrier function of the cell layer.

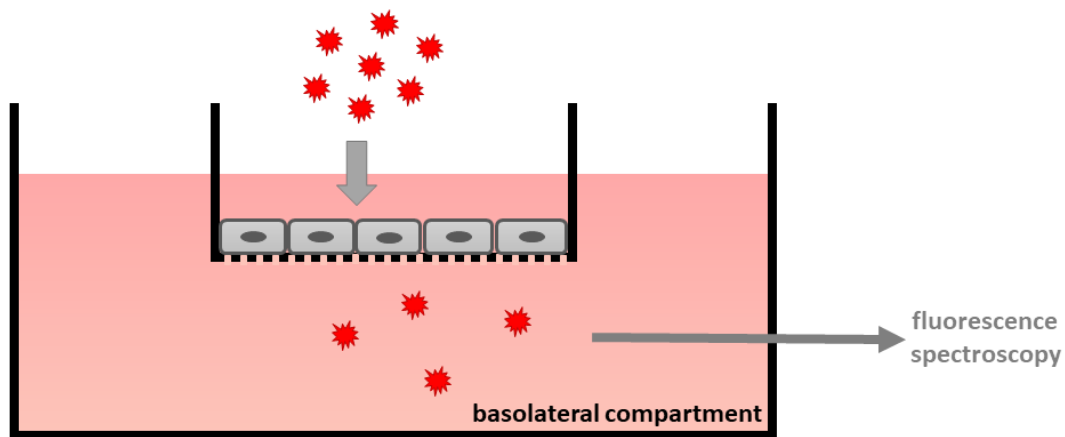


Figure 4.5. Setup of the endothelial barrier model. Primary HUVECs were seeded into cell culture inserts with 3 μm pore size. FL or TR-dextran were administered to the cell culture insert. After 1 h at 37 $^{\circ}\text{C}$ and 5 % CO_2 , the amount of FL/TR-dextran passing through the endothelial monolayer could be measured using fluorescence spectroscopy.

The impact of ROS on FL/TR-dextran passage was determined by pretreatment with 250 μM cumene hydroperoxide (CH) in cell culture medium for 15 min at 37 $^{\circ}\text{C}$ and 5 % CO_2 , 4 h in advance of permeability measurements. CH is a common inducer of oxidative stress in mammalian cells (168, 169) and was further used to trigger ROS activity in primary HUVECs. In additional samples, 100 ng/mL VEGF was added to the cell culture medium 1 h before FL/TR-dextran treatment to evaluate the influence of VEGF-induced cell contact dedifferentiation.

Presence of cell contacts was confirmed by immunofluorescence. Cells in the inserts were fixed with 3.7 % paraformaldehyde in PBS for 15 min at room temperature, washed with PBS

and permeabilized with 0.1 % Triton X-100 for 20 min at room temperature. Inserts were further washed with PBS, and blocked with 5 % goat serum in PBS for 2 h at room temperature. HUVECs were then labeled with primary antibodies anti-VE-cadherin (VE-Cad; 1:200 in 1 % goat serum in PBS), anti-claudin-1 (1:100 in 1 % goat serum in PBS), and anti-zonula occludens-1 (ZO-1; 1:50 in 1 % goat serum in PBS) for 72 h at 4 °C. Inserts were then washed with 1% goat serum in PBS, and subsequently coupled to secondary antibodies goat anti-rabbit Alexa Fluor™ 488 (1:200 in 1 % goat serum in PBS) and donkey anti-mouse Alexa Fluor™ 546 (1:200 in 1 % goat serum in PBS) for 45 min at RT, followed by washing with 1 % goat serum in PBS. For visualization, the confocal laser scanning microscope LSM880 equipped with an EC Plan-Neofluar 63x/1.30 objective was used. ZO-1/VE-Cad (Alexa Fluor™ 488) and claudin-1 (Alexa Fluor™ 488) were visualized by excitation and emission as indicated in **Table 4.5**.

Table 4.5. Excitation wavelengths and emission ranges for the fluorophores detected with confocal laser-scanning microscopy in 4.2.3.3.

Fluorophore	Excitation wavelength (nm)	Emission range (nm)
Alexa Fluor™ 488	488	499 – 553
Alexa Fluor™ 546	561	570 – 624

4.2.4 Evaluation and/or quantification of liposomal cargo and dye uptake

The quantification of liposomal dye uptake by cells and the delivery of pharmacologically relevant cargo entrapped is a requirement for the prognosis of availability at intracellular target structures. Here, the uptake of liposomes was quantified by tracking a liposomal tracer dye using flow cytometry. Further, the impact of small molecule encapsulation inside FL or supplemented to the buffer on membrane fusion was investigated with a membrane-impermeable dye (PI) using laser-scanning microscopy qualitatively. Additionally, the impact of absorption serum content to FL and the pretreatment with CH or VEGF on the fusion efficiency were evaluated using laser-scanning microscopy.

4.2.4.1 Evaluation of DiR uptake in MCF 10A acini

To analyze the uptake of the liposomal dye DiR in MCF 10A acini, acini were treated with liposomal formulations as described previously (see **4.2.3.2**) with PBS serving as a control. Subsequently, BM and cell contacts of MCF 10A acini were dissolved by treatment with 290 U/mL collagenase IV and 0.04 % trypsin EDTA for 20 min at 37 °C and 5 % CO₂. For confirmation of the involvement of the BM in DiR uptake, acini were pretreated with collagenase IV (C4ase) before liposomal treatment in a control experiment, followed by treatment with 0.04 % trypsin/EDTA without additional C4ase. The obtained suspensions of single cells were fixed with solution A of the Fix & Perm cell fixation and permeabilization kit by direct addition to suspended cells in cell culture medium. The relative change of median DiR intensity was analyzed by flow cytometry. Using the Guava easyCyte 8HT and CytoFlex S, the cell population was identified using the forward and side scatter signals. Subsequent doublet exclusion of the identified cell population was further done using forward scatter height and area. DiR was excited with a 635/638 nm laser, and fluorescence emission was detected using the band-pass optical filters 785/70 nm and 780/60 nm, respectively. The median of fluorescence intensity in the respective DiR channels was calculated using the supplier's software. The ratio of sample median fluorescence intensity to control median fluorescence intensity was examined in an identical procedure and is presented as a relative change of median shift.

4.2.4.2 Evaluation of PI uptake in MCF 10A cells

For evaluation of PI uptake respective to its formulation inside FL or the aqueous buffer, MCF 10A cells were seeded on fibronectin-coated high-precision microscopy glass and treated with FL at 40 µg/mL of total lipid concentration in PBS with PI encapsulated inside FL (FL-PI) or added to the final treatment solution (FL/PI) at 1.5 µM each in addition to unloaded FL. FL without PI addition (FL) and 1.5 µM PI in PBS (PI) served as controls. After treatment, samples were washed with PBS and imaged live in culture medium. For imaging, the confocal laser-scanning microscope LSM880 was used equipped with an EC Plan-Neofluar 40x/1.30 objective. Fluorophores were excited and emission was detected as visualized in **Table 4.6**.

Table 4.6. Excitation wavelengths and emission ranges for the fluorophores detected with confocal laser-scanning microscopy in 4.2.4.2.

Fluorophore	Excitation wavelength (nm)	Emission range (nm)
Propidium Iodide	543	602 – 797
DiR	633	651 – 797

4.2.4.3 Evaluation of fusion efficiency of primary HUVEC cells

Primary HUVECs were seeded on fibronectin-coated high-precision microscopy glass and incubated in cell culture medium for 48 h at 37 °C and 5 % CO₂. For the evaluation of serum content interaction, cells were treated with 50 µg/mL FL in PBS with or without 5 % fetal bovine serum for 15 min or 1 h at 37 °C and 5 % CO₂. To determine the effect of VEGF- and CH-pretreatment on fusion efficiency, HUVECs were treated with VEGF and CH as described in **4.2.3.3**, then HUVECs were treated with 50 µg/mL FL in medium for 15 min at 37 °C and 5 % CO₂. Samples were further washed with PBS, fixed with 3.7 % paraformaldehyde, and nuclei were labeled with NucBlue. Samples were then imaged using the laser-scanning microscope LSM710 equipped with an EC Plan-Neofluar 40x/1.30 objective with excitation wavelengths and emission ranges as indicated in **Table 4.7**. For the determination of fusion efficiency, an algorithm was developed at the Institute of Biological Information Processing 2: Mechanobiology (Forschungszentrum Jülich GmbH, Germany) by Georg Dreissen and implemented in Matlab using the staining intensity of NucBlue and DiD as previously described in (170). In brief, the NucBlue channel was segmented using its mean grey value as a threshold. Using the watershed transformation, connected nuclei were separated and cell borders were defined by the dividing line between the watershed areas. In the DiD channel, bright spots were eliminated using the local z-score as mentioned in (171). As a z-score, an environment of 91x91 pixels and a cut-off value of 2 were used. Afterwards the averaged grey value intensity of the DiD image within each detected cell border was calculated and cells exceeding a user defined threshold were defined as fused cell, all others were defined as non-fused cells. The threshold was chosen according to manual observation and kept constant for the 15 min fusion parameter and increased for 1 h fusion parameter to reduce interference of time-dependent endoplasmic reticulum accumulation of the liposomal tracer dye. The plotted fusion efficiency is the ratio of fused to all cells.

Table 4.7. Excitation wavelengths and emission ranges for the fluorophores detected with confocal laser-scanning microscopy in 4.2.4.3.

Fluorophore	Excitation wavelength (nm)	Emission range (nm)
NucBlue	405	410 – 585
DiD	633	638 – 797

4.2.5 Quantification of pharmacological effects of liposomal cargo

FL can serve as vehicles for pharmacologically active substances. In this work, the pharmacological effects of anti-cancer therapeutics and the polyphenol RSV were investigated. The used anthracyclines ACL and DOX exert inhibition of proliferation, while RSV can decrease ROS activity in cells.

4.2.5.1 Anti-proliferative effects of anthracyclines

To quantify the proliferation percentage after anthracycline treatment in MCF 10A cells and acini, a 5-ethynyl-20-deoxyuridine (EdU) incorporation assay was used. MCF 10A cells and acini were treated with FL and PEG-EL loaded with anthracyclines as described before (4.2.3.1), free anthracyclines in PBS and PBS only served as controls. For proliferation analysis in MCF 10A acini, acini were transferred after 10 days (low-developed; ld) or 20 days (high-developed; hd) of culture and incubated with or without EGF, respectively, to represent low- or high-maturation states of the BM. Following treatment, cells and acini were washed with PBS and further cultured in the corresponding medium supplemented with 10 μ M EdU. All samples were fixed with 3.7 % paraformaldehyde 72 h after seeding/transfer to high-precision microscopy glass. EdU incorporated into the DNA of newly proliferated cells was linked to Alexa Fluor™ 488 according to the supplier's instructions (Figure 4.6), followed by labeling of the cell nuclei with NucBlue.

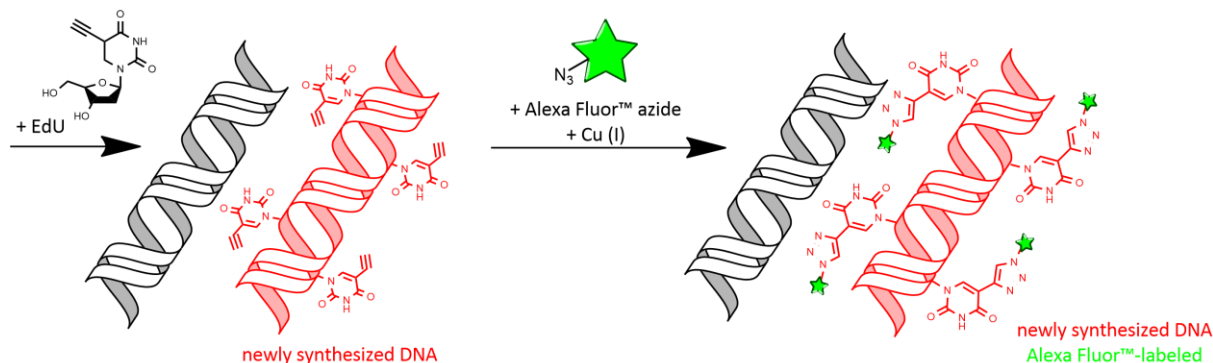


Figure 4.6. Working principle of the EdU incorporation assay used for the quantification of proliferating cells in MCF 10A acini after anthracycline treatment. During the monitored proliferation time frame, cells were cultured by supplementing EdU to the cell culture medium, which intercalates into newly synthesized DNA as a thymidine analog. In a second labeling step, Click-iT® chemistry was used to link the incorporated EdU analog to an Alexa Fluor™ fluorophore.

Imaging was carried out using the confocal laser-scanning microscope LSM880 equipped with a c-Apochromat 40x/1.2 objective and an Airyscan detector (172) with excitation wavelengths and emission bandpass filters as indicated in **Table 4.8**. MCF 10A cells were imaged in a single focal plane, imaging of acini required confocal imaging stacks. Imaging data was randomized using Matlab R2019b. To quantify NucBlue- and EdU-labeled nuclei in a single focal plane, the count of focal plane images was done manually using Fiji-ImageJ (159). For acini, the nuclei count was done semi-automatically using Imaris 9.5.0. The percentage of double-positive nuclei is shown as the proliferation percentage in both cases.

Table 4.8. Excitation wavelengths and bandpass filters for the fluorophores detected with confocal laser-scanning microscopy in 4.2.5.1.

Fluorophore	Excitation wavelength (nm)	Bandpass filters (nm)
NucBlue	405	420 – 480
Alexa Fluor™ 488	488	495 – 550

4.2.5.2 Anti-oxidative effects of resveratrol

Primary HUVECs were seeded in 96-well plates (~90 000 cells/cm²) and incubated for 48 h at 37 °C and 5 % CO₂. Cells were then treated with FL-RSV, diluted to 50 – 500 µM final RSV concentration in PBS, for 15 min at 37 °C and 5 % CO₂. Free RSV with a final concentration of 50 – 500 µM in PBS (≤ 0.2 % DMSO) served as control. Subsequently, cells were washed with PBS and treated with 250 µM CH in cell culture medium for 15 min at 37 °C and 5 % CO₂. Cells were further treated with 10 µM of chloromethyl-2',7'-dichlorodihydrofluorescein diacetate (CM-H₂DCFDA), a general oxidative stress indicator, in PBS for 30 min at 37 °C and 5 % CO₂. Here, the level of ROS corresponds to the formation of the fluorescent oxidation product, which was excited at 495 nm, and emission was detected at 520 nm (**Figure 4.7**). Cells were incubated in cell culture medium, and fluorescence intensity was measured with the Infinite® 200 PRO plate reader. Measurement settings were kept constant in all experiments. For data analysis, the fluorescence intensity of cells was normalized to controls with and without CH stimulus (100 % and 0 %, respectively), which equals ROS activity (%).

Furthermore, ROS activity in primary HUVECs was determined after previously mentioned incubation with 250 µM CH, as well as treatment with 100 ng/mL VEGF for 1 h at 37 °C and 5 % CO₂. ROS activity was assessed by incubation with CM-H₂DCFDA and subsequent fluorescence intensity measurements. Here, fluorescence intensity of cells was normalized to controls without CH or VEGF stimulus.

To further examine the effect of RSV on the permeability of primary HUVECs, cells were seeded onto cell culture inserts according to **4.2.2.4**. The effect of RSV on permeability was examined by treatment with 50 µg/mL FL-RSV for 1 h at 37 °C and 5 % CO₂. To investigate an immediate effect of FL-RSV on permeability of cells with increased ROS activity, primary HUVECs were treated with CH as indicated in **4.2.3.3**, then treated with FL-RSV, followed by an immediate assessment of permeability by treatment with TR-dextran and subsequent fluorescence spectroscopy as indicated in **4.2.3.3**. To test if FL-RSV can serve as an endothelium-protective stimulus, primary HUVECs were treated with FL-RSV, followed by CH treatment and subsequent assessment of the permeability using FL as indicated in **4.2.3.3**. To exclude interference with fluorescence spectroscopy measurements, FL-RSV were labeled with lipid dye DiO, while FL for permeability assessment were labeled with lipid dye DiD.

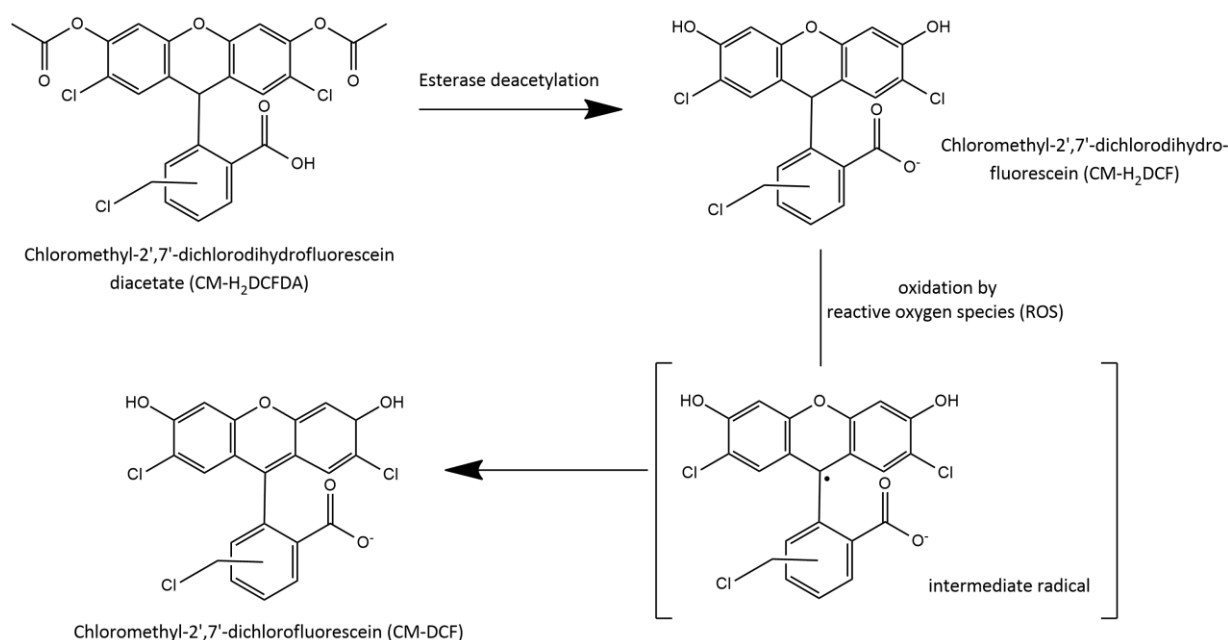


Figure 4.7. The reaction of the CM-H₂DCFDA general oxidative stress indicator after cellular uptake. CM-H₂DCFDA is cell membrane permeable, but hydrolyzed by intracellular esterases and retained in the cells. Reactive oxygen species oxidize CM-H₂DCF by intermediate radical formation to the fluorescent CM-DCF, which can be excited at 495 nm, and emission was detected at a maximum of 517 – 527 nm. The chloromethyl group of the indicator can further react with cellular thiol groups to allow covalent binding and further retention inside the cell.

4.2.5.3 Neurovascular adaptability after resveratrol treatment

The assessment of neurovascular coupling responses after treatment with FL loaded with RSV (FL-RSV) in a mouse model was done in cooperation with the group of Prof. Zoltan Ungvari and Prof. Anna Csiszar at University of Oklahoma Health Science Center during a 2-month research stay.

For assessment of neurovascular coupling responses, mice were divided according to age in groups of young (3-month-old) and aged mice (24-month-old). Mice were retro-orbitally injected with FL-RSV diluted in PBS, corresponding to a dose of 2 mg/kg/day for four consecutive days by trained personnel. PBS and FL without RSV served as controls. 4 h after the last injection, mice were anaesthetized with isoflurane, endotracheally intubated and ventilated. Body temperature at approximately 37 °C was maintained by placement on a thermostatic heating pad. Rectal temperature of approximately 37 °C, blood pressure of 90-110 mmHg, and end-tidal CO₂ of 3.2 – 3.7 % were surveilled as published previously (154, 173, 174). Mice were immobilized on a stereotactic frame, the skull was exposed and thinned with a dental drill cooled by dripping buffer. The adaptability of neurovascular coupling

responses to somatosensory stimulation was assessed using laser speckle contrast imaging (**Figure 4.8**).

When coherent light like a laser beam illuminates a diffusive surface, laser speckles result from an interference pattern of scattered light. In the cerebral vasculature, red blood cells are scattering particles whose movement can be spatially and temporally resolved. The movement can be analyzed by quantifying the local spatial variance; thus, the movement intensity correlates with a spatial blurring of the speckle pattern. Hence, after neuronal stimulation, an endothelium-mediated adaptation of the cerebral blood flow can be determined by an increasing movement of red blood cells, as measured by a decrease in local spatial variance and contrast.

For visualization, the imager was placed with 10 cm working distance above the thinned skull, which was then illuminated with a divergent 785 nm laser. The whiskers were stimulated on one side for 30 s at 5 Hz as published previously (175). Differential perfusion maps of the brain vasculature were detected on the contralateral site from whisker stimulation before and after stimulation. Changes in the cerebral blood flow above the barrel cortex were monitored in 5-10 min intervals between stimulation in six trials. 20 min after systemic administration of the nitric oxide synthase inhibitor N ω -Nitro-L-arginine methyl ester (L-NAME, 10 mg/kg), the cerebral blood flow after whisker stimulation was monitored again as described.

The speckle pattern before whisker stimulation was set as baseline and relative change of the signal during stimulation was analyzed. To exclude unspecific changes of cerebral blood flow during stimulation, the relative change on the contralateral site to whisker stimulation was compared to unspecific changes on the same site of whisker stimulation. Measurement of neurovascular coupling responses after treatment was carried out by a blinded experimenter.

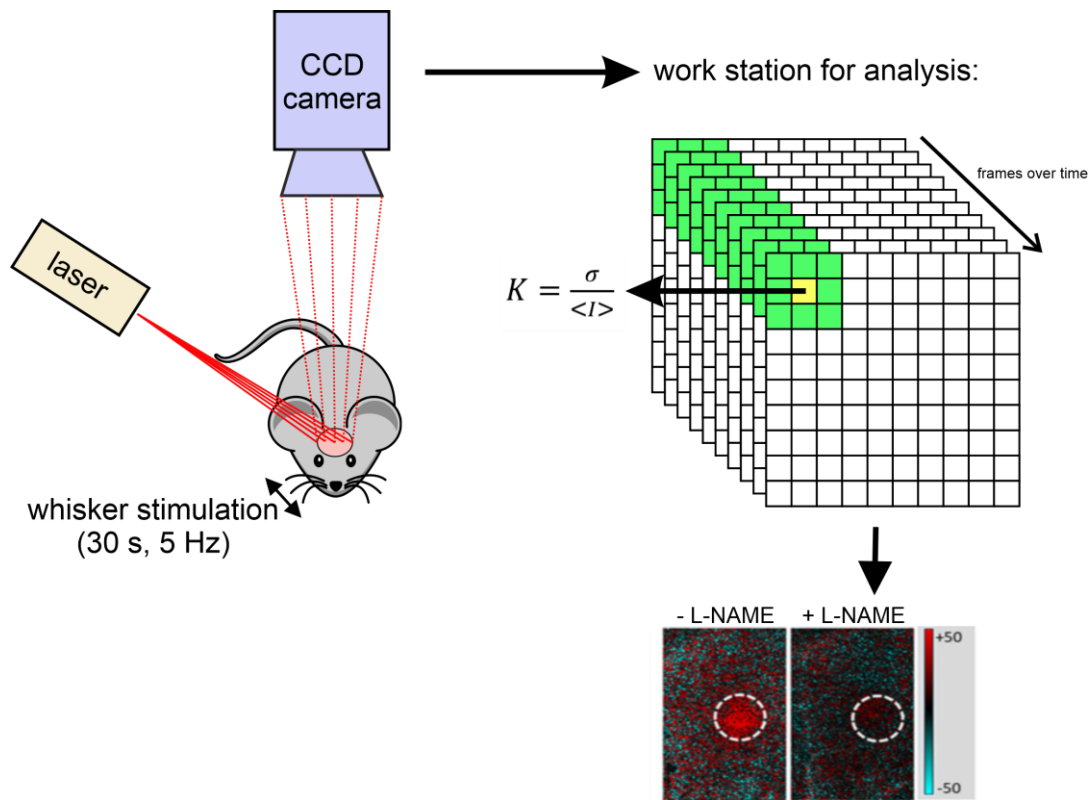


Figure 4.8. Schematic workflow of laser speckle contrast imaging. The skull of anesthetized mice was thinned down, and mice were placed in a laser speckle contrast imager with subsequent somatosensory stimulation. A diffused 785 nm laser was used to illuminate the barrel cortex, and the laser speckle pattern was detected with a CCD camera over time. The local laser speckle contrast (K) was calculated for each frame, which is the ratio of standard deviation (σ) to mean intensity ($\langle I \rangle$) of neighboring pixels (green in the displayed matrix) for the center pixel (yellow in the displayed matrix) and further related to a baseline measurement prior stimulation. Additional information to laser speckle contrast imaging and determination of changes in cerebral blood flow can be found in (176) and (177). Differential perfusion maps with representative regions of interests (dashed line) after somatosensory whisker stimulation are shown (bottom row), with +50 representing highest relative change of cerebral blood flow compared to the baseline (before whisker stimulation). L-NAME is an inhibitor of the nitric oxide synthase and can decrease NO-mediated neurovascular adaptability to neuronal stimulation. Figure is in part modified from (42).

4.2.6 Evaluation of biodistribution of fusogenic liposomes

Further experiments were done in cooperation with the group of Prof. Zoltan Ungvari and Prof. Anna Csiszar at University of Oklahoma Health Science Center during a 2-month research stay.

The analysis of biodistribution is a useful method for tracking FL after systemic administration during circulation and tissue localization. In this work, biodistribution was investigated in the living organism and after dissection. Using intravital microscopy, cerebral localization of FL was assessed and time-dependent elimination from the cerebral circulation was investigated. Further, liposomal tracer dye accumulation was tracked using fluorescence intensity measurements of dissected organs with a plate reader.

4.2.6.1 Fusogenic liposomes in the cerebral vasculature

Chronic cranial windows for *in vivo* imaging were prepared on young C57BL/6 mice as published previously (178, 179). In brief, mice were anesthetized with isoflurane, placed on a heating pad, and immobilized in a stereotactic frame. Subsequently, the head was disinfected, and the skull bone was exposed. A pneumatic dental drill was used to thin down a circular surface (\varnothing 3 mm), and craniotomy was performed. Subsequently, a sterile glass coverslip was applied on the dura mater and secured using liquid instant adhesive and acrylic resin. Mice were allowed to rest for at least 10 days after craniotomy and before intravital imaging.

The use of two-photon microscopy for intravital imaging of the cerebral vasculature has two key advantages compared to confocal microscopy. On the one hand, the excitation of the fluorophores is feasible by two photons of a longer wavelength compared to confocal (and other single-photon) microscopy (**Figure 4.9**), increasing the tissue penetration depth of the laser beam by reduction of light absorption of surrounding tissue. On the other hand, the fluorophore excitation is reduced from an illumination cone in confocal microscopy to a single spot in two-photon microscopy, enabled by non-linear excitation, additionally reducing out-of-focus illumination.

For intravital imaging, mice were anesthetized again and placed in the two-photon microscope FluoView 1000 MPE equipped with a XLPLN 25 \times water immersion objective and a MaiTai HP DeepSee-OL 690 – 1040 nm laser. DiD-labeled FL-RSV and fluorescein isothiocyanate (FITC)–dextran (500 kDa) were administered retro-orbitally 30 min before microscopy. Then the

cranial window was excited at 800 – 910 nm, and emission was detected using bandpass filters indicated in **Table 4.9**. Imaging before FL-RSV and FITC-dextran injection served as a control. All micrographs have been enhanced in brightness and contrast for visualization.

For the quantification of dynamic FL-RSV in the cerebral vasculature for several days, DiO-labeled FL-RSV and TR-dextran (70 kDa) were injected, then at least three regions of interest (frame interval 65 ms) of 2 animals equipped with a chronic cranial window were recorded for 30 s repeatedly at different time points (1 h, 24 h, 48h, 72 h, 96 h, 120 h and 144 h after administration). Dynamic FL-RSV signals were counted manually and quantified for the TR-dextran stained vessel lumen, and are further displayed as (vesicle) count per μm^3 (vessel lumen) per s.

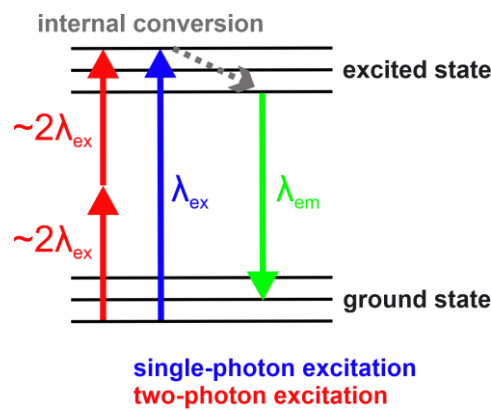


Figure 4.9. Jablonski diagram with a combined schematic view of single-photon and two-photon excitation. In epifluorescence and confocal microscopy, a photon of a specific wavelength excites the fluorophore (λ_{ex}) due to internal conversion. By emission of photons of a longer wavelength (λ_{em}), the fluorophore relaxes back to the ground state. In two-photon excitation, two photons of approximately the twofold wavelength can excite the fluorophore as well ($\sim 2 \lambda_{ex}$) if arriving almost simultaneously (~ 1 fs). Here, the excitation wavelength of both fluorophores is longer than the emission wavelength of the fluorophore.

Table 4.9. Bandpass filters used for fluorophores in intravital imaging.

Fluorophore	Bandpass filters (nm)
FL-DiO/ FITC-Dextran	495 – 540
FL-DiD/TR-dextran	575 – 630

4.2.6.2 Liposomal dye distribution in different tissues

Mice were treated with FL as described previously in **4.2.5.3**. Mice were humanely killed, perfused with PBS, and dissected 4 h after the last injection. Brain, lung, liver, kidney, and heart were removed and snap-frozen for measurement of fluorescence intensity of the liposomal dye DiD in the different tissues. For the measurement, tissues were homogenized with an ultrasonic cell disruptor homogenizer in PBS with 1 % Triton X-100 on ice. Homogenized samples were further centrifuged for 20 min at 4 °C and 15.000 rpm. The fluorescence intensity of DiD in the supernatant was measured at 680 nm (excitation wavelength: 644 nm) using the SPARK plate reader and normalized on organ mass. The fold change of FL-treated to PBS-treated samples is shown with standard deviation.

4.2.7 Data analysis

GraphPad Prism 7, Matlab R2019b, ImageJ, Imaris 9.5.0 and CorelDRAW were used for the analysis and presentation of data. BioDraw Ultra 12.0 was used for the visualization of chemical structures and schemes. Statistical analysis was carried out using Graphpad Prism on data of at least three individual experiments by parametric one-way ANOVA with Tukey's posthoc test, non-parametric Kruskal-Wallis test with Dunn's posthoc test or Wilcoxon signed rank test, all with $\alpha < 0.05$ being statistically significant.

5 Results

FL can enter the cell by membrane fusion, unassisted by fusion proteins or peptides, providing a fast and efficient way to deliver liposome cargo to the cytosol. Subsequent endosomal trafficking is circumvented, possibly enhancing availability of drugs entrapped in FL at their intracellular target sites. Thus, the application of FL as vehicles for drug delivery was investigated in the following chapter. While liposomes have been involved in approved drug formulation since the 1990s (4), the cellular uptake mechanism of FL by unassisted membrane fusion is an innovative form of delivery. Their application as drug delivery vehicles was explored in this work.

On the one hand, to predict target availability, change in delivery efficiency of a liposomal tracer dye to recipient cells was investigated in a breast cancer *in vitro* model with a modular BM, mimicking invasion events in malign tissue of the human mammary gland. On the other hand, the permeation of FL across (dys-)functional endothelial cell layer, highly relevant in systemic administration of drugs against cardiovascular diseases or cancer, was investigated to predict endothelial delivery, as well as possible extravasation and local accumulation.

The effects of drugs delivered with FL were examined for anti-cancer therapeutics ACL and DOX *in vitro* and the antioxidant RSV *in vitro* and *in vivo*. The robustness of the cellular drug delivery by membrane fusion was further tested by addition of serum proteins and the variation of cargo and its localization in the formulation.

Finally, the biodistribution and elimination of FL from cerebral circulation were investigated, including determining functional cargo effects in an *in vivo* model.

5.1 Impact of fusogenic liposome-assisted delivery at a cellular level

Membrane fusion of FL with mammalian cells is accompanied by the intercalation of the liposomal bilayer into the cell membrane, directly allowing a cargo release into the inner of the cell. Cell membrane fusion requires proximity of both bilayers, followed by a bilayer destabilization and fusion pore formation as an intermediate state with subsequent pore opening (see 3.1.2.1). The application of FL for the delivery of entrapped cargo to cultured cells has been shown numerous times (41, 44, 46-48). Yet, it is neither elucidated yet if small molecules can enter the cell during membrane fusion irrespectively of their entrapment in the liposomal formulation, nor if the circumvention of endocytosis increases cargo efficacy in any case.

5.1.1 Passive entry mediated by membrane fusion

To investigate whether a localization of small molecules inside FL is crucial for fusion-mediated cellular uptake, the membrane-impermeable dye PI was entrapped in FL to a final treatment concentration of 1.5 μM , with an entrapment efficiency of 84 % (Table 5.1). Loading of PI did not significantly alter zeta potential or size.

Table 5.1. Liposome characterization of fusogenic liposomes after loading with 1.5 μM PI or unloaded liposomes. Mean diameter (d), polydispersity index (PDI), zeta potential (ζ), and entrapment efficiency (EE) with standard deviation are shown ($n \geq 3$ independently prepared samples).

	d (nm)	PDI	ζ (mV)	EE (%)
FL	109 \pm 44	0.32 \pm 0.08	63 \pm 9	-
FL-PI	117 \pm 22	0.25 \pm 0.04	53 \pm 1	84 \pm 3

The influence of PI localization on the uptake in MCF 10A cells by membrane fusion was further investigated. PI uptake was compared for PI entrapped in FL (FL-PI) as characterized in Table 5.1, and PI supplemented to the FL solution after liposome formation (FL/PI) in similar treatment concentration. Visualization of membrane fusion and the uptake of fluorescent PI showed that PI was only internalized by cells if membrane fusion was present, the latter was indicated by the homogenous membrane staining of the liposomal tracer dye DiR (Figure 5.1). After treatment of MCF 10A cells with FL but not PI, a negligible background of DiR emission is visible in the PI channel.

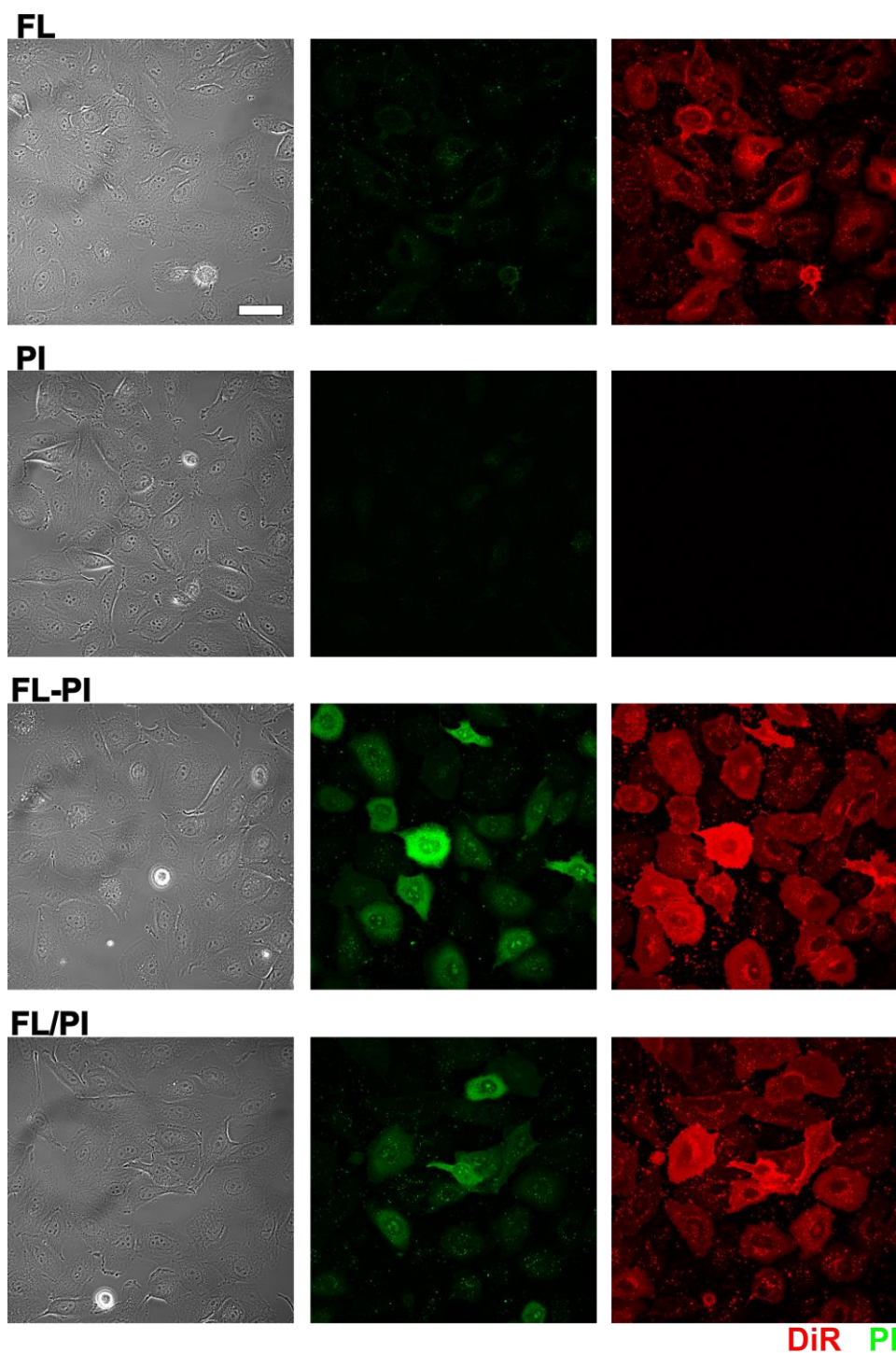


Figure 5.1. Uptake of membrane-impermeable propidium iodide (PI) by MCF 10A cells using fusogenic liposomes (FL). PI is entrapped in FL during liposome preparation (FL-PI), or supplemented to the treatment solution after liposome formation (FL/PI). The final treatment concentration of PI was 1.5 μ M irrespectively of formulation; PI only, and FL without PI served as controls. PI uptake was visualized using confocal laser-scanning microscopy. Scale bar 50 μ m, applies to all.

PI uptake was also observed if PI was only supplemented to the FL solution (FL/PI). Thus, an additional uptake mechanism of PI, present in FL solution without insertion into liposomes during lipid film hydration, could be demonstrated. PI in FL/PI is neither inserted into the liposomal bilayer nor the liposomal lumen. Thus, this uptake was further termed passive, since it is not actively caused by merging of membranes due to bilayer insertion or the unification of liposomal lumen and cell cytosol.

5.1.2 Circumvention of lysosomal sequestration

To further identify the applicability of FL as nano-carriers for therapeutic agents, two anti-cancer therapeutics with different chemical characteristics were investigated, namely doxorubicin (DOX) and aclacinomycin a (ACL). ACL and DOX belong to the structural class of anthracyclines; however, ACL is less basic and more lipophilic than DOX (see **4.1.1**). In this work, ACL and DOX were entrapped in FL in final treatment concentrations of 0.6 and 1.8 μM , respectively. These concentrations have shown to significantly reduce cell proliferation in previous studies (43, 49). As a control, liposomes that mimic the composition of Doxil, an approved liposomal formulation of DOX, were additionally prepared and termed PEGylated, endocytic liposomes (PEG-EL), respective to their stealth liposomal composition and cellular uptake mechanism. For comparison of liposomal compositions please refer to **4.2.1.1**.

Upon size and zeta potential comparison of all formulations, the size was 85 – 163 nm, and increasing if PEG-EL composition was investigated (**Table 5.2**). The zeta potential was positive for FL and negative for PEG-EL, yet it was not affected by drug loading. Zeta potential of FL ranged 63 – 69 mV, while zeta potential for PEG-EL ranged -29 – -48 mV. The entrapment efficiency of both anthracyclines was determined using ultrafiltration of the liposomal formulations. It was $\geq 88\%$ in all formulations (**Table 5.2**). Due to high entrapment efficiencies and a further dilution of the liposomal formulation for treatment, the remaining free drug in the formulation was considered negligible and liposomal formulations without purification were used in the remainder of the studies.

Table 5.2. Liposome characterization of FL and PEG-EL after encapsulation of 0.6 μM ACL and 1.8 μM DOX or unloaded liposomes. Mean diameter (d), polydispersity index (PDI), zeta potential (ζ), and entrapment efficiency (EE) with standard deviation are shown ($n \geq 3$). Data were partially published in (43).

	d (nm)	PDI	ζ (mV)	EE (%)
FL	109 \pm 44	0.32 \pm 0.08	63 \pm 9	-
FL-ACL	87 \pm 14	0.28 \pm 0.03	64 \pm 25	92 \pm 6
FL-DOX	85 \pm 4	0.29 \pm 0.02	69 \pm 5	88 \pm 6
PEG-EL	163 \pm 78	0.46 \pm 0.24	-29 \pm 18	-
PEG-EL-ACL	152 \pm 46	0.42 \pm 0.15	-47 \pm 5	89 \pm 4
PEG-EL-DOX	142 \pm 44	0.39 \pm 0.12	-48 \pm 10	90 \pm 6

Further, the uptake and localization of ACL and DOX formulated in FL or PEG-EL into MCF 10A cells was investigated, with anthracyclines in PBS serving as controls. Membrane fusion of FL-ACL and FL-DOX was visualized based on the fusion-mediated membrane intercalation of the liposomal tracer dye DiR, which was added to the FL and PEG-EL formulation in similar amounts (**Figure 5.2**).

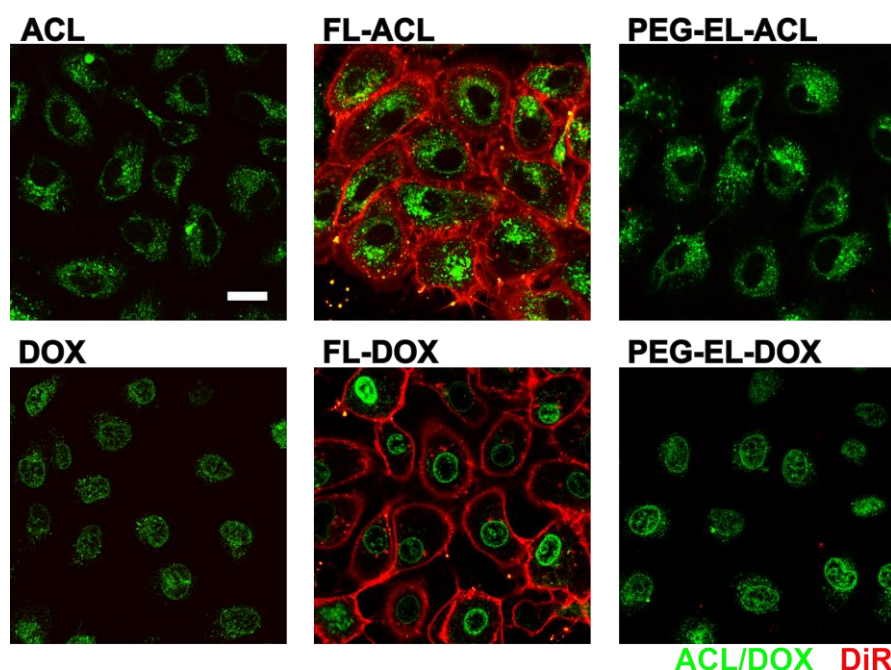


Figure 5.2. Formulation-independent localization of the anthracyclines aclacinomycin a (ACL) and doxorubicin (DOX). For visualization of the anthracycline localization after 10 min treatment duration, treatment concentrations of ACL and DOX were increased to 6 μM and 9 μM . Scale bar 20 μm applies to all.

Additionally, the anthracycline scaffold of ACL and DOX enabled the intracellular visualization of both drugs. ACL was localized in substructures close to the nucleus and DOX inside the nucleus, as observed before (49). Yet, this was observed irrespectively of formulation in FL, PEG-EL, or PBS. Here, the formulation did not alter the localization of either drug inside the cell. However, both drugs in comparison were not localized in similar compartments, despite their structural similarity, pointing towards possible differences in their pharmacological effects.

To assess the cytostatic effects of ACL and DOX inside all formulations, proliferation after anthracycline treatment was monitored in MCF 10A cells for three days using an EdU incorporation assay. Here, proliferating cells were labeled by incorporation of the thymidine analog EdU into newly synthesized DNA, which was subsequently coupled to Alexa Fluor™ 488 and visualized using confocal laser-scanning microscopy (**Figure 5.3A**).

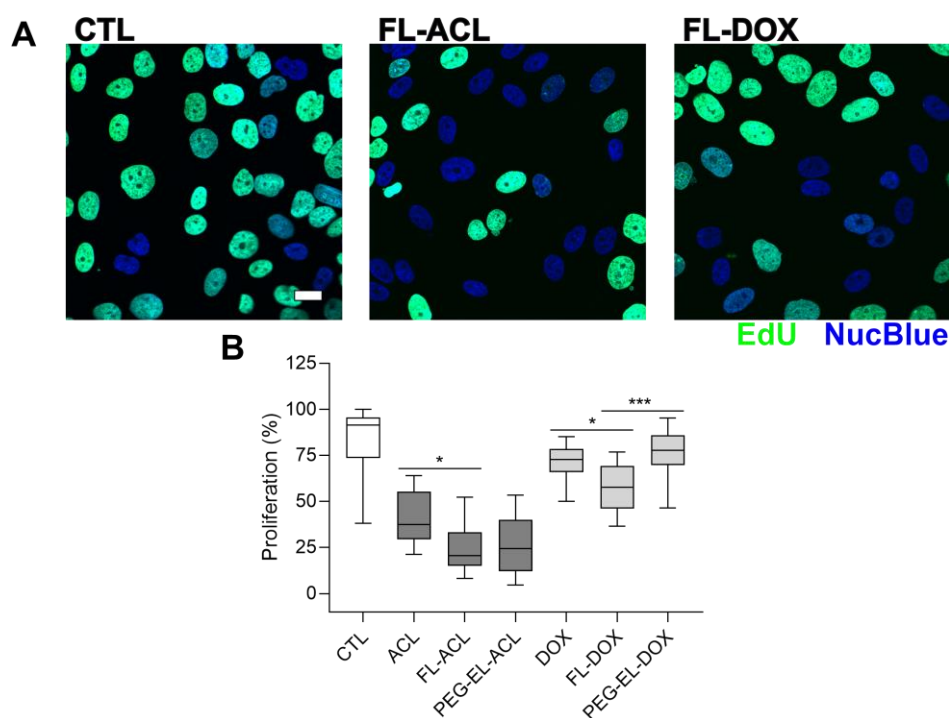


Figure 5.3. Anti-proliferative effects of the anthracyclines aclacinomycin a (ACL) and doxorubicin (DOX) in different formulations in MCF 10A cells. (A) In each formulation, 0.6 μ M ACL or 1.8 μ M DOX was used, and proliferation was monitored after 72 h using confocal laser-scanning microscopy. PBS-treated cells served as control. (B) For proliferation quantification, the ratio of Edu-labeled nuclei to all NucBlue-labeled nuclei was calculated. Statistical analysis was done using the non-parametric Kruskal-Wallis test with posthoc Dunn's test (*: $p < 0.05$; ***: $p < 0.001$; $n \geq 4$ experiments and ≥ 25 analyzed images per parameter). Data was published in (43).

All anthracycline formulations reduced MCF 10A proliferation in the monitored time frame compared to untreated cells except PEG-EL-DOX. The anti-proliferative effect of DOX measured as proliferation reduction was significantly increased by formulation in FL in comparison to PEG-EL (p-value = 0.0005) or PBS (p-value = 0.0457). FL-ACL reduced proliferation compared to ACL in PBS (p-value = 0.0179), yet no further proliferation reduction could be observed compared to PEG-EL-ACL (**Figure 5.3B**).

To sum up this subchapter, membrane-impermeable dye PI was delivered to MCF 10A cells in the presence of FL, also by supplementation after liposome formation. Additionally, the anthracyclines ACL and DOX showed differential intracellular compartmentalization in MCF 10A cells independent of the formulation. However, FL entrapment of both compounds significantly increased their anti-proliferative effects in comparison to free drug. Simultaneously, formulation of DOX in FL improved anti-proliferative effects, while PEG-EL formulation failed to significantly reduce proliferation.

5.2 Fusogenic liposome-assisted delivery across the extracellular matrix

A prolonged circulation time of liposomal drug delivery systems, as introduced for stealth liposomes in 3.1.2, allows accumulation, especially on tumor sites with leaky vasculature. However, the availability of liposomal cargo at the intracellular target can be highly inefficient due to the endosomal uptake and trafficking. The reduced availability is even more pronounced by PEG coating, reducing cellular interaction of the nanoparticle even further. Several studies indicated that less than 1 % of nanoparticles passively targeted to the tumor are delivered to the target site (180). Due to the alternated uptake mechanism to cells by membrane fusion, FL might overcome the problem of target availability. In this chapter, the applicability of FL as nano-carriers for anti-cancer therapeutics was investigated for the delivery to a three-dimensional model of breast cancer with a modular BM. Here, the possibility of penetration of the ECM, including a separated investigation of the BM, and the cellular uptake and effects of anti-cancer therapeutics ACL and DOX was investigated.

5.2.1 Culturing of three-dimensional models

To initially assess if FL were able to penetrate the ECM-mimicking Geltrex matrix, FL labeled with DiI or DiR were applied to a cell-free Geltrex bed, which was formed on top of fluorescein-BSA coated high-precision microscopy glass (see 4.2.3.1). Confocal laser-scanning microscopy was used to visualize the penetration depth of DiI- or DiR-labeled FL 24 h or 48 h after their individual application at the end of the experiment. Ortho projection of imaging stacks indicated no differential penetration of FL inside the Geltrex bed within the 24 h delay (**Figure 5.4A**). Upon normalization of the mean grey value for each frame of the image stack, an overlap of the differently labeled FL signals was shown. The lack of change in main peak position indicated no additional penetration of FL-DiR into the Geltrex layer compared to FL-DiI applied with 24 h delay (**Figure 5.4B**).

Geltrex mainly consists of the BM-associated proteins laminin, collagen IV, entactin, and heparan sulfate proteoglycans. Collagen IV is of key importance for network formation of the BM protein meshwork. However, in the interstitial matrix, a diverse set of collagens is present to provide structural support, e.g., the fibrillar collagen I, also commonly used as a substrate in cell culture applications (181). To assess whether the penetration of FL was altered if fibrillar collagen was present in the interstitial matrix, differently labeled FL were applied again with

a time delay to a collagen I gel. Here, no noteworthy time-dependent penetration into the gel layer in the image stack or after quantification was detected as well (**Figure 5.4C and D**). Hence, a substantial penetration of FL through the ECM-like substrates Geltrex and collagen I was not detected within 24 h.

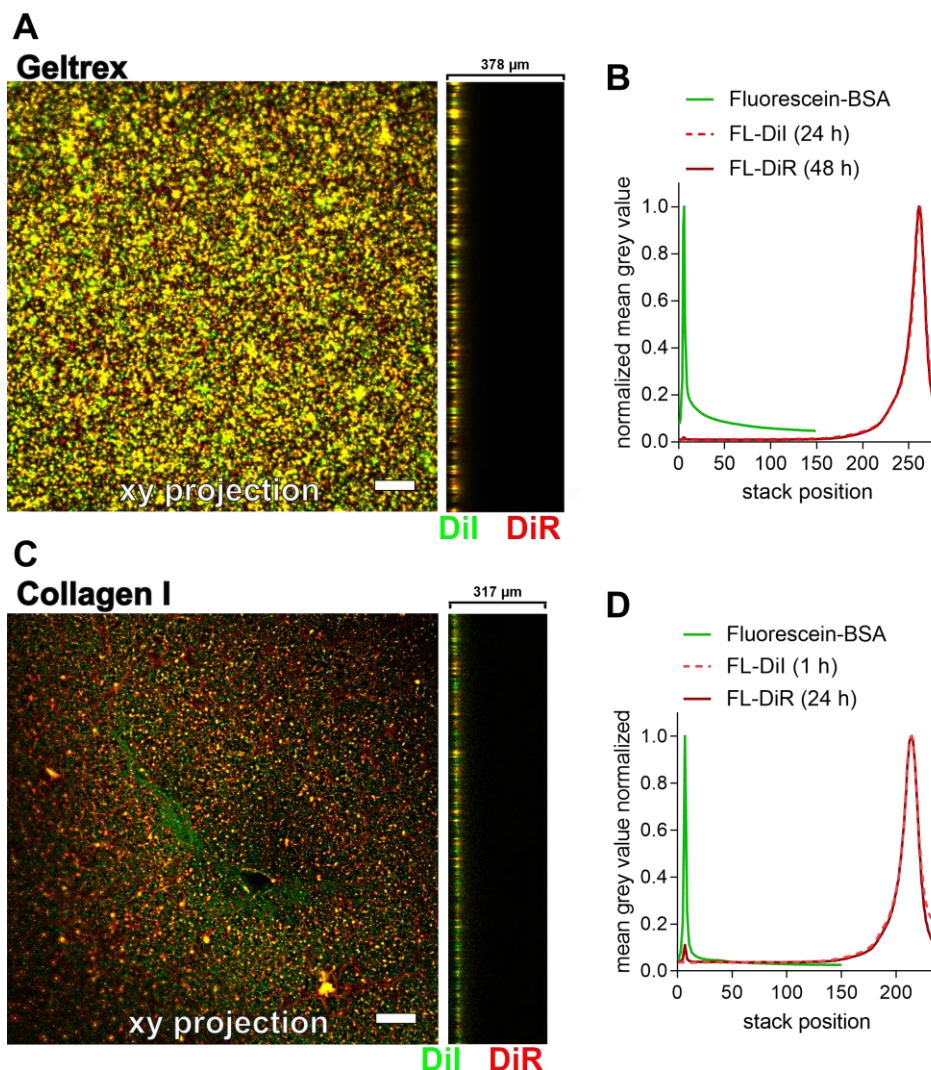


Figure 5.4. Penetration of fusogenic liposomes containing DiR or DiI after indicated incubation times, after administration onto a gel layer of Geltrex and collagen I. (A+C) XY and ortho projections are shown to indicate the penetration depth in both ECM-like substrates, respectively. Scale bar 50 μm . Normalized mean grey value intensities of each stack position are shown for fluorescein-BSA, FL-DI, and FL-DiR for (B) Geltrex and (D) collagen I. Mean grey values were normalized on the highest signal for each channel to facilitate comparison.

Three-dimensional cell culture models used to investigate the application of FL as nano-carriers in cancer therapy were based on the non-tumorigenic epithelial MCF 10A cell line of

the mammary gland and the highly invasive triple-negative breast cancer cell line MDA-MB-231. Three-dimensional culture led to the development of model acini as observed in the mammary gland (**Figure 5.5** left panel), composed of baso-apically polarized cells and a self-secreted BM as previously published (165). Culturing MDA-MB-231 cells on a Geltrex bed led to morphological heterogeneities, as shown in **Figure 5.5** right panel. While some cell clusters obtained a rounded morphology as observed for MCF 10A acini, others showed grape-like structures, besides network-forming growth on the Geltrex bed.

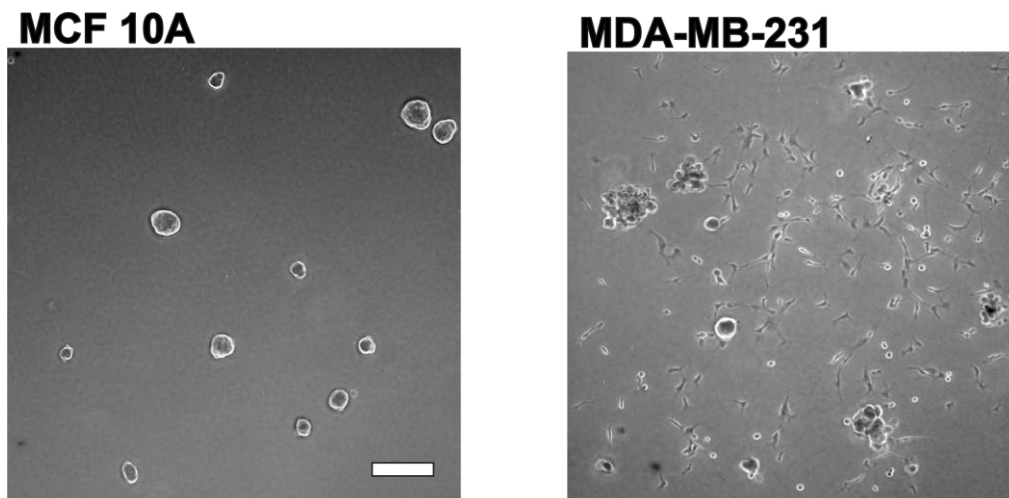


Figure 5.5. Formation of MCF 10A acini and MDA-MB-231 spheroids on a Geltrex bed, cultured for 10 or 9 days, respectively. Scale bar 200 μ m applies to both.

To further evaluate FL-mediated delivery of liposomal tracer dye DiR to cells of both models, incorporation of DiR was visualized by confocal laser-scanning microscopy. Fusion of cells inside FL-treated MCF 10A acini was observed due to homogenous membrane staining with DiR (**Figure 5.6**). Additionally, a speckled DiR localization on the surface of the acinus was detected. Fusion was also observed for MCF 10A acini treated with EGF. MCF 10 acini treatment with EGF was previously demonstrated to promote cell proliferation, loss of acinar polarization and BM lesions (65). For spheroids of the highly invasive MDA-MB-231 cell line, fusion was reduced in comparison to MCF 10A acini and primarily observed for cells growing on the glass surface. To further assess whether the observed fusion reduction in MDA-MB-231 spheroids was associated with ECM protein secretion, collagen IV, a critical protein of the BM meshwork, was immunofluorescently labeled. The epithelial-mesenchymal transition is

marked by degradation and invasion of the BM (69-71) and MDA-MB-231 represent transitioned highly invasive breast cancer cells. Still, secretion of collagen IV on the cell surface could be observed (**Figure 5.7A**). Yet, no functional BM could be formed as indicated by the absence of laminin 332 secretion, another crucial component and initiator of BM formation (**Figure 5.7B**).

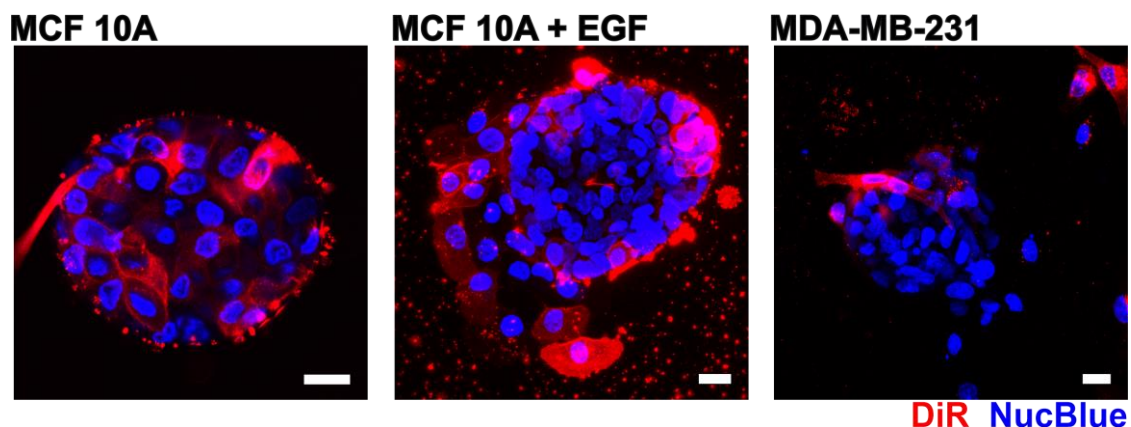


Figure 5.6. MCF 10A acini with or without EGF treatment and a MDA-MB-231 spheroid after FL treatment. Fusion is visualized by homogenous DiR membrane staining. An optical slice of an MCF 10A acini is shown, maximum intensity projections are shown for an MCF 10A acinus treated with EGF for 30 h and a MDA-MB-231 spheroid. Scale bars 20 μm .

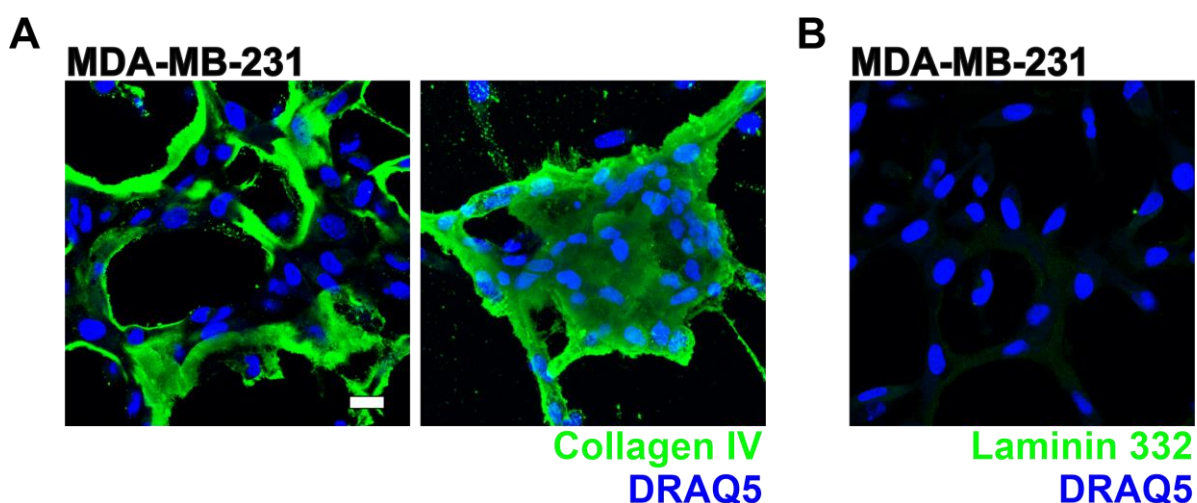


Figure 5.7. Collagen IV and laminin 332 secretion of MDA-MB-231 cells cultured on a Geltrex bed. Nuclei are labeled with DRAQ5. (A) Micrograph of a cellular network and maximum intensity projection of a spheroid image stack stained for collagen IV are shown. (B) Laminin 332 staining of MDA-MB-231 cells indicated no significant secretion. Scale bar 20 μm applies to all.

5.2.2 Penetration of the basement membrane

The BM secreted by MCF 10A acini is adjustable in maturation state and integrity due to cultivation parameters (65, 165). To further specify the impact of BM-protein interaction for

FL delivery, the uptake of liposomal tracer dye DiR into cells of the MCF 10A acini was investigated after administration of FL or PEG-EL with respect to the maturation state of the BM by alteration of cultivation time. Treatment of low-developed acini with a low-matured BM (ld) with FL resulted in membrane fusion of cells inside the acinus, as observed by the homogenous DiR membrane staining (**Figure 5.8**; ld+FL).

Additionally, a speckled tracer dye pattern could be observed on the interface of cells and medium, hinting towards a sticking of FL to the low-matured BM. After treatment with PEG-EL, no notable interaction or DiR uptake was observed, irrespectively of BM maturation state (**Figure 5.8**; ld+PEG-EL and hd+PEG-EL). If the BM was more matured and acini were treated with FL, as can be observed in high-developed acini (hd), an interaction of DiR with the BM could only be observed sparingly (**Figure 5.8**; hd+FL).

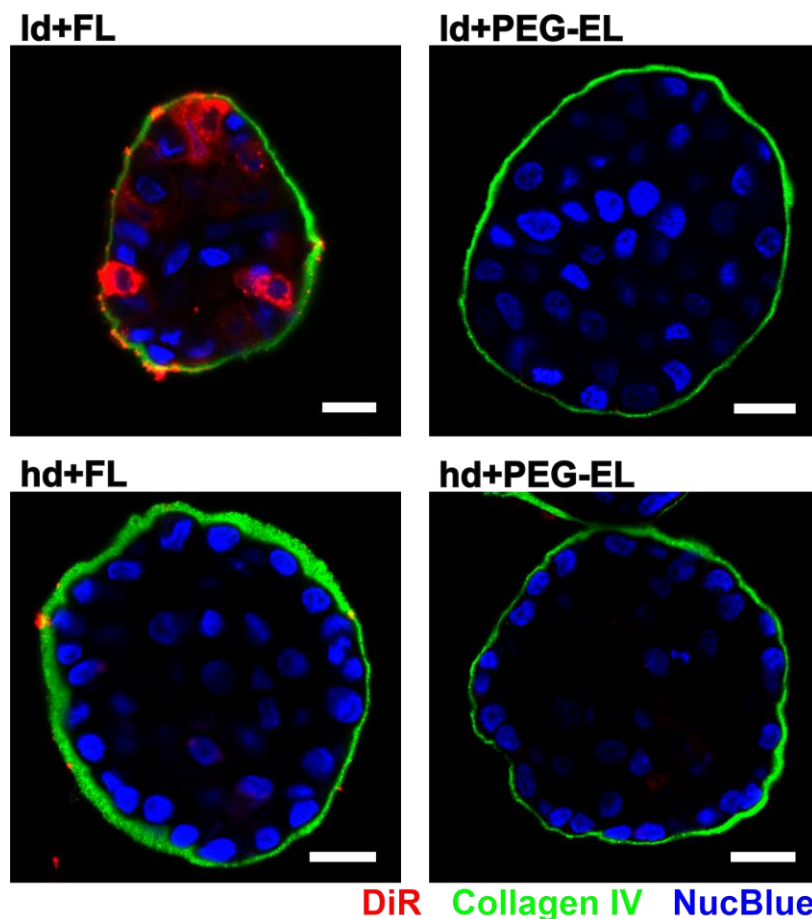


Figure 5.8. Interaction of fusogenic and endocytic liposomes with the basement membrane of low- (ld) and high-developed (hd) MCF 10A acini. Optical slices of MCF 10A acini treated with fusogenic and pegylated, endocytic liposomes (FL and PEG-EL) and subsequent immune fluorescent staining of collagen IV and cell nuclei are shown. Scale bars 20 μ m.

Uptake of DiR in cells of the MCF 10A acini was quantified by determining the relative change of median DiR fluorescence intensity of single cells compared to PBS treated controls, using flow cytometry. Here, a low maturation state of the BM did increase the uptake of DiR after FL administration compared to PEG-EL (ld: FL vs. PEG-EL, p-value = 0.0305), while this was not observed in hd acini with a more matured BM (**Figure 5.9**). Uptake of DiR after FL treatment compared to PEG-EL treatment could be additionally increased by treatment of acini with EGF. This was shown before to initiate MCF 10A transition within the acinus towards a more invasive phenotype (65) due to its pathophysiological involvement in breast cancer onset. FL treatment increased the uptake of DiR compared to PEG-EL treatment irrespectively of BM maturation state if acini were pretreated with EGF (ld+EGF: FL vs. PEG-EL, p-value = 0.0018; hd+EGF: FL vs. PEG-EL, p-value = 0.0010) (**Figure 5.9**).

To further confirm the involvement of the BM status in relative changes of DiR uptake after FL treatment, the BM of MCF 10A acini was disrupted prior to FL treatment by digestion with collagenase IV (C4ase). C4ase treatment disrupted the BM meshwork of laminin 332 and collagen IV (**Figure 5.10A**). Furthermore, pretreatment of high-developed acini with C4ase led to DiR uptake comparable to EGF-pretreated MCF 10A acini (**Figure 5.10B**), confirming the BM-restricted delivery of DiR by FL.

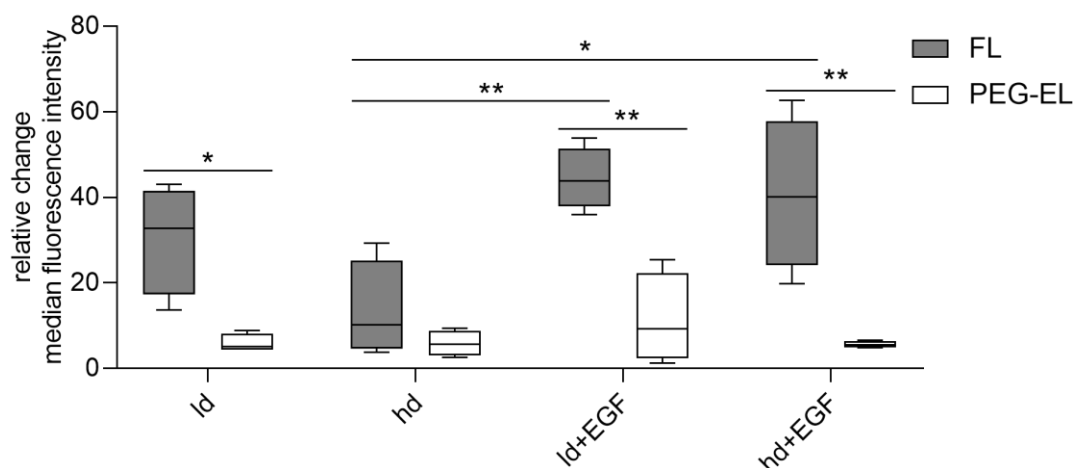


Figure 5.9. Analysis of median DiR fluorescence intensity in cells of low- (ld) or high-developed (hd) MCF 10A acini and subsequent treatment with fusogenic liposomes (FL) or pegylated endocytic liposomes (PEG-EL). Basement membrane integrity was altered by treatment with epidermal growth factor (EGF) triggering MCF 10A invasion onset. Mean relative change of median fluorescence intensity is shown as box plots and statistical analysis was done using one-way ANOVA with posthoc Tukey's test (*: $p < 0.05$; **: $p < 0.01$; $n=4$ experiments). Data were published in (43).

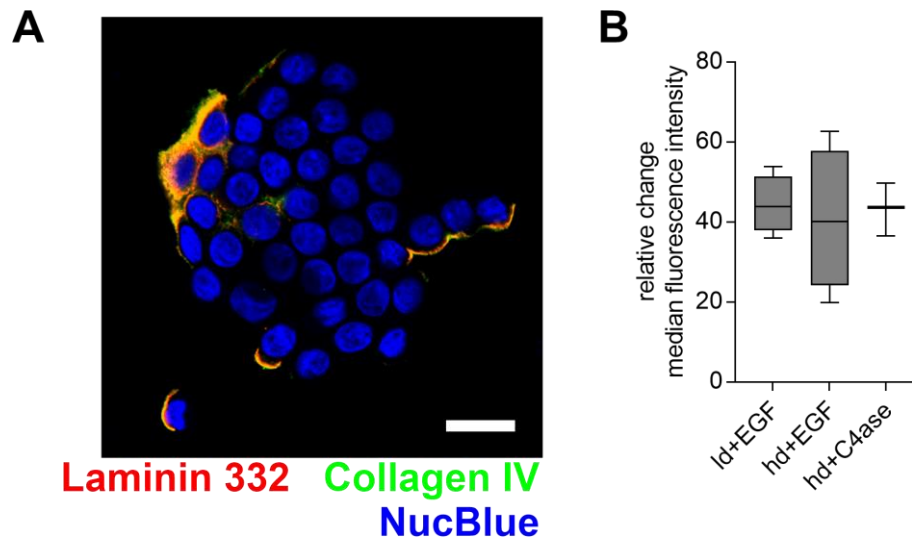


Figure 5.10. Digestion of the basement membrane by collagenase IV (C4ase) of an MCF 10A acinus with a high-developed basement membrane is shown. (A) XY-projection of a high-developed (hd) MCF 10A acini treated with C4ase and subsequent immune fluorescent staining of collagen IV and cell nuclei. Scale bar 20 μ m. (B) Analysis of median DiR fluorescence intensity in cells of the MCF 10A acini model after treatment with FL in epidermal growth factor (EGF) or C4ase treated, Id and hd acini. Relative change of median fluorescence intensity is shown as box plots ($n \geq 3$ experiments). Results of statistical analysis using one-way ANOVA with posthoc Tukey's test indicated no significant differences. Data were published in (43).

5.2.3 Fusogenic liposome-assisted delivery of anti-cancer therapeutics

The BM is a key structural feature of the ECM and a known barrier for the passage of endogenous macromolecules (76, 79). Lesions of the BM in solid tumors mark the initiation of invasion and metastasis, and are associated with poor prognosis (69, 88). To further investigate the BM's impact as an invasive barrier on delivery and resulting effects of anti-cancer therapeutics ACL and DOX, anti-proliferative effects of the anthracyclines in cells of the MCF 10A acini model were examined. Here, the EdU incorporation assay was used to analyze the proliferation rate of Id acini after treatment with anti-cancer therapeutics formulated in FL and PEG-EL. PBS treated samples served as control and reached a proliferation percentage of 63 % three days post-treatment (**Figure 5.11**).

As visualized in **Figure 5.11**, control samples showed a loss of acinar morphology, and cells started to form a proliferation-induced two-dimensional layer on the glass surface. Treatment with ACL and DOX encapsulated in FL, on the other hand, reduced proliferation and the layer-like growth of cells. Upon quantifying imaging data and in accordance with results from **5.1.2**, all formulations reduced proliferation significantly besides treatment with PEG-EL-DOX.

Treatment with DOX encapsulated in FL reduced proliferation significantly compared to PEG-EL-DOX (p-value = 0.0005), while there was no significant difference if ACL was administered in different formulations (**Figure 5.11**).

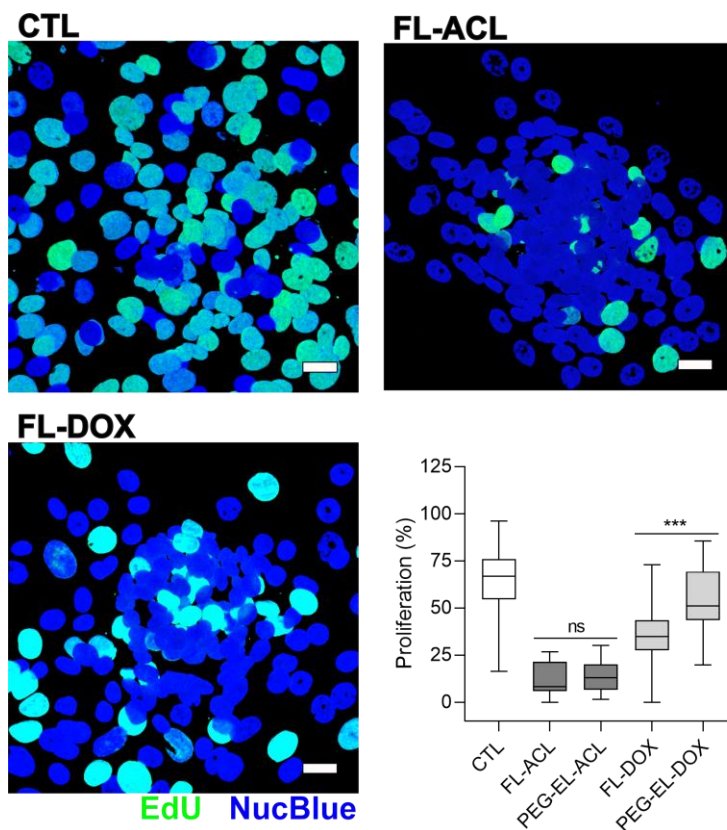


Figure 5.11. Anti-proliferative effects of the anthracyclines aclacinomycin a (ACL) and doxorubicin (DOX) in different formulations in the low-developed MCF 10A acini model. In each formulation, 1.8 μ M DOX or 0.6 μ M ACL were used. Effects were analyzed by EdU-labeling of nuclei and subsequent laser-scanning confocal microscopy, quantified using the ratio of EdU-labeled to all cell nuclei. 3D-projections are shown. Scale bars 20 μ m. The non-parametric Kruskal-Wallis test with posthoc Dunn's test was used for statistical analysis (***: $p < 0.001$; $n \geq 3$ experiments and ≥ 21 analyzed images per parameter). Data were partially published in (43).

Further, the effects of DOX treatment on hd acini with a more mature BM were investigated. Previous data indicated a drastically reduced uptake of liposomal tracer dye DiR in FL, if not being previously supplemented with EGF (see 5.2.2). Here, the proliferation of control samples was 31 %, and treatment with DOX neither in FL nor PEG-EL did change proliferation significantly (**Figure 5.12**).

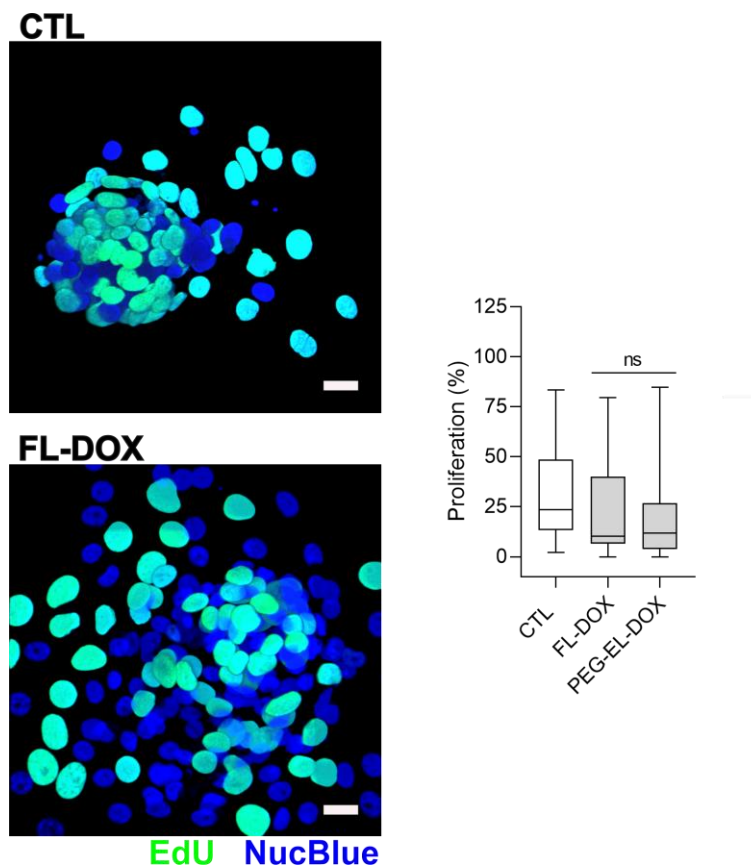


Figure 5.12. Anti-proliferative effects of the anthracycline doxorubicin (DOX) in different formulations in the high-developed MCF 10A acini model. In each formulation, 1.8 μM DOX was used. Effects were visualized by detection of EdU-labeled nuclei of proliferated cells using laser-scanning confocal microscopy. 3D-projections are shown. Scale bars 20 μm . Quantification was done using the ratio of EdU positive to all cell nuclei. The non-parametric Kruskal-Wallis test with posthoc Dunn's test was used for statistical analysis ($n=3$ experiments and ≥ 20 analyzed images per parameter). Data were partially published in (43).

The results of this subchapter reveal that FL did not permeate ECM-like gels of Geltrex and collagen I. Additionally, spheroids of highly invasive MDA-MB-231 cells showed drastically reduced FL uptake compared to MCF 10A acini and a BM-independent collagen IV secretion. However, FL demonstrated a BM-dependent uptake into the MCF 10A acini model in contrast to PEG-EL, which additionally influenced the anti-proliferative effects of anti-cancer therapeutic DOX, while there was no effect on ACL.

5.3 (Trans-)endothelial delivery mediated by fusogenic liposomes

The vascular endothelium has a critical function in the regulation of thrombic and inflammatory activity. It is additionally involved in the regulation of nutrient supply by vascular tone and permeability changes. Hence, functionality of the endothelium is of relevance in various cardiovascular diseases, and the induction of hyperpermeability was demonstrated to enable tumor nutrient supply in cancer (see 3.3.2.2). The application of drug delivery systems, such as liposomes, is described for diseases with dysfunctional vascular endothelium. For instance, the enhanced permeability and retention effect described for stealth liposomes causes an accumulation in solid tumors with leaky vasculature (see 3.1.2). Therefore, an *in vitro* investigation of the consequences of compromised vascular endothelium for FL extravasation was done in the following subchapter. Additionally, the possibility to rebalance ROS activity by antioxidant delivery and resulting effects on endothelial permeability was explored.

5.3.1 Establishment of an endothelial barrier model

To analyze the possibility of drug passage through endothelial layer, primary HUVECs were seeded on porous cell culture inserts in a well plate, simulating a luminal site for FL and TR-dextran administration and a basolateral site for permeability analysis using fluorescence spectroscopy. The formation of tight and adherens junctions between endothelial cells was confirmed by immune fluorescence of the endothelial adherens junctions marker VE-Cad and the tight junctions marker claudin-1, which were localized in the membranes of neighboring cells (**Figure 5.13A**), indicating a passage restriction for macromolecules. After luminal treatment with TR-dextran (10 kDa) or FL, 16.0 ± 7.5 % of applied TR-dextran and 2.6 ± 2.3 % FL passed to the basolateral site, confirming a significant restriction across primary HUVECs (p -values = 0.0156) and, thus, a possible barrier function (**Figure 5.13B**).

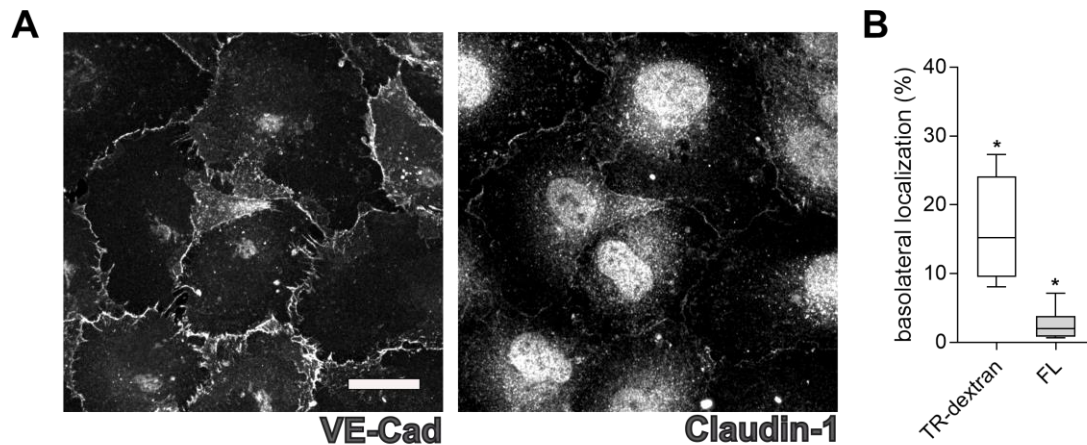


Figure 5.13. Barrier function of primary human umbilical vein endothelial cells (HUVECs). (A) Immune fluorescence of HUVECs seeded in cell culture inserts demonstrated a membrane localization of adherens junction protein VE-cadherin (VE-Cad) and tight junction protein claudin-1. Maximum intensity projections are shown, scale bar 20 μm applies to both. (B) Passage of TR-dextran and FL across HUVECs was investigated by fluorescence intensity measurements in the basolateral compartment and normalized on fluorescence intensity of the initial treatment solution. Box plots are shown and the non-parametric Wilcoxon signed rank test was used for statistical analysis (*vs. 100 %: $p < 0.05$; $n=6$ experiments and 7 analyzed samples per parameter).

5.3.2 Liposome passage through dysfunctional endothelium

Due to its relevance for extravasation of macromolecules, the dysfunctional vascular endothelium is a potential target for drug delivery in anti-angiogenic and anti-geronic drug development (see 3.3.2.2). Hence, passage of FL and TR-dextran was investigated after ROS induction by CH treatment and permeability-inducing growth factor stimulation. CH and VEGF treatment resulted in discontinuous membrane localization of ZO-1, as indicated by immune fluorescence and subsequent confocal laser-scanning microscopy (Figure 5.14A). ZO-1 is a scaffolding protein involved in the maintenance of adherens and tight junctions, discontinuities in ZO-1 membrane localization are thus a consequence of discontinuous intercellular junctions (182). CH treatment additionally increased ROS activity significantly (p -value = 0.0039), while treatment with VEGF failed to evoke a change in ROS activity (Figure 5.14B). Thus, an alteration of intercellular junctions could be demonstrated by CH-mediated induction of ROS activity and ROS-independently by VEGF treatment. Further, the impact of ROS activity caused by CH treatment and discontinuities in the intercellular junctions, as observed after VEGF treatment, on macromolecule passage were investigated. CH treatment significantly increased the relative passage of TR-dextran and FL (p -values = 0.0078), while

relative passage after VEGF treatment only increased for FL (p-value = 0.0313), but not TR-dextran (Figure 5.14C).

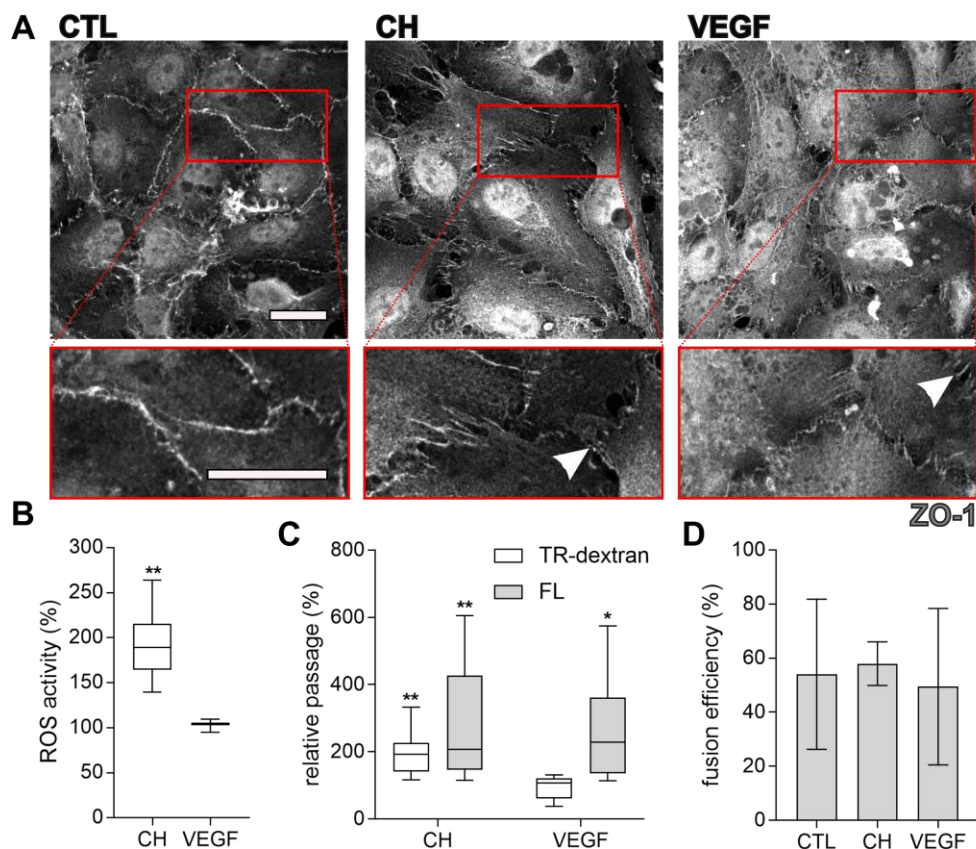


Figure 5.14. Permeability of a primary HUVECs after ROS induction and VEGF stimulation. (A) Immune fluorescence of zonula occludens-1 (ZO-1) indicates discontinuities of the membrane localized signal after CH and VEGF treatment (white arrows). Maximum intensity projections are shown, scale bar 20 μm applies to all micrographs and magnifications. (B) A CM-H₂DCFDA assay was used to determine ROS activity in primary HUVECs after CH and VEGF treatment. ROS-induced oxidation of DCFDA was monitored by formation of fluorescent DCF. (C) Relative passage of TR-dextran and FL was analyzed after treatment with CH or VEGF. Fluorescence intensities in B and C were normalized on untreated controls. Box plots are shown and the non-parametric Wilcoxon signed rank test was used for statistical analysis (* vs. 100 %: $p < 0.05$; ** vs. 100 %: $p < 0.01$; $n \geq 3$ experiments and ≥ 3 analyzed samples (B) or ≥ 6 analyzed samples (C)). (D) Fusion efficiency was analyzed after treatment with CH or VEGF and subsequent fusion (15 min) using confocal laser-scanning microscopy and quantification with an in-house developed Matlab routine for image analysis (see 4.2.4.3). Mean with standard deviation is shown ($n=3$ experiments). Results of statistical analysis using Kruskal-Wallis test with posthoc Dunn's test indicated no significant differences.

Endothelial dysfunction was demonstrated to include glycocalyx shedding and degradation (see 3.3.2.1), altering the luminal surface of endothelial cells. Hence, the fusion ability of FL with primary HUVECs was investigated after CH or VEGF treatment using laser-scanning

Results

microscopy followed by image analysis for quantification. No significant changes in fusion efficiency of >49 % for all parameters were observed (**Figure 5.14D**).

5.3.3 Fusogenic liposome-assisted delivery of resveratrol to the endothelium

An imbalanced production and subsequent ROS activity inside endothelial cells can have severe pathophysiological consequences, including hypertension and cognitive decline. Thus, a rebalancing of the redox system of vascular endothelium has a therapeutic benefit, as can be observed for various applications of the polyphenolic compound RSV, which exerts strong antioxidant effects, yet has poor pharmacokinetics (see **3.3.2.2**).

To further investigate beneficial effects of RSV loaded to FL (FL-RSV) on primary HUVECs, FL-RSV labeled with various dyes were initially characterized. While the size after loading partially increased, zeta potential remained positive, and loading with RSV was > 74 % (**Table 5.3**). Due to interference of the DiD fluorophore excitation/emission range in zetasizer measurements, size and zeta potential could not be determined for DiD-labeled FL and FL-RSV.

Table 5.3. Liposome characterization of FL after encapsulation of RSV or unloaded liposomes. DiD was exchanged for dye analogues DiI, DiO and DiR for size and zeta potential determination. Mean diameter (d), polydispersity index (PDI), zeta potential (ζ) and entrapment efficiency (EE) with standard deviation are shown, if applicable. EE was determined as described in 4.2.1.3 for FL-RSV formulations used in *in vitro* and *in vivo* experiments. The non-parametric Kruskal-Wallis test with posthoc Dunn's test was used for statistical analysis (* vs. FL(DiO): p = 0.0260; n \geq 3 independently prepared samples).

	d (nm)	PDI	ζ (mV)	EE (%)
FL(DiO)	107 \pm 37	0.33 \pm 0.11	56 \pm 1	
FL-RSV(DiO)	367 \pm 86 (*)	0.40 \pm 0.06	42 \pm 13	74 \pm 22
FL(DiI)	114 \pm 45	0.22 \pm 0.02	53 \pm 3	-
FL-RSV(DiI)	180 \pm 39	0.32 \pm 0.09	55 \pm 7	-
FL(DiR)	109 \pm 44	0.32 \pm 0.08	63 \pm 9	-
FL-RSV(DiR)	227 \pm 61	0.42 \pm 0.13	52 \pm 3	-
FL (DiD)	-	-	-	-
FL-RSV (DiD)	-	-	-	89 \pm 4

To demonstrate the reduction of ROS activity in primary HUVECs after delivery of FL-RSV, cells were treated with DiD-labeled FL-RSV and RSV solved in DMSO and further diluted in PBS as comparison. The addition of RSV did not affect the fusion abilities of the liposomal formulation as could be visualized using confocal laser-scanning microscopy (**Figure 5.15A**). Additionally,

treatment with a serial-fold dilution of FL-RSV demonstrated a dose-dependent reduction of ROS activity in primary HUVECs, comparable to treatment with RSV in $\leq 0.2\%$ DMSO (**Figure 5.15B**). To further assess whether FL-RSV could affect a CH-mediated hyperpermeability by decreasing ROS activity, primary HUVECs were treated as described in **4.2.5.2**. CH-mediated hyperpermeability could be reduced by treatment with FL-RSV, as indicated by decreased passage of TR-dextran after treatment (p -value = 0.0313) (**Figure 5.15C**). Furthermore, FL-RSV could also protect primary HUVECs from CH-mediated hyperpermeability, if cells were treated with FL-RSV before CH. Here, passage of FL was reduced accordingly (p -value = 0.0313) (**Figure 5.15C**).

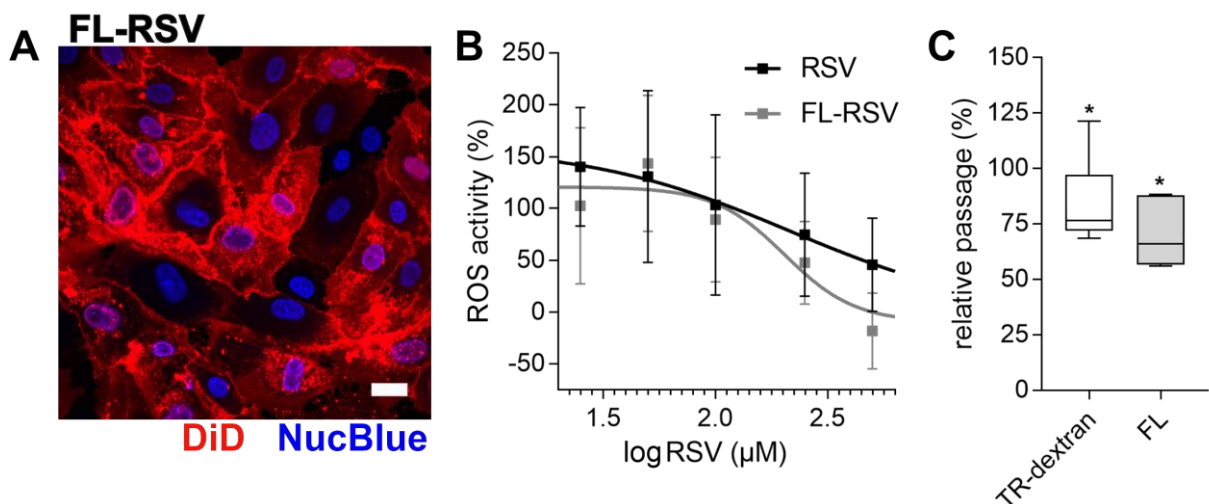


Figure 5.15. Delivery of resveratrol (RSV) to primary human umbilical vein endothelial cells (HUVECs). (A) Fusion of fusogenic liposomes loaded with RSV (FL-RSV) with HUVECs was monitored by homogenous DiD membrane staining. Scale bar 20 μm . (B) Cells were treated with RSV and FL-RSV in a concentration range from 50 μM to 500 μM ; then reactive oxygen species (ROS) formation was triggered with cumene hydroperoxide (CH). Fluorescence intensity was normalized to untreated samples with or without CH addition and displayed as ROS activity (%). Mean with standard deviation is shown ($n \geq 7$ experiments per data point). Results of statistical analysis using Kruskal-Wallis test with posthoc Dunn's test indicated no significant differences. (C) Relative passages across primary HUVECs were analyzed after treatment with CH and subsequently FL-RSV for TR-dextran, and FL-RSV and subsequent CH treatment for FL. To avoid interference of measured fluorescence, FL-RSV and FL were labeled with liposomal tracer dyes DiO and DiD, respectively. Fluorescence intensity was normalized on CH-treated controls. Box plots are shown and the non-parametric Wilcoxon signed rank test was used for statistical analysis (* vs. 100%: $p < 0.05$; $n=5$ experiments and 6 analyzed samples).

In conclusion, permeability of primary HUVECs for FL was increased by enhanced ROS activity as well as ROS-independently by VEGF stimulation. Further, FL were efficiently loaded with

RSV as cargo, without hindering the fusion mechanism. FL-RSV demonstrated to dose-dependently decrease ROS activity and subsequently decreased a ROS-induced macromolecule permeability of primary HUVEC cells.

5.4 Fusogenic liposome-assisted delivery by systemic administration

The formulation of nanoparticles systematically alters the pharmacokinetics of encapsulated drugs. As previously mentioned in **3.1**, delivery by and distribution of liposomes can be drastically modulated by the liposomal composition as a consequence of their physicochemical characteristics. Due to the specific physicochemical requirements for a liposomal composition that is inducing membrane fusion, the biodistribution after administration and the elimination sites of the drug delivery system should be investigated. In previous findings of this work, FL delivery, in contrast to PEG-EL delivery, was strongly influenced by ECM and BM status (see **5.2.2**). Consequently, the interaction with other proteins that can be encountered after systemic administration, such as serum proteins, was also examined. Serum proteins are known to interfere with the availability of drugs to recipient cells, e.g., by protein corona formation and subsequent inaccessibility for target interaction. Thus, consequences for FL applications were investigated. Additionally, a functional assessment of loaded liposomes carrying the antioxidant RSV was done *in vivo*.

5.4.1 Impact of serum proteins on fusogenic delivery

Liposomes entering the bloodstream, e.g., after systemic administration, dynamically interact with serum proteins, and liposomal surface binding of proteins can lead to protein corona formation if thermodynamically favorable. The protein corona is determined by the lipid composition and surface charge of liposomes. It can strongly influence the pharmacokinetics of the drug delivery system, e.g., by altered immune recognition (see **3.1.2**). FL investigated in this work require close contact to the target cell to mediate membrane fusion, possibly hindered by a protein corona shell *in vivo*. To examine whether membrane fusion by FL and endothelial cells is affected by serum components, primary HUVECs were treated with FL with or without 5 % fetal bovine serum (FBS), and fusion efficiency was determined by confocal laser-scanning microscopy and a subsequent image analysis. Fusion was visualized by homogenous membrane staining of cells with DiD for each parameter, and cells were identified by NucBlue nucleus staining (**Figure 5.16A**).

Quantification of fusion efficiency demonstrated that kinetics of membrane fusion were affected by the addition of FBS. After a 15 min-treatment period with FL, fusion efficiency was reduced if FBS was present in the treatment solution. Yet, after 1 h of treatment with FL in addition of 5 % FBS, 72 % of primary HUVECs were fused, in contrast to 27 % fusion after 15 min (Figure 5.16B).

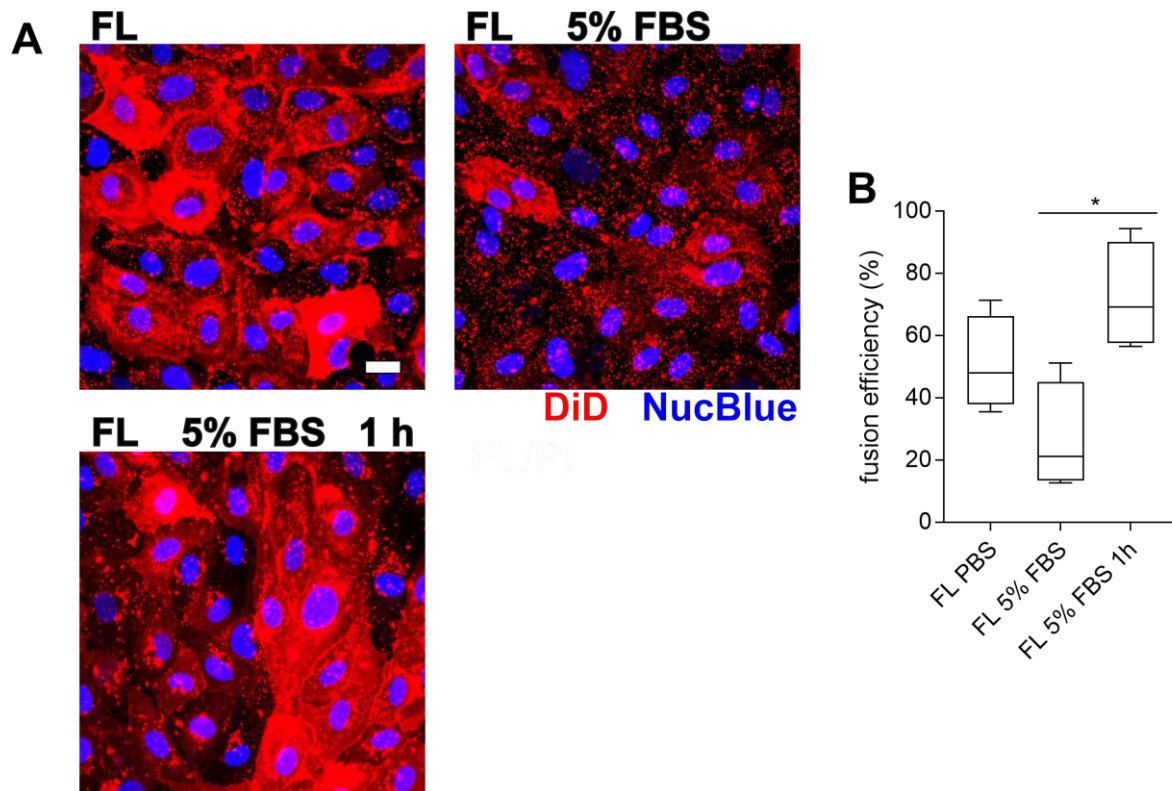


Figure 5.16. Influence of fetal bovine serum (FBS) on the fusion of fusogenic liposomes (FL) with primary human umbilical vein endothelial cells (HUVECs). (A) Fusion efficiency was analyzed after 15 min (or 1 h) of treatment with FL with addition of 5 % FBS using confocal laser-scanning microscopy. FL treatment without FBS for 15 min served as control. Scale bar 20 μ m, applies to all. (B) For quantification, an in-house developed Matlab routine for image analysis was used (see 4.2.4.3). Kruskal-Wallis with posthoc Dunn's test was used for statistical analysis (*: $p = 0.0243$; $n=4$ experiments).

5.4.2 Biodistribution of fusogenic liposomes

To locate FL in tissues relevant for nanoparticle metabolism, FL were repetitively administered to mice by retro-orbital injection, and mice were humanely killed 4 h after the last injection (see 4.2.5.3 and 4.2.6.2). Tissue homogenates of the heart, kidney, lung, and liver were analyzed for fluorescence intensity of the liposomal tracer dye DiD. DiD intensity for FL-treated

mice demonstrated a 2.4-fold change in kidney, followed by a 7.6-fold change for heart tissue homogenate relative to tissues of PBS-treated mice (**Figure 5.17A**). Lung and liver tissue homogenates showed the highest fold changes of fluorescence intensity with 68 and 217, respectively (**Figure 5.17B**), indicating an accumulation of FL or their tracer dye inside the latter mentioned tissues.

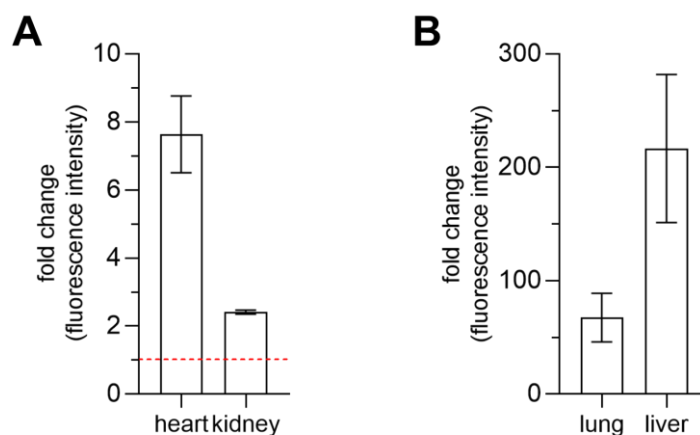


Figure 5.17. Intensity measurement of liposomal tracer dye DiD in murine tissue after repetitive treatment with fusogenic liposomes. A fold change of mean fluorescence intensity with standard deviation is shown for (A) heart and kidney, and (B) lung and liver tissue homogenates compared to PBS-treated controls.

As briefly mentioned in **3.3.2.2**, a dysfunctional endothelium of the cerebral vasculature can be highly relevant for cognitive decline due to an uncoupling of vascular tone and neuronal activity. Therefore, the cerebral vasculature is a promising drug target for treatment of neurodegenerative diseases and age-related pathologies, and, as a consequence, the delivery of drugs aimed to the cerebral endothelium is a promising application field for FL. To visualize FL in the cerebral vasculature, mice with chronic cranial windows were retro-orbitally injected with FL-RSV and with fluorophore-labeled dextran. As further mentioned in **3.3.2.2**, RSV is a potent antioxidant, exerting several anti-inflammatory, anti-thrombic and vasodilatory effects on the vasculature. Yet, it has poor bioavailability and is an attractive target for reformulation, thus its delivery using FL was investigated. The cerebral vasculature was imaged live 30 min after systemic administration of FL-RSV and FITC-dextran using two-photon microscopy. In the cerebral vasculature, a dynamic DiD signal was observable inside the vessel lumen, as visualized by co-localization with FITC-dextran (**Figure 5.18A**, white arrow).

Results

The circulation of DiO-labeled FL-RSV was further observed after a single retro-orbital injection using intravital imaging (**Figure 5.18B**). Dynamic FL-RSV signals were counted 1 h after injection and then every 24 h for six days, indicating the elimination of FL-RSV from the cerebral circulation after 24 h (1 h vs. 24 h: p-value = 0.0020). For the determination of further functional effects of FL-RSV on the cerebral vasculature, FL-RSV were hence administered in periods of 24 h for four consecutive days.

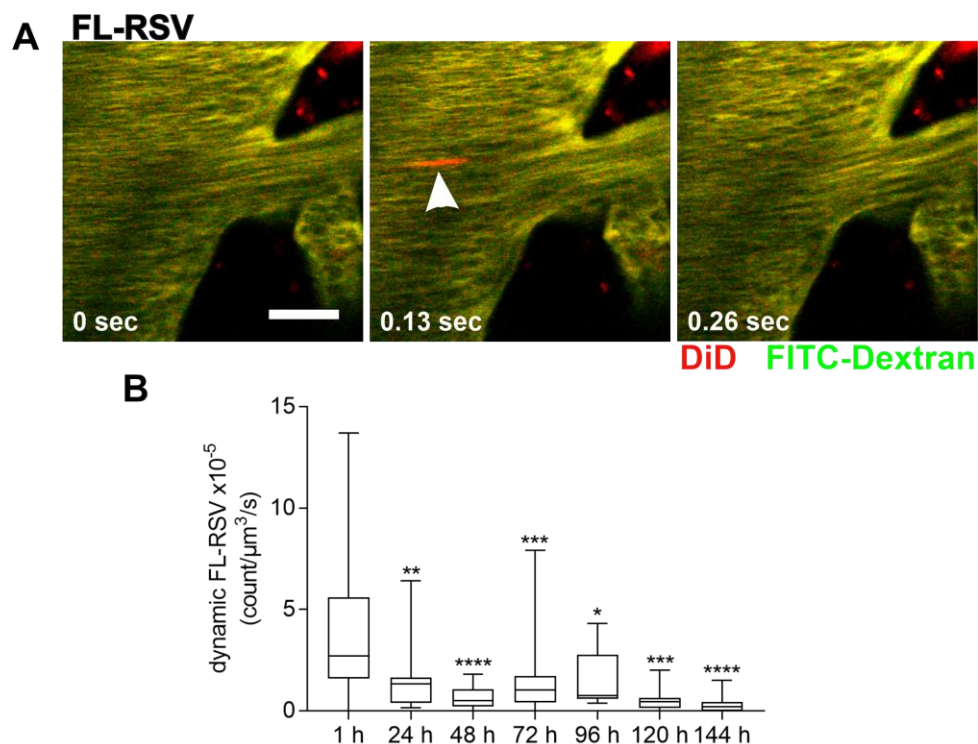


Figure 5.18. Localization of liposomal tracer dyes in the murine brain. Intravital imaging by two-photon microscopy was used to localize fusogenic liposomes loaded with resveratrol (FL-RSV) inside cerebral vasculature after a single injection; FITC-dextran was administered simultaneously to visualize vessel lumen. (A) A time series of images was done to visualize dynamics of DiD-labeled FL-RSV inside vessel lumen. Scale bar 20 μm . (B) The dynamic signal of circulating, DiO-labeled FL-RSV vesicles was counted manually 1 h after administration and then in 24 h periods for 6 days, and is expressed as count/ $\mu\text{m}^3/\text{s}$. Box plots are shown and data were analyzed using one-way ANOVA with posthoc Tukey's test (all vs. 1 h; ****: p < 0.0001; ***: p < 0.001; **: p < 0.01; *: p < 0.05; n=2 animals and ≥ 9 analyzed region of interests per time point). Data were partially published in (42).

In addition to the fluctuating signal of DiD co-localizing with the perfused vasculature, a static signal of the liposomal tracer dye was visualized along the vasculature and in unstained cerebral tissue (**Figure 5.19A**). To further confirm the accumulation of the liposomal tracer dye inside the brain, mice were retro-orbitally injected with FL and FL-RSV for four consecutive

days, sacrificed 4 h after the last injection and DiD fluorescence intensity of brain tissue homogenate was analyzed. Here, DiD fluorescence intensity demonstrated a 1.5- and 2.2-fold change of FL and FL-RSV treated animals compared to PBS-treated animals, respectively (p -values = 0.0313) (**Figure 5.19B**). Murine vasculature was perfused with PBS previous to dissection to eliminate the interference of liposomes circulating in the blood.

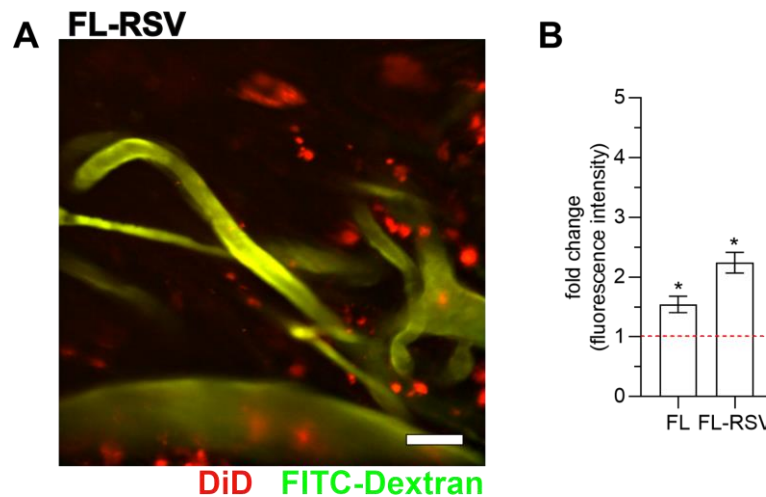


Figure 5.19. Localization of liposomal tracer dye DiD in the murine brain. (A) An overview of several vessels after administration of FITC-Dextran and DiD-labeled fusogenic liposomes loaded with resveratrol (FL-RSV) is shown. Scale bar 20 μ m. (B) Intensity measurement of DiD in the brain after repetitive treatment with FL and FL-RSV. Fold change of mean fluorescence intensity with standard deviation is shown and the non-parametric Wilcoxon signed rank test was used for statistical analysis (* vs. 1: $p < 0.05$; $n=2$ animals per parameter in triplicates each). Data were partially published in (42).

5.4.3 Functional assessment of resveratrol in fusogenic liposomes *in vivo*

To further investigate a functional improvement of neurovascular coupling after antioxidant treatment, cerebral blood flow (CBF) responses after somatosensory stimulation were determined. Whisker stimulation is inducing increased neuronal activity in the somatosensorous cortex and subsequently leads to adaptation of CBF due to functional coupling of the neurovascular unit, comprised of cerebral endothelial cells and cells of the brain parenchyma. With laser speckle contrast imaging, the movement of red blood cells in the superficial cerebral vasculature was spatially and temporally resolved, and a change in red blood cell movement was further correlated with a change of CBF and subsequently the functional neurovascular coupling after somatosensory stimulation.

Results

Laser speckle contrast imaging of the thinned down skull in aged mice was done after four-day treatment with FL and FL-RSV. Data indicated that CBF adaptation to somatosensory stimulation was decreased in aged mice compared to young animals (young vs. aged: p-value < 0.0001). Treatment with FL-RSV, however, rescued the adaptation of the vascular tone to neuronal activity, as can be visualized by an increase in CBF response (aged vs. aged+FL-RSV: p-value < 0.0001) (**Figure 5.20B**). RSV exerts its antioxidant effects in endothelial cells by induction of endothelial nitric oxide synthase (eNOS) (154). Accordingly, the impact of FL-RSV treatment was reversed by treatment with the NO synthase inhibitor N ω - Nitro-L-arginine methyl ester (L-NAME) (young vs. (aged+FL-RSV)+L-NAME: p-value < 0.0001). A similar decrease of CBF change was observed in young animals (young vs. young+L-NAME: p-value < 0.0001), indicating a NO-mediated adaptability of the cerebrovascular system in young and FL-RSV treated animals. L-NAME did not show any impact on CBF response in aged mice after FL without RSV treatment or in the aged control group (**Figure 5.20B**).

To sum up the investigation of systemically applied FL, their systemic administration resulted in a hepatic and pulmonary accumulation, and an interaction of FL with serum content retarded fusion with endothelial cells *in vitro*. However, FL could additionally be localized in cerebral vessel lumen and enclosed brain parenchyma after systemic administration. Loading FL with RSV and repetitive systemic administration further functionally improved CBF response to neuronal stimulation in an endothelium-specific manner.

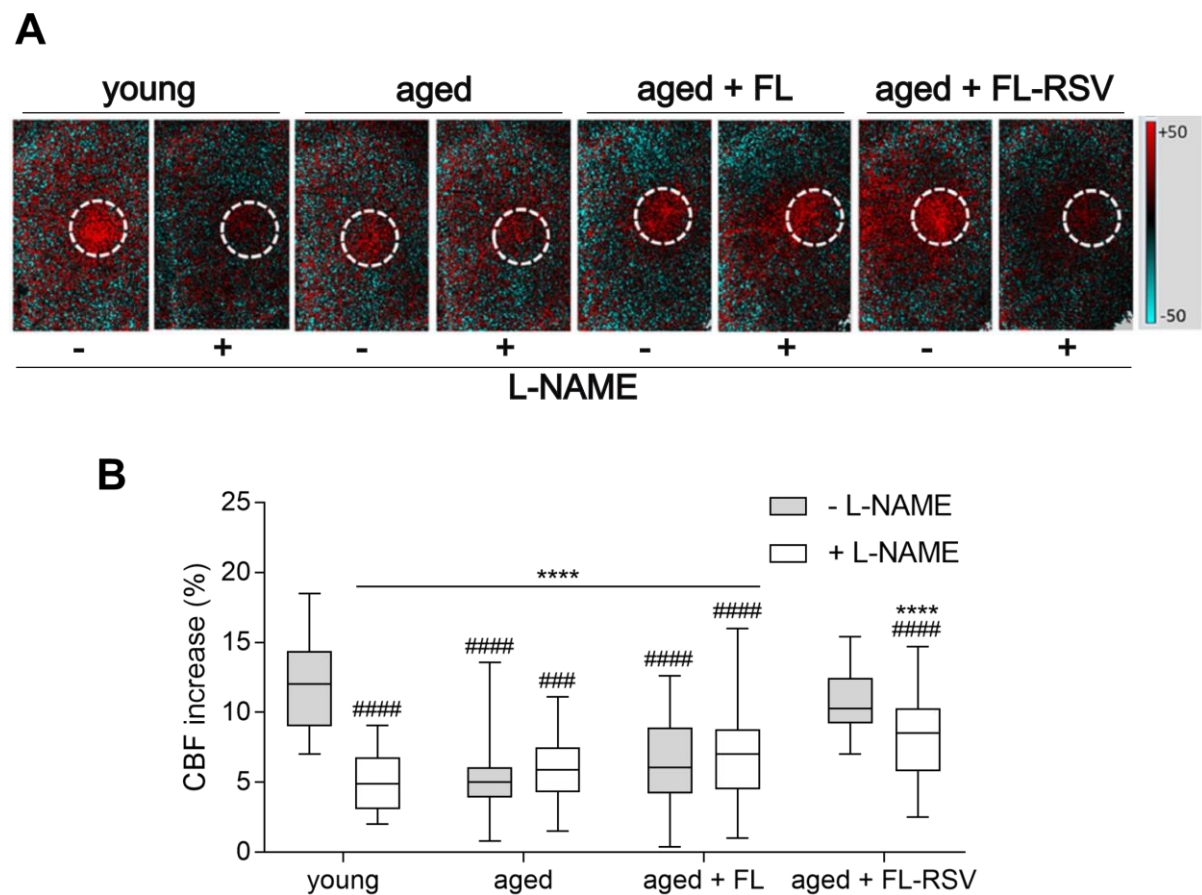


Figure 5.20. Cerebral blood flow (CBF) response of mice after somatosensory stimulation. CBF increase was investigated in young and aged mice, aged mice were repetitively treated with fusogenic liposomes (FL) and FL loaded with resveratrol (FL-RSV) for four consecutive days before the experiment. Mice were systemically injected with the endothelial nitric oxide synthase inhibitor L-NAME prior to the experiment as control. (A) Differential perfusion maps with analyzed regions of interests (dashed lines) after somatosensory whisker stimulation are shown for all parameters, with +50 representing highest relative CBF change compared to the baseline (before whisker stimulation). (B) Data were normalized on the baseline CBF of the region of interest before somatosensory stimulation. Box plots are shown and data were analyzed using one-way ANOVA with posthoc Tukey's test (**** vs. young – L-NAME: $p < 0.0001$; ### vs. aged + FL-RSV – L-NAME: $p < 0.001$; ##### vs. aged + FL-RSV – L-NAME: $p < 0.0001$; $n=4-7$ animals and ≥ 24 measurements per parameter). Data were published in (42).

6 Discussion

The application of delivery vehicles in drug development has enabled new possibilities to tailor pharmacokinetics improving therapeutic efficacy while reducing immunogenicity and other adverse effects. Pioneering approvals used the liposomal stealth technology for drug entrapment, especially in cancer therapy. While optimized therapeutic performance, including a preferable toxicity profiling, has been achieved, other problems emerged. Anaphylaxis observed for the pegylated stealth liposomes and only a marginal accumulation at the target site promote a focus of pharmaceutical research on innovative technologies for drug delivery.

So far, liposomal formulations for drug delivery primarily focused on reduced systemic toxicity rather than increasing efficacy by cellular uptake. FL are liposomal carrier systems enabling the cellular uptake of their cargo by membrane fusion. Thereby, FL can increase cytoplasmic cargo localization and bypass the endosomal pathway. The altered cellular uptake mechanism by membrane fusion suggests a superior drug accumulation at the target site and consequently an increase of efficacy compared to endocytosed liposomes. Thus, an investigation of biodistribution and the interaction with physiologically interfering processes, such as protein absorption, systemic circulation, extravasation, and passage through the ECM, was presented in this work.

6.1 Considerations for fusogenic liposomal cargo selection

As introduced in **3.1.2.1**, the stalk mechanism describes lipid bilayer fusion. Here, the merging of outer bilayer leaflets is accompanied by non-bilayer intermediate phase transition, and followed by the creation of a fusion stalk and subsequent fusion pore opening. A similar phenomenon can be observed for the fusion of FL with mammalian cell membranes. Fusion events of FL and mammalian cells presented in this thesis are solely induced by the specific FL composition and independent of external inducers or catalysts. Nevertheless, incorporating additional molecules can be beneficial for their delivery to the cell if an alternative cellular uptake pathway such as endocytosis is inefficient or disadvantageous for the cargo.

6.1.1 Circumvention of lysosomal cargo sequestration

The present work examined the relevance of direct cargo release for drug effects. This was done by entrapment of cargos with similar scaffold but different hydrophobicity and basicity in FL and PEG-EL. ACL and DOX belong to the class of anthracyclines, which are commonly used anti-cancer therapeutics. ACL is more hydrophobic than DOX due to an addition of a more complex aglycolic moiety to the anthracycline scaffold (see **Table 4.1**). The difference in hydrophobicity is also visible for the partition coefficients between octanol and PBS for ACL and DOX of 21.8 and 0.5, respectively (183). Subsequently, formulation of the more hydrophobic ACL resulted in a bilayer localization in FL, demonstrated by Foerster resonance energy transfer of ACL to the membrane-inserted dye DiR, which could not be demonstrated for DOX (7, 8).

Anti-proliferative effects of ACL and DOX were investigated in MCF 10A cells using FL and PEG-EL formulations to examine the impact of differential cell uptake on drug efficacy (see **5.1.2**). Entrapment in FL significantly increased the performance of DOX compared to DOX in PEG-EL, while a similar formulation-dependent effect was not observable for ACL (**Figure 5.3**). A formulation-dependent difference in DOX effects can be attributed to the difference in cell uptake. PEG-EL are taken up by endocytosis, followed by endosomal trafficking and a possible lysosomal degradation of drug cargo. During trafficking, the endosomal and lysosomal lumen are acidified. Thus, a pH optimum for activity of several hydrolases and other enzymes is generated for the degradation of endocytosed compounds (184). In contrast to this, FL can fuse with the cell membrane. Subsequently, FL enable an immediate drug release into the cytosol, circumventing the endo-/lysosomal pathway. An increased cell uptake of cargo mediated by FL was demonstrated before (44, 48). Although the difference in hydrophobicity impacted the incorporation of anthracyclines in FL as mentioned before, the difference in basicity can lead to preferred endosomal degradation. Due to its lower pKa value of 7.3 (183), ACL is less likely to accumulate in the lysosomal lumen for degradation after endocytic uptake, because it can diffuse through the endosomal membrane. DOX with a higher pKa value of 9.93 (185) displays stronger lysosomotropic preferences and is hence much more likely to accumulate in endosomes. This can lead to further lysosomal degradation as a consequence. Thus, the increased basicity of DOX attributes to higher sensitivity to lysosomal degradation. The direct release of DOX into the cytosol, as mediated by FL, can subsequently increase intracellular availability and anti-proliferative effects in comparison to endocytosis.

The majority of drugs with intracellular targets requires high intracellular availability for sufficient effects. However, lysosomotropic preferences have also been exploited before, e.g., for the use of anti-viral agents that accumulate in lysosomes (186). Therefore, the choice of a delivery vehicle should aim at preferential pharmacokinetic profiling, and also at beneficial cellular uptake route depending on the drug's chemical characteristics and intended use. For cargo with lysosomotropic preferences and intracellular targets, the present work confirmed the superiority of FL-mediated cellular delivery compared to endocytosed liposomes.

It is further to note that ACL and DOX compartmentalized differently after cellular uptake, yet unaffected by the used formulation (see **5.1.2**) (49). A key pharmacological feature of many anthracyclines is their proliferation reduction by interference with DNA due to the planar anthraquinone scaffold. Furthermore, inhibition of the DNA-Topoisomerase II complex during DNA replication and histone eviction is observed, in addition to cellular metabolism that is generating free radicals (187-189). Mediation of these effects has to occur in different cell compartments, e.g., in the nucleus or mitochondria. While the localization of DOX in nuclei was observed, ACL was found in nucleus-enclosed substructures (**Figure 5.2**). Still, a localization-dependent claim of different effects for both anthracyclines would require a further specification of ACL compartmentalization. However, sensitivities of DOX-resistant tumors and cell lines to ACL have been observed before (190) and support the theory of different mechanisms of action.

6.1.2 Transient permeability induction by membrane fusion

Previous theoretical and experimental studies indicated that a protein-dependent fusion, e.g., mediated by the fusogenic influenza protein hemagglutinin, is accompanied by a membrane permeability during early fusion pore formation (191). A transient permeability of the cell membrane during protein-independent membrane fusion would have further consequences for biological or pharmaceutical applications by potential cellular delivery of compounds in proximity to the merging membranes that are not part of the liposomal formulation.

In the present work, membrane-impermeable PI delivery to the mammalian cell line MCF 10A was investigated to study the possibility of a passive cellular uptake induced by FL membrane fusion (see **5.1.1**). Treatment of cells with FL loaded with PI (FL-PI) resulted in intracellular localization of the dye, observable by confocal laser-scanning microscopy (**Figure 5.1**). PI was

demonstrated before to intercalate in DNA strands, leading to a spectral redshift of fluorescence excitation and emission (192, 193). In the present work, the dye was located throughout the cell cytoplasm and not strictly intercalated into nuclear DNA, observable by overall intracellular staining in contrast to nucleus accumulation. Pores of the nuclear envelope are approximately 9 nm in size and should enable nucleus translocation of PI with a hydrodynamic radius of <1 nm (194, 195). The possibility of nucleus accumulation by DNA intercalation in MCF 10A cells was also previously demonstrated for DOX (**Figure 5.2**). However, PI was also previously shown to bind to double-stranded RNA in the cell cytoplasm: In literature, this is leading to increased false-positive rates in flow cytometry-based cell cycle analysis without RNase treatment (193, 196). Micro(mi)-RNA matures from double-stranded RNA and is commonly found in mammalian cells. It is involved in the regulation of cellular mRNA levels. Recently, miRNA-181a expression was found in MCF 10A cells, presumably suppressing tumorigenesis-related pathways (197, 198). Thus, the additional cytoplasmic signal observed in **5.1.1** might be related to miRNA expression, such as miRNA-181a.

Additionally, cells were treated with FL not loaded with PI, though PI was added at a similar concentration after liposome generation and before cellular treatment (FL/PI). Here, PI was not loaded into the aqueous liposomal core during lipid film hydration. The membrane impermeability of the dye should omit significant intercalation into the liposomal membrane or lumen post-preparation. However, the lipid phase present in fusogenic liposomes is still unclear. While a lamellar phase provides distinct extra- and intravesicular space, other lipid phases, e.g. inverted hexagonal or cubic phases, could give rise to a less distinct separation of liposomal lumen and aqueous milieu (199, 200).

Nevertheless, a noticeable PI uptake was observed with confocal laser-scanning microscopy (**Figure 5.1**). These results demonstrated uptake of membrane-impermeable dye mediated by FL. Although FL have been used before to deliver otherwise membrane-impermeable substances, the latter have always been actively incorporated into the liposomal formulation. In the present work, delivery of a membrane-impermeable dye is shown due to the FL-mediated fusion process, but not due to deliberate incorporation into FL. Hence, the fusion process might enable an additional passive delivery of compounds by a transient increase of membrane permeability, e.g., by pore formation (53).

Membranes of cells and vesicles are usually exposed to hydrostatic and osmotic pressure, which contribute to the lateral tension of membranes. Pore formation of these membranes can be explained by the hydrophobic effect and a change in enthalpy. At pore opening, surface energy reduction occurs due to the decreasing lateral tension of the lipid membrane. This is opposed by an increase in energy needed for the curving of lipids at the pore edge to avoid the exposure of hydrophobic tails to water. After expanding the pore to a critical size, pore formation becomes energetically favorable, since the reduction of lateral tension outgrows pore edge tension (201). The formation of pores in lipid membranes is usually triggered by physical cues, such as mechanical stress, or chemical cues, such as detergents and proteins (202-204). Previous theoretical and experimental studies also indicated that the fusion process of bilayers can relax membrane tension (205, 206). Thus, a fusion-induced decrease of membrane tension by transient pore opening might explain the uptake of membrane-impermeable PI. Yet, a mechanistic understanding of the transient permeability increase requires an understanding of the FL-induced fusion mechanism. The latter is still a subject of current research and was not further investigated in this work.

A passive entry pathway can be additionally important while discussing FL suitability as drug delivery vehicles. In literature, drug delivery directed by transient permeability increase of targeted cells is currently studied utilizing sonoporation. Microbubble-mediated sonoporation can enhance cellular uptake of therapeutic agents using a transient cell membrane perforation by ultrasound (207). Drug delivery using sonoporation most likely mediates an enhanced drug influx as well (208). By actively and passively mediating cellular cargo uptake by membrane fusion, FL can be used to deliver otherwise cell-impermeable cargo and might also enable drug uptake of co-formulated therapeutic agents for combinatory treatment. However, entrapment of cargo is still the method of choice for clinical applications since it can guarantee synchronized pharmacokinetics of FL and entrapped drug.

6.2 Interactions of fusogenic liposomes with extra-cellular matrix

While the consequences of membrane fusion for selected liposomal cargo have been briefly discussed in 6.1.1, the target site availability of FL and their cargo vastly depends on interactions of the nano-carrier with the ECM prior to cellular delivery. Breast cancer progression is known to involve a remodeling of the ECM by cancer and cancer-associated cells, including BM lesions, as well as ECM stiffening, chemical modification, and degradation (67-72). The penetration depth of nanoparticles through the ECM is an important parameter for effective drug delivery in tumor treatment, modulating the range width of the anti-cancer drug to as many cells as possible. The tumor availability is influenced by the nanoparticle's ability to diffuse through the ECM, which was shown to be influenced by interstitial fluid pressure, binding sites in the ECM, and the ECM meshwork size (209).

6.2.1 Cargo uptake modified by liposome and extracellular matrix interplay

The movement of particles through the ECM is largely affected by steric interactions, e.g., due to collisions with ECM fibers. Consequently, particles smaller than the mesh size should pass without hindrance, while larger particles should not. Supporting this theory, a previous study demonstrated the penetration of nanoparticles of 1 – 100 nm in size through cell spheroid-derived ECM depended on nanoparticle size, as well as the density of ECM (210). Following this, permeation of nanoparticles FL through the ECM meshwork, as mimicked by Geltrex and collagen I, was presumably hampered due to the FL diameter (see 5.2.1). Yet, an accumulation of FL at the gel and aqueous interface was also observed, indicating an interaction of liposomes with the ECM-like gels, probably by interactions of the liposomal positively charged lipid derivative DOTAP with negatively charged moieties of the gels (**Figure 5.4**). Geltrex contains heparan sulfates proteoglycans, which commonly dictate the negative charge of ECM. Collagen I has a net neutral charge at physiological pH (211). However, it is amphoteric and can thus provide interaction sites of opposite charge to FL. An insufficient permeation was further reported by the negligible delivery of liposomal tracer dye to highly invasive breast cancer cells in a spheroid model, which was additionally shown to secrete ECM-associated collagen IV (see 5.2.1: **Figure 5.6** and **Figure 5.7**). FL also stuck to the self-secreted BM of the MCF 10A acini model (see 5.2.2: **Figure 5.8**). However, the electrostatic interaction of FL with

the BM of the MCF 10A acini model was additionally accompanied by a BM maturation-dependent restrictiveness of liposomal dye delivery by FL when compared to PEG-EL (**Figure 5.9**).

Size-dependent sieving of particles traversing the ECM was previously demonstrated to be accompanied by electrostatic and hydrodynamic interactions (82, 212), presenting the highly complex interplay of nanoparticles and ECM. In a previous publication, the maturation of the BM in the MCF 10A acini model induced an increase in size-dependent retardation of macromolecule passage, presumably due to further development of the BM meshwork and subsequent decrease of pore size (165). Thus, the results of the present work suggest a size-restriction of FL passage through the ECM, in addition of charge-driven interactions of FL with negatively charged moieties.

In contrast to FL, no accumulation of PEG-EL with a negative zeta potential was observed at the BM of the MCF 10A acini model (see **5.2.2: Figure 5.8**), confirming the relevance of electrostatic attraction for the sticking of FL to ECM. Although PEG-EL did not accumulate on the BM, a change in liposomal tracer dye delivery was not observed for PEG-EL in any observed parameter (see **5.2.2: Figure 5.9**), presumably due to low cell interaction and uptake of PEG-EL irrespectively of cell accessibility.

A recent study supported the high relevance of efficient cellular uptake in comparison to enhanced ECM diffusion, demonstrating that positively charged and pegylated liposomes outperformed their negatively or neutrally charged counterparts when comparing anti-cancer drug efficacies in several breast cancer models *in vivo*. Still, overall circulation time and tumor accumulation were reduced for positively charged liposomes (213). Thus, the relevance of low nanoparticle interaction and adhesion for improvement of drug efficacy by prolonged circulation times should be critically weighed against an enhanced drug uptake by targeted cells. Yet, it is also to consider that the interaction of pegylated liposomes with ECM-like matrices were previously shown to be affected by the conformation of PEG in a mushroom or brush regime (214). Hence, diffusion of PEG-EL could be increased by a higher liposomal surface density of PEG, as long as the bilayer stability is not compromised. However, whether increased diffusion could balance out the reduced cellular uptake for improved drug efficacy, is to be investigated.

6.2.2 Consequences for drug delivery

Enhanced cellular uptake of liposomal tracer dye delivered by FL compared to PEG-EL was demonstrated after BM lesion induction by EGF stimulation in the MCF 10A model, mimicking pathophysiological onset of carcinogenic invasion (see **5.2.2: Figure 5.9**). Further, the performance of the anti-cancer drug DOX, entrapped in FL and PEG-EL, was evaluated by estimation of the anti-proliferative effect in MCF 10A acini with a low or highly matured BM (see **5.2.3**). Anti-proliferative effects of DOX entrapped in FL could be increased in low MCF 10A acini in contrast to DOX entrapped in PEG-EL, while this effect was not observable in MCF 10A acini with a highly mature BM (**Figure 5.11** and **Figure 5.12**). Accordingly, the therapeutic performance of DOX was dependent on the BM maturation state, presumably due to increasing size-restrictiveness. These results support the high relevance of FL-mediated, increased cellular uptake of drug cargo for drug efficacy and suggests a potential use of FL as drug delivery vehicles at infiltration sites of solid tumors.

However, the observed low diffusivity of FL presumably caused by electrostatic interactions is problematic for the delivery of anti-cancer therapeutics. Therefore, the use of FL as drug delivery vehicles can be further improved by the addition of ECM-degrading compounds, enabling enhanced intratumoral diffusion without altering the liposomal composition that is optimized for highly effective membrane fusion. Currently investigated delivery strategies involve the degradation of stromal collagen, e.g., by administering collagenase in different formulations (215, 216). Delivery of liposomal tracer dye mediated by FL was feasible after MCF 10A treatment with collagenase IV as well (see **5.2.2: Figure 5.10**). Thus, it is highly likely that the combination with an ECM-degrading compound could also increase FL cargo delivery into ECM-remodeled tumors.

The FL membrane can merge with the cell membrane by electrostatic interaction on approaching to short distances, and subsequent membrane fusion. This requires close interactions of both lipid membranes, enabled by the strongly opposed charges of the cell membrane and FL. Nevertheless, highly charged nanoparticles were also effectively trapped in ECM-like hydrogels in previous research (82). Thus, the optimization of FL-mediated drug delivery has to address the dilemma of choosing the right liposomal composition. FL needed for highly efficient cellular uptake mediated by membrane fusion require a positive charge. In contrast, enhanced passage through the ECM and prolonged circulation time are in need of

inert nanoparticles with low to neutral charge. Consequently, a modified FL composition that is adjustable to the specific milieu in the circulation or tumor might tailor the formulation towards use in drug delivery. It is highly likely that the PEG coating of a liposomal surface hinders membrane fusion due to the thickness of several nanometers on the liposomal surface, and masks the positively charged lipids of FL during circulation. The application of lipids linked to PEG with pH-sensitive bonds has been previously investigated due to the acidic pH in the tumor environment (217), enabling site-specific hydrolysis. Amongst others, research has focused here on the application of hydrazone-based PEG-lipid conjugates (218). The introduction of hydrazone-based PEG-DOPE conjugates might therefore permit preferential diffusion in tumor ECM, followed by fusion-mediated cell uptake after acidic hydrolysis of the PEG-DOPE conjugate.

In addition to the latter strategy, the presence of enzymes overexpressed and secreted to the tumor matrix can be taken advantage of. As briefly described in **3.2.2.1**, increased activity of the endopeptidase MMP-2 by deregulation of the EGFR pathway can lead to ECM remodeling. Its overexpression is frequently observed in various solid tumors and is therefore discussed as a biomarker (219). Substrates with the peptide sequence Pro-Leu-Gly-Arg are subject to proteolysis by MMP-2, and optical probes containing this peptide sequence have been investigated in the search for tumor diagnostics (220-222). Furthermore, chemotherapeutics were previously linked to hydrogel matrices with the specific peptide sequence, enabling a site-specific drug release (223). Consequently, a coating of the FL surface with an MMP-2 substrate using a peptide-functionalized lipid might enable the removal of the peptide coating in tumor environment overexpressing MMP-2. Whether a peptide functionalization of the FL surface can hinder cell uptake before reaching the targeted tissue and fusogenic abilities can be recovered after substrate cleavage, are to be determined.

Overall, FL showed size-restricted delivery of liposomal tracer dye to cells embedded in ECM, yet this was greatly affected by strongly opposed charges of FL and ECM, presumably hindering FL passage through the ECM. However, the enhanced cellular uptake mediated by membrane fusion in contrast to endocytosis enabled an increased delivery of liposomal tracer dye, as well as pharmacologically relevant effects of drug cargo doxorubicin. For drug efficacy, previously mentioned results show the benefit of an increased cellular uptake by FL compared to PEG-EL. However, the accessibility of targeted cells is hindered by low ECM diffusivity of FL. Thus, it requires optimization of the delivery strategy, either by combination with ECM-

degrading compounds or the modification of the liposomal surface. The latter might enable fusogenic abilities of FL to be site-specific due to low pH or enzyme activity in the tumor ECM; however, this has to be investigated further.

6.3 Interactions of fusogenic liposomes with vascular endothelium and their biodistribution

Though the penetration of ECM is an important parameter for drug delivery using nanoparticles, the extravasation of those is the basis for availability at the targeted tissue after systemic administration. Vascular endothelial cells are the barrier-forming cells of the vasculature. Their restrictiveness to macromolecule passage is vastly characterized by intercellular connections, such as adherens and tight junctions (97, 98).

6.3.1 Effects of endothelial barrier integrity

The restrictiveness of intact endothelium and leakiness of compromised endothelium for nanoparticle delivery is commonly utilized by the enhanced permeation and retention effect of stealth liposomes (34). Especially in cancer therapy, the vascular hyperpermeability induces increased extravasation of nanoparticles compared to intact peripheral endothelium, restricting macromolecule passage. In this work, an *in vitro* model of HUVECs restricted the passage of macromolecules (see **5.3.1**). Varying in size from approximately 2.3 nm (FITC-dextran, supplier information) to approximately 100 nm (FL; **Table 5.3**), the percentage of passed macromolecule through the cellular barrier of HUVECs inversely correlated with size (**Figure 5.13**; passage of 16 % in comparison to 2 %, respectively). Thus, the permeation of FL is vastly restricted by an endothelial monolayer with intact intercellular junctions.

Cancer and a vast selection of other diseases with cardiovascular and neurodegenerative implications rely on pathophysiological changes in the vascular endothelium. In cancer, hyperpermeability-induced extravasation can support tumor growth. Cancer-associated endothelial cells further maintain an inflammatory tumor environment and provide the formation of new vasculature by neoangiogenesis. Here, hyperpermeability of the vascular endothelium could lead to increased extravasation of nanoparticles and accumulation in tumor tissue, beneficial for overall treatment efficacy.

In this work, the consequences of a compromised endothelium on FL passage were investigated (see **5.3.2**). A dysfunctional endothelium was mimicked by induction of ROS activity after treatment with CH. Additionally, cancer-associated hyperpermeability was investigated after treatment with VEGF, which was demonstrated before to drive cancer-

associated changes in the vascular endothelium *in vitro* and *in vivo* (224, 225). Increased ROS activity in endothelial cells resulted in discontinuities of the cellular junction-associated protein ZO-1 at the cell membrane, indicating an impaired barrier function of the endothelial cell layer (**Figure 5.14**). This impairment was confirmed by the increased passage of FL and TR-dextran. Treatment of the endothelial cell layer with VEGF resulted in ROS-independent discontinuities of ZO-1 membrane localization as well (**Figure 5.13** and **Figure 5.14**). Changes in intercellular junction formation after VEGF treatment resulted in the increased passage of FL, while an increased passage was not observed for the smaller TR-dextran. ROS formation was used to generate a model system of generic endothelial dysfunction, as observed in the onset of various aforementioned pathophysiologies. Here, ROS formation enabled enhanced translocation of the investigated macromolecules across HUVECs. However, stimulation of endothelial cells by VEGF is complex and can either be a physiological angiogenesis stimulus or be involved in hyperpermeability and tumor angiogenesis.

Furthermore, upon stimulation of endothelial cells with VEGF, clathrin-mediated endocytosis for VEGF receptor trafficking is enhanced (226). Clathrin-mediated endocytosis additionally is a critical cellular uptake route of small dextrans as well (227). Therefore, an increased, unspecific cellular uptake of TR-dextran by increased VEGFR trafficking cannot be excluded. Subsequently, the lack of increased TR-dextran passage after VEGF treatment of HUVECs as observed in **5.3.2** might not be caused by a lack of permeability induction but by the interference of TR-dextran uptake by HUVECs. Thus, the paracellular permeability might not be measurable by TR-dextran passage after VEGF treatment due to interference with cellular uptake and a possible transcellular passage. For FL, interference with cellular uptake was neglected since fusion efficiencies were not significantly altered after VEGF treatment of HUVECs (**Figure 5.14**). Accordingly, induction of increased permeability by ROS or VEGF treatment led to the increased passage of FL. In addition to previous findings of interactions of FL with ECM proteins, an enhanced permeability and retention effect is thus predicted for FL, as discussed for stealth liposomes *in vivo*.

6.3.2 Biodistribution of fusogenic liposomes

Biodistribution of FL after systemic administration might favor the accumulation of the drug delivery system in tissues associated with highly permeable vasculature, as has been

suggested before. This theory is further supported by the accumulation of FL in liver tissue after systemic administration by repetitive retro-orbital injection to a murine model (see **5.4.2: Figure 5.17**). The hepatic vascular endothelium is known to be fenestrated and devoid of BM (228), of whom the latter was previously highlighted as a barrier for FL passage. Further, the accumulation of FL in hepatic tissue is in accordance with previous studies of liposomal biodistribution (229, 230), indicating a resulting hepatic clearance as proposed for nanoparticles of comparable size (231). A preferred hepatic elimination should also be considered for an upcoming modification of FL administration since oral drug administration can result in enterohepatic circulation, which describes the circulation of substances taken up in the duodenum followed by transport to the liver and bile (232). This could lead to increased hepatic clearance of orally applied FL before entering the systemic circulation.

Furthermore, systemic administration of FL resulted in lung accumulation (**Figure 5.17**). Several studies suggest a preferential gene expression in the lung after intravenous injection of cationic lipoplexes delivering nucleic acids (233, 234), proposedly due to an aggregation of lipoplexes with red blood cells and size-dependent accumulation in pulmonary microcirculation (235). Yet, FL have been demonstrated to display only sparse interactions with red blood cells *in vitro* (44). Hence, an aggregation-induced pulmonary accumulation seems rather unlikely. An essential function of microcirculation is the adequate delivery of oxygen to tissue. Accordingly, the microcirculation is also executing the key pulmonary function of gas exchange at the blood-gas barrier. Microcirculation consists to a great extent of capillaries, whose vessel diameter is commonly less than 10 μm (236). The surface-to-volume ratio in vessels increases with smaller diameter. Thus, interaction of FL and endothelial cells is more likely in vessels with smaller diameter. Additionally, the blood flow velocity is inversely correlating with the cross-sectional vessel area, so an accumulation in lung tissue with a high percentage of microcirculation and low blood flow velocities might be further related to the increased interaction time of FL with cells of the pulmonary vasculature. Membrane fusion is a rather rapid process in the magnitude of microseconds (237). However, the interaction of FL with serum components demonstrated a delay in high fusion efficiencies with endothelial cells (see **5.4.1.: Figure 5.16**). This delay was presumably induced by the formation of a protein corona comprised of serum proteins and FL. Thus, the results of the present work argue for a need for prolonged interaction time of FL and endothelial cells in systemic circulation due to a possible protein corona formation. Accordingly, an increased

surface-to-volume ratio and lower blood flow velocities in the microcirculation could enable an increased interaction of FL with endothelial cells, followed by increased delivery of liposomal tracer dye. To further support or oppose this theory, endothelial cells could be cultured in microfluidic devices with tunable flow rates, mimicking altering blood flow velocities due to vessel diameter.

6.3.3 Vascular endothelium as a therapeutic target

Endothelial cells are critical regulators of vascular homeostasis, and reduced availability of NO results in endothelial dysfunction and subsequent inflammation, prothrombic activity, and hypertension with related pathophysiologies. During aging, NO availability is reduced as well, and reduced functional adaptability of endothelial cells in the neurovascular unit might be involved in age-related cognitive decline (154). Hence, a passive targeting of endothelial cells of the neurovascular unit by FL loaded with drugs ameliorating a rebalanced vascular homeostasis might rescue vascular responses to neuronal activity in the aged cerebral vasculature, providing a therapeutic benefit for aging-related pathologies. As visualized by intravital microscopy in mice, FL have been taken up by cells of the cerebral vasculature (see **5.4.2: Figure 5.18**). Though the identity of cells with liposomal tracer dye localization could not be specified, an endothelium-specific effect of liposome cargo could be measured *in vivo* (see **5.4.3**). Both observations point towards an uptake by cerebrovascular endothelial cells.

RSV is a plant-derived polyphenol that was shown to improve mitochondrial function by attenuating mitochondrial oxidative stress. It was further shown to increase Nrf2 activation, a transcription factor regulating antioxidant enzyme expression, and sirtuin-1 activation, which is implicated in the regulation of mitochondrial function and the DNA damage repair machinery (127, 148). A previous study of RSV administration in an aged mouse model indicated vasoprotective effects of RSV by increasing neurovascular adaptability to neuronal stimulation (154). However, poor pharmacokinetics of RSV by low aqueous solubility, bioavailability and a rapid clearance suggest the need for an optimized formulation of RSV. In a previous study, FL loaded with RSV (FL-RSV) significantly increased RSV uptake to aged endothelial cells *in vitro* while attenuating ROS activity and increasing Nrf2 activation (46). In this work, repetitive, systemic administration of FL-RSV to aged mice significantly enhanced neurovascular adaptability to somatosensory stimulation (see **5.4.3: Figure 5.20**). This effect

was reversible by inhibition of the nitric oxide synthase. Hence, uptake of FL-RSV by endothelial cells of the cerebral vasculature is highly probable and further supported by the previously mentioned FL dye localization in cells nearby vessel lumen. These findings again confirm the suitability of fusogenic liposomes as drug delivery vehicles, here with special focus on delivery to the cerebral vasculature.

In literature, increased permeability of the blood-brain barrier was also demonstrated at the hippocampus, a critical part of the cortex for learning and memory, potentially contributing to age-related cognitive impairment (238). An increase in vascular permeability is further observed in various central and peripheral pathologies. Furthermore, the breakdown of the vascular barrier function is critical in the supply of solid tumors and promotes metastasis as previously mentioned. In this work, the investigation of macromolecule passage through endothelial monolayer demonstrated that the barrier function of HUVECs could be improved by FL-RSV treatment (see **5.3.3: Figure 5.15**). The beneficial effects of FL-RSV are presumably mediated by decreasing ROS activity after radical stimuli, as could be further confirmed for HUVECs (**Figure 5.15**). Hence, the rescue of neurovascular coupling responses by RSV might be supplemented by a recovered barrier function of the neurovascular endothelium. Recovery of the barrier function could further decrease the passage of neurotoxic proteins, pathogens, and immune cells with immense pathological relevance (238).

7 Conclusion and outlook

The most striking difference between FL and conventionally used liposomes in drug delivery is the passage of the cell membrane and cargo delivery by membrane fusion or endocytosis, respectively. In this work, a passive entry of cargo mediated by FL-induced membrane fusion highlighted the possibility of transient permeability increase of the cell membrane, in addition to the delivery of compounds entrapped in FL (see 5.1.1). Although the fusion mechanism of FL is so far not completely understood, an increase in membrane permeability might be explained by a transient pore opening, enabling a passive compound uptake from the extracellular space.

Furthermore, the change in cellular trafficking after uptake mediated by membrane fusion or endocytosis can be highly important. Compounds with higher basicity and lysosomotropic preferences have been shown to benefit from a direct release into the cytosol after cellular uptake compared to endocytosis (see 5.1.2). An immediate cytosol release can prevent lysosomal accumulation and degradation as demonstrated for the anti-cancer therapeutic DOX, underlining a potential use of FL as delivery vehicles for weakly basic drugs in cancer therapy. This was further supported by the adjustability of FL-mediated delivery depending on the status of the BM (see 5.2.2). BM lesions are critical for cancer progression; hence an increased uptake of FL-delivered cargo, such as anti-cancer therapeutics, could allow more selective targeting of cells infiltrating the tumor parenchyma. Yet it is to consider that an accompanying remodeling of the tumor ECM might require additional degradation of the tumorigenic interstitial matrix or optimization of the FL formulation since FL delivery was also restricted by ECM *in vitro* (see 5.2.1). This could be further investigated by a closer view of FL motion in the ECM, e.g., by fluorescence correlation spectroscopy or single-molecule microscopy. Here, one could investigate (restricted) diffusion of FL with modified composition, e.g., by introducing a pH-sensitive PEG-coating, or in combinatorial treatment with ECM-degrading compounds. After optimizing particle diffusion, FL-mediated liposomal tracer dye or drug delivery could be investigated in cells covered with ECM gels with varying mesh size or charged moieties, to obtain additional insights into the diffusivity of FL in the dynamically changing tumor matrix, and ECM in general.

For the passage across intracellularly connected cell layers, FL were shown to increasingly pass through endothelial cell layers *in vitro* if their barrier function was compromised (see 5.3.2),

as observed in tumor-associated vascular remodeling. Overall, the use of FL as drug delivery vehicles in cancer therapy was thus proposed as beneficial over conventionally used liposomal formulations, although additional considerations, such as the previously mentioned optimization of ECM passage, are necessary.

The investigation of FL biodistribution by retro-orbital injection to a murine model further indicated a pulmonary and hepatic accumulation and a potential hepatic clearance (see **5.4.2**). Additionally, a delivery of FL cargo to endothelial cells was proposed, further highlighted by the mediation of antioxidant cargo effects in endothelial cells of the cerebral vasculature *in vivo*. The relevance of FL-mediated endothelial delivery of antioxidants was further supported by the *in vitro* investigation of functional effects in endothelium, focusing on the rescue of the barrier function of dysfunctional endothelial cells (see **5.3.3**). Many radical scavenging antioxidants are deprotonated at physiological pH (239, 240). Thus, future applications of FL are not focusing on weakly basic compounds prone to lysosomal degradation within this application, in contrast to anti-cancer therapy. An application of FL for antioxidant delivery can be expanded to newly emerging antioxidant compounds, e.g., antioxidants with lipid-like aliphatic chains. These could be intercalated into FL with high efficiency and directly inserted into the cell membrane by membrane fusion. Oxidized lipids are ROS derived from membrane lipids, which can promote endothelial dysfunction-related pathophysiologies (241, 242). Thus, a direct localization of antioxidants in the membrane could be of high therapeutic relevance.

Furthermore, the interaction of FL with serum proteins should be investigated more closely since formation of a protein corona was shown to greatly affect immunogenicity and biodistribution of nanoparticles before. The retardation of liposomal tracer dye incorporation by membrane fusion in the presence of serum proteins *in vitro*, as observed in this work (see **5.4.1**), supports a potential protein corona formation of FL as well. Protein corona formation is a rapid and highly dynamic process. The absorption of proteins to the liposomal surface in systemic circulation is energetically favored. Thus, a "soft" protein corona is forming rapidly by absorption of highly abundant proteins. The latter are substituted over time by less frequently observed proteins with high affinity, forming a "hard" protein corona (29, 243). This might not only be relevant for previously mentioned pharmacokinetics of FL, but for the mediation of membrane fusion since protein absorption is proposedly changing the liposomal surface charge, a previously published key determinant of FL-mediated membrane fusion (45). Fusion with endothelial cells also relies on close bilayer contact, and a protein shell around

liposomes could sterically interfere with it. After combining these thoughts with the previously observed retardation of fusion, it is suggested that the formation of a "soft" protein corona still enables fusion due to low affinity of proteins and subsequent dominance of electrostatic attraction of opposed membrane charges, until a "hard" protein corona with high affinity binding forms. However, this theory has to be investigated further. Here, the dynamically changing protein interaction partners in the protein corona could be identified at different time points after serum addition to FL, e.g., by mass spectrometry. The fusion efficiencies of the protein corona obtained at different time points could be further measured by previously mentioned confocal laser-scanning microscopy and subsequent image analysis (see **4.2.4.3**). A time-dependent change of fusogenicity of the protein corona could be of high relevance for endothelial delivery of drugs, since nanoparticle administration is followed by accumulation of these in eliminating organs. A time-dependent formation of a "hard" protein corona that blocks membrane fusion could thus reduce fusion-mediated uptake in cells of eliminating organs and subsequently reduce side effects as well.

8 References

1. Choi yh & Han H-K (2017) Nanomedicines: current status and future perspectives in aspect of drug delivery and pharmacokinetics. *Journal of Pharmaceutical Investigation* 48.
2. Buschmann MD, *et al.* (2021) Nanomaterial Delivery Systems for mRNA Vaccines. *Vaccines* 9(1).
3. Gabizon A, *et al.* (1983) Enhancement of Adriamycin Delivery to Liver Metastatic Cells with Increased Tumorcidal Effect Using Liposomes as Drug Carriers. *Cancer research* 43(10):4730-4735.
4. Gabizon A, *et al.* (1994) Prolonged circulation time and enhanced accumulation in malignant exudates of doxorubicin encapsulated in polyethylene-glycol coated liposomes. *Cancer research* 54(4):987-992.
5. Liebisch G, *et al.* (2020) Update on LIPID MAPS classification, nomenclature, and shorthand notation for MS-derived lipid structures. *Journal of lipid research* 61(12):1539-1555.
6. Jackson CL, Walch L, & Verbavatz JM (2016) Lipids and Their Trafficking: An Integral Part of Cellular Organization. *Dev Cell* 39(2):139-153.
7. Björck ML & Brzezinski P (2018) Control of transmembrane charge transfer in cytochrome c oxidase by the membrane potential. *Nature Communications* 9(1):3187.
8. Fadok VA, Bratton DL, Frasch SC, Warner ML, & Henson PM (1998) The role of phosphatidylserine in recognition of apoptotic cells by phagocytes. *Cell death and differentiation* 5(7):551-562.
9. Ramstedt B & Slotte JP (2006) Sphingolipids and the formation of sterol-enriched ordered membrane domains. *Biochimica et biophysica acta* 1758(12):1945-1956.
10. Suzuki KGN (2012) Lipid rafts generate digital-like signal transduction in cell plasma membranes. *Biotechnology Journal* 7(6):753-761.
11. Monnard PA & Deamer DW (2002) Membrane self-assembly processes: steps toward the first cellular life. *The Anatomical record* 268(3):196-207.
12. Chandler D (2005) Interfaces and the driving force of hydrophobic assembly. *Nature* 437(7059):640-647.
13. Marsh D (2012) Thermodynamics of phospholipid self-assembly. *Biophysical journal* 102(5):1079-1087.
14. Kulkarni CV (2012) Lipid crystallization: from self-assembly to hierarchical and biological ordering. *Nanoscale* 4(19):5779-5791.
15. Hamai C, Yang T, Kataoka S, Cremer PS, & Musser SM (2006) Effect of Average Phospholipid Curvature on Supported Bilayer Formation on Glass by Vesicle Fusion. *Biophysical journal* 90(4):1241-1248.
16. Jouhet J (2013) Importance of the hexagonal lipid phase in biological membrane organization. *Frontiers in plant science* 4:494.
17. Cevc G (1993) *Phospholipids Handbook* (Marcel Dekker, Inc.).
18. Bangham AD & Horne RW (1964) Negative staining of phospholipids and their structural modification by surface-active agents as observed in the electron microscope. *Journal of Molecular Biology* 8(5):660-661.
19. Bangham AD, Standish MM, Watkins JC, & Weissmann G (1967) The Diffusion of Ions from a Phospholipid Model Membrane System. (Springer Vienna), pp 183-187.
20. Bangham AD, Gier J, & Greville GD (1967) Osmotic properties and water permeability of phospholipid liquid crystals. *Chemistry and Physics of Lipids* 1:225-246.

21. Barenholz Y (2012) Doxil®--the first FDA-approved nano-drug: lessons learned. *Journal of controlled release : official journal of the Controlled Release Society* 160(2):117-134.
22. Beltrán-Gracia E, López-Camacho A, Higuera-Ciapara I, Velázquez-Fernández JB, & Vallejo-Cardona AA (2019) Nanomedicine review: clinical developments in liposomal applications. *Cancer Nanotechnology* 10(1):11.
23. Almeida B, Nag OK, Rogers KE, & Delehanty JB (2020) Recent Progress in Bioconjugation Strategies for Liposome-Mediated Drug Delivery. *Molecules (Basel, Switzerland)* 25(23):5672.
24. Munster P, *et al.* (2018) Safety and pharmacokinetics of MM-302, a HER2-targeted antibody-liposomal doxorubicin conjugate, in patients with advanced HER2-positive breast cancer: a phase 1 dose-escalation study. *British journal of cancer* 119(9):1086-1093.
25. Wei Y, *et al.* (2019) Low-toxicity transferrin-guided polymersomal doxorubicin for potent chemotherapy of orthotopic hepatocellular carcinoma in vivo. *Acta biomaterialia* 92:196-204.
26. Matsumura Y, *et al.* (2004) Phase I and pharmacokinetic study of MCC-465, a doxorubicin (DXR) encapsulated in PEG immunoliposome, in patients with metastatic stomach cancer. *Annals of oncology : official journal of the European Society for Medical Oncology* 15(3):517-525.
27. Çağdaş M, Sezer AD, & Bucak S (2014) Liposomes as Potential Drug Carrier Systems for Drug Delivery.).
28. Lombardo D, Calandra P, Caccamo MT, magazù S, & Kiselev M (2019) Colloidal stability of liposomes. *AIMS Materials Science* 6:200-213.
29. Caracciolo G (2015) Liposome–protein corona in a physiological environment: Challenges and opportunities for targeted delivery of nanomedicines. *Nanomedicine: Nanotechnology, Biology and Medicine* 11(3):543-557.
30. Caracciolo G, Pozzi D, Capriotti AL, Cavaliere C, & Laganà A (2013) Effect of DOPE and cholesterol on the protein adsorption onto lipid nanoparticles. *Journal of Nanoparticle Research* 15(3):1498.
31. Bulbake U, Doppalapudi S, Kommineni N, & Khan W (2017) Liposomal Formulations in Clinical Use: An Updated Review. *Pharmaceutics* 9(2).
32. Marsh D, Bartucci R, & Sportelli L (2003) Lipid membranes with grafted polymers: physicochemical aspects. *Biochimica et Biophysica Acta (BBA) - Biomembranes* 1615(1):33-59.
33. Hong R-L, *et al.* (1999) Direct Comparison of Liposomal Doxorubicin with or without Polyethylene Glycol Coating in C-26 Tumor-bearing Mice. *Is Surface Coating with Polyethylene Glycol Beneficial?* 5(11):3645-3652.
34. Greish K (2010) Enhanced permeability and retention (EPR) effect for anticancer nanomedicine drug targeting. *Methods in molecular biology (Clifton, N.J.)* 624:25-37.
35. Saito T, *et al.* (2000) Immune tolerance induced by polyethylene glycol-conjugate of protein antigen: clonal deletion of antigen-specific Th-cells in the thymus. *Journal of biomaterials science. Polymer edition* 11(6):647-656.
36. Kozma GT, *et al.* (2019) Pseudo-anaphylaxis to Polyethylene Glycol (PEG)-Coated Liposomes: Roles of Anti-PEG IgM and Complement Activation in a Porcine Model of Human Infusion Reactions. *ACS nano* 13(8):9315-9324.
37. Giavina-Bianchi P & Kalil J (2019) Polyethylene Glycol Is a Cause of IgE-Mediated Anaphylaxis. *The Journal of Allergy and Clinical Immunology: In Practice* 7(6):1874-1875.

References

38. Nikolaou V, Syrigos K, & Saif MW (2016) Incidence and implications of chemotherapy related hand-foot syndrome. *Expert opinion on drug safety* 15(12):1625-1633.
39. Liu X & Huang G (2013) Formation strategies, mechanism of intracellular delivery and potential clinical applications of pH-sensitive liposomes. *Asian Journal of Pharmaceutical Sciences* 8(6):319-328.
40. Hayashi K, Watanabe M, Iwasaki T, Shudou M, & Uda RM (2019) Endosomal escape by photo-activated fusion of liposomes containing a malachite green derivative: a novel class of photoresponsive liposomes for drug delivery vehicles. *Photochemical & photobiological sciences : Official journal of the European Photochemistry Association and the European Society for Photobiology* 18(6):1471-1478.
41. Csiszar A, *et al.* (2010) Novel fusogenic liposomes for fluorescent cell labeling and membrane modification. *Bioconjugate chemistry* 21(3):537-543.
42. Wiedenhoef T, *et al.* (2019) Fusogenic liposomes effectively deliver resveratrol to the cerebral microcirculation and improve endothelium-dependent neurovascular coupling responses in aged mice. *GeroScience* 41(6):711-725.
43. Wiedenhoef T, *et al.* (2020) The Basement Membrane in a 3D Breast Acini Model Modulates Delivery and Anti-Proliferative Effects of Liposomal Anthracyclines. *Pharmaceuticals (Basel, Switzerland)* 13(9).
44. Kolašinac R, *et al.* (2021) Delivery of the Radionuclide (131)I Using Cationic Fusogenic Liposomes as Nanocarriers. *International journal of molecular sciences* 22(1).
45. Kolašinac R, Kleusch C, Braun T, Merkel R, & Csiszár A (2018) Deciphering the Functional Composition of Fusogenic Liposomes. *International journal of molecular sciences* 19(2).
46. Csiszár A, *et al.* (2015) Resveratrol encapsulated in novel fusogenic liposomes activates Nrf2 and attenuates oxidative stress in cerebromicrovascular endothelial cells from aged rats. *The journals of gerontology. Series A, Biological sciences and medical sciences* 70(3):303-313.
47. Kube S, *et al.* (2017) Fusogenic Liposomes as Nanocarriers for the Delivery of Intracellular Proteins. *Langmuir* 33(4):1051-1059.
48. Hoffmann M, Hersch N, Merkel R, Csiszar A, & Hoffmann B (2019) Changing the Way of Entrance: Highly Efficient Transfer of mRNA and siRNA via Fusogenic Nano-Carriers. *J Biomed Nanotechnol* 15(1):170-183.
49. Braun T (2017) Fusogene und endozytotische Liposomen: Vergleichende Untersuchungen zum Wirkstofftransport am Beispiel von Doxorubicin und Aclacinomycin A. Doctoral Thesis (Rheinische Friedrich-Wilhelms-Universität Bonn, Bonn, Germany).
50. Markin V, Kozlov M, & Borovjagin V (1984) On the theory of membrane fusion. The stalk mechanism. *Gen. Physiol. Biophys* 3(5):361-377.
51. Hong W & Lev S (2014) Tethering the assembly of SNARE complexes. *Trends in cell biology* 24(1):35-43.
52. Siegel DP (1999) The Modified Stalk Mechanism of Lamellar/Inverted Phase Transitions and Its Implications for Membrane Fusion. *Biophysical journal* 76(1):291-313.
53. Chernomordik LV & Kozlov MM (2008) Mechanics of membrane fusion. *Nature structural & molecular biology* 15(7):675-683.
54. Sung H, *et al.* (2021) Global cancer statistics 2020: GLOBOCAN estimates of incidence and mortality worldwide for 36 cancers in 185 countries. *CA: A Cancer Journal for Clinicians*.
55. Klaus Diedrich WH, Walter Jonat, Askan Schultze-Mosgau, Klaus-Theo Schneider, Jürgen Weiss (2007) *Gynäkologie und Geburtshilfe* (Springer) 2 Ed.

56. Oskarsson T (2013) Extracellular matrix components in breast cancer progression and metastasis. *The Breast* 22:S66-S72.
57. Clusan L, Le Goff P, Flouriot G, & Pakdel F (2021) A Closer Look at Estrogen Receptor Mutations in Breast Cancer and Their Implications for Estrogen and Antiestrogen Responses. *International journal of molecular sciences* 22(2).
58. Harbeck N, *et al.* (2019) Breast cancer. *Nature Reviews Disease Primers* 5(1):66.
59. Sporikova Z, Koudelakova V, Trojanec R, & Hajduch M (2018) Genetic Markers in Triple-Negative Breast Cancer. *Clinical Breast Cancer* 18(5):e841-e850.
60. Cuzick J & Baum M (1985) Tamoxifen and contralateral breast cancer. *Lancet (London, England)* 2(8449):282.
61. Richard J, *et al.* (1987) Epidermal-Growth-Factor Receptor Status as Predictor of Early Recurrence of and Death From Breast Cancer. *The Lancet* 329(8547):1398-1402.
62. Hicklin DJ & Ellis LM (2005) Role of the vascular endothelial growth factor pathway in tumor growth and angiogenesis. *Journal of clinical oncology : official journal of the American Society of Clinical Oncology* 23(5):1011-1027.
63. Petersen OW, Rønnov-Jessen L, Howlett AR, & Bissell MJ (1992) Interaction with basement membrane serves to rapidly distinguish growth and differentiation pattern of normal and malignant human breast epithelial cells. *Proceedings of the National Academy of Sciences of the United States of America* 89(19):9064-9068.
64. Debnath J, Muthuswamy SK, & Brugge JS (2003) Morphogenesis and oncogenesis of MCF-10A mammary epithelial acini grown in three-dimensional basement membrane cultures. *Methods (San Diego, Calif.)* 30(3):256-268.
65. Gaiko-Shcherbak A, *et al.* (2021) Cell Force-Driven Basement Membrane Disruption Fuels EGF- and Stiffness-Induced Invasive Cell Dissemination from Benign Breast Gland Acini. *International journal of molecular sciences* 22(8):3962.
66. Minchinton AI & Tannock IF (2006) Drug penetration in solid tumours. *Nature reviews. Cancer* 6(8):583-592.
67. Casey TM, *et al.* (2008) Cancer associated fibroblasts stimulated by transforming growth factor beta1 (TGF-beta 1) increase invasion rate of tumor cells: a population study. *Breast cancer research and treatment* 110(1):39-49.
68. Acerbi I, *et al.* (2015) Human breast cancer invasion and aggression correlates with ECM stiffening and immune cell infiltration. *Integrative Biology* 7(10):1120-1134.
69. Winkler J, Abisoye-Ogunniyan A, Metcalf KJ, & Werb Z (2020) Concepts of extracellular matrix remodelling in tumour progression and metastasis. *Nature Communications* 11(1):5120.
70. Schenk S, *et al.* (2003) Binding to EGF receptor of a laminin-5 EGF-like fragment liberated during MMP-dependent mammary gland involution. *The Journal of cell biology* 161(1):197-209.
71. Zeng Z-S, Cohen AM, & Guillem JG (1999) Loss of basement membrane type IV collagen is associated with increased expression of metalloproteinases 2 and 9 (MMP-2 and MMP-9) during human colorectal tumorigenesis. *Carcinogenesis* 20(5):749-755.
72. Sun X, *et al.* (2017) Elevated heparanase expression is associated with poor prognosis in breast cancer: a study based on systematic review and TCGA data. *Oncotarget* 8(26).
73. Yurchenco PD, Cheng YS, & Colognato H (1992) Laminin forms an independent network in basement membranes. *The Journal of cell biology* 117(5):1119-1133.
74. Howat WJ, Holmes JA, Holgate ST, & Lackie PM (2001) Basement membrane pores in human bronchial epithelium: a conduit for infiltrating cells? *The American journal of pathology* 158(2):673-680.

References

75. Hironaka K, Makino H, Yamasaki Y, & Ota Z (1993) Pores in the Glomerular Basement Membrane Revealed by Ultrahigh- Resolution Scanning Electron Microscopy. *Nephron* 64(4):647-649.
76. Naylor RW, Morais MRPT, & Lennon R (2021) Complexities of the glomerular basement membrane. *Nature Reviews Nephrology* 17(2):112-127.
77. Ogston AG (1958) The spaces in a uniform random suspension of fibres. *Transactions of the Faraday Society* 54(0):1754-1757.
78. Brenner BM, Hostetter TH, & Humes HD (1978) Glomerular permselectivity: barrier function based on discrimination of molecular size and charge. *American Journal of Physiology-Renal Physiology* 234(6):F455-F460.
79. Lawrence MG, *et al.* (2017) Permeation of macromolecules into the renal glomerular basement membrane and capture by the tubules. *Proceedings of the National Academy of Sciences of the United States of America* 114(11):2958-2963.
80. Caulfield JP & Farquhar MG (1974) The permeability of glomerular capillaries to graded dextrans. Identification of the basement membrane as the primary filtration barrier. *The Journal of cell biology* 63(3):883-903.
81. Harvey SJ, *et al.* (2007) Disruption of glomerular basement membrane charge through podocyte-specific mutation of agrin does not alter glomerular permselectivity. *The American journal of pathology* 171(1):139-152.
82. Lieleg O, Baumgärtel RM, & Bausch AR (2009) Selective filtering of particles by the extracellular matrix: an electrostatic bandpass. *Biophysical journal* 97(6):1569-1577.
83. Thorne RG, Lakkaraju A, Rodriguez-Boulan E, & Nicholson C (2008) In vivo diffusion of lactoferrin in brain extracellular space is regulated by interactions with heparan sulfate. *Proceedings of the National Academy of Sciences of the United States of America* 105(24):8416-8421.
84. Rennke HG & Venkatachalam MA (1977) Glomerular permeability: in vivo tracer studies with polyanionic and polycationic ferritins. *Kidney international* 11(1):44-53.
85. Bolton GR, Deen WM, & Daniels BS (1998) Assessment of the charge selectivity of glomerular basement membrane using Ficoll sulfate. *American Journal of Physiology-Renal Physiology* 274(5):F889-F896.
86. Stylianopoulos T, *et al.* (2010) Diffusion of particles in the extracellular matrix: the effect of repulsive electrostatic interactions. *Biophysical journal* 99(5):1342-1349.
87. Zhang X, Hansing J, Netz Roland R, & DeRouchey Jason E (2015) Particle Transport through Hydrogels Is Charge Asymmetric. *Biophysical journal* 108(3):530-539.
88. Siegel RL, Miller KD, & Jemal A (2019) Cancer statistics, 2019. *CA: A Cancer Journal for Clinicians* 69(1):7-34.
89. Kelley LC, *et al.* (2019) Adaptive F-Actin Polymerization and Localized ATP Production Drive Basement Membrane Invasion in the Absence of MMPs. *Developmental Cell* 48(3):313-328.e318.
90. Iivanainen E, *et al.* (2003) Angiopoietin-regulated recruitment of vascular smooth muscle cells by endothelial-derived heparin binding EGF-like growth factor. *FASEB journal : official publication of the Federation of American Societies for Experimental Biology* 17(12):1609-1621.
91. Hellstrom M, Kaln M, Lindahl P, Abramsson A, & Betsholtz C (1999) Role of PDGF-B and PDGFR-beta in recruitment of vascular smooth muscle cells and pericytes during embryonic blood vessel formation in the mouse. *Development* 126(14):3047-3055.
92. Folkman J & D'Amore PA (1996) Blood Vessel Formation: What Is Its Molecular Basis? *Cell* 87(7):1153-1155.

93. Goumans MJ, *et al.* (2002) Balancing the activation state of the endothelium via two distinct TGF-beta type I receptors. *The EMBO journal* 21(7):1743-1753.
94. Tucker WD, Mahajan, K. (2020) *Anatomy, Blood Vessels* (StatPearls Publishing).
95. Lüllmann-Rauch L (2003) *Taschenlehrbuch Histologie* (Georg Thieme Verlag) 3 Ed.
96. Pugsley MK & Tabrizchi R (2000) The vascular system: An overview of structure and function. *Journal of Pharmacological and Toxicological Methods* 44(2):333-340.
97. Corada M, *et al.* (2001) Monoclonal antibodies directed to different regions of vascular endothelial cadherin extracellular domain affect adhesion and clustering of the protein and modulate endothelial permeability. *Blood* 97(6):1679-1684.
98. Bazzoni G (2006) Endothelial tight junctions: permeable barriers of the vessel wall. *Thrombosis and haemostasis* 95 1:36-42.
99. Parthasarathi K, *et al.* (2006) Connexin 43 mediates spread of Ca²⁺-dependent proinflammatory responses in lung capillaries. *The Journal of clinical investigation* 116(8):2193-2200.
100. Schmidt VJ, Wölfle SE, Boettcher M, & de Wit C (2008) Gap junctions synchronize vascular tone within the microcirculation. *Pharmacological reports : PR* 60(1):68-74.
101. Hirase T, *et al.* (1997) Occludin as a possible determinant of tight junction permeability in endothelial cells. *Journal of cell science* 110 (Pt 14):1603-1613.
102. Gavard J & Gutkind JS (2006) VEGF controls endothelial-cell permeability by promoting the beta-arrestin-dependent endocytosis of VE-cadherin. *Nature cell biology* 8(11):1223-1234.
103. Gavard J & Gutkind JS (2008) VE-cadherin and claudin-5: it takes two to tango. *Nature cell biology* 10(8):883-885.
104. Taddei A, *et al.* (2008) Endothelial adherens junctions control tight junctions by VE-cadherin-mediated upregulation of claudin-5. *Nature cell biology* 10(8):923-934.
105. Kevil CG, Payne DK, Mire E, & Alexander JS (1998) Vascular permeability factor/vascular endothelial cell growth factor-mediated permeability occurs through disorganization of endothelial junctional proteins. *The Journal of biological chemistry* 273(24):15099-15103.
106. Michel CC & Neal CR (1999) Openings through endothelial cells associated with increased microvascular permeability. *Microcirculation (New York, N.Y. : 1994)* 6(1):45-54.
107. Petit V & Thiery JP (2000) Focal adhesions: structure and dynamics. *Biology of the cell* 92(7):477-494.
108. Rüegg C & Mariotti A (2003) Vascular integrins: pleiotropic adhesion and signaling molecules in vascular homeostasis and angiogenesis. *Cellular and molecular life sciences : CMLS* 60(6):1135-1157.
109. Li S, *et al.* (1997) Fluid shear stress activation of focal adhesion kinase. Linking to mitogen-activated protein kinases. *The Journal of biological chemistry* 272(48):30455-30462.
110. Wang G, Tiemeier GL, van den Berg BM, & Rabelink TJ (2020) Endothelial Glycocalyx Hyaluronan: Regulation and Role in Prevention of Diabetic Complications. *The American journal of pathology* 190(4):781-790.
111. Potenza MA, Gagliardi S, Nacci C, Carratu MR, & Montagnani M (2009) Endothelial dysfunction in diabetes: from mechanisms to therapeutic targets. *Current medicinal chemistry* 16(1):94-112.

References

112. Moncada S, Higgs EA, & Vane JR (1977) Human arterial and venous tissues generate prostacyclin (prostaglandin x), a potent inhibitor of platelet aggregation. *Lancet (London, England)* 1(8001):18-20.
113. Kumar R & Boim MA (2009) Diversity of pathways for intracellular angiotensin II synthesis. *Current opinion in nephrology and hypertension* 18(1):33-39.
114. Macarthur H, Warner TD, Wood EG, Corder R, & Vane JR (1994) Endothelin-1 release from endothelial cells in culture is elevated both acutely and chronically by short periods of mechanical stretch. *Biochemical and biophysical research communications* 200(1):395-400.
115. Jaffe EA, Hoyer LW, & Nachman RL (1974) Synthesis of von Willebrand factor by cultured human endothelial cells. *Proceedings of the National Academy of Sciences of the United States of America* 71(5):1906-1909.
116. Brodsky SV, Malinowski K, Golightly M, Jesty J, & Goligorsky MS (2002) Plasminogen activator inhibitor-1 promotes formation of endothelial microparticles with procoagulant potential. *Circulation* 106(18):2372-2378.
117. Reddy KG, Nair RN, Sheehan HM, & Hodgson JM (1994) Evidence that selective endothelial dysfunction may occur in the absence of angiographic or ultrasound atherosclerosis in patients with risk factors for atherosclerosis. *Journal of the American College of Cardiology* 23(4):833-843.
118. Konukoglu D & Uzun H (2017) Endothelial Dysfunction and Hypertension. *Advances in experimental medicine and biology* 956:511-540.
119. Shi Y, *et al.* (2016) Rapid endothelial cytoskeletal reorganization enables early blood-brain barrier disruption and long-term ischaemic reperfusion brain injury. *Nature Communications* 7(1):10523.
120. Muoio V, Persson PB, & Sendeski MM (2014) The neurovascular unit - concept review. *Acta physiologica (Oxford, England)* 210(4):790-798.
121. Incalza MA, *et al.* (2018) Oxidative stress and reactive oxygen species in endothelial dysfunction associated with cardiovascular and metabolic diseases. *Vascular pharmacology* 100:1-19.
122. Corcoran A & Cotter TG (2013) Redox regulation of protein kinases. *The FEBS journal* 280(9):1944-1965.
123. Salminen A, Kaarniranta K, & Kauppinen A (2013) Crosstalk between Oxidative Stress and SIRT1: Impact on the Aging Process. *International journal of molecular sciences* 14(2):3834-3859.
124. Takahashi N, Kozai D, Kobayashi R, Ebert M, & Mori Y (2011) Roles of TRPM2 in oxidative stress. *Cell calcium* 50(3):279-287.
125. Sahoo N, Hoshi T, & Heinemann SH (2014) Oxidative modulation of voltage-gated potassium channels. *Antioxidants & redox signaling* 21(6):933-952.
126. Klotz LO, *et al.* (2015) Redox regulation of FoxO transcription factors. *Redox biology* 6:51-72.
127. Vomund S, Schäfer A, Parnham MJ, Brüne B, & von Knethen A (2017) Nrf2, the Master Regulator of Anti-Oxidative Responses. *International journal of molecular sciences* 18(12).
128. Lipowsky HH & Lescanic A (2013) The effect of doxycycline on shedding of the glycocalyx due to reactive oxygen species. *Microvascular research* 90:80-85.
129. Singh A, *et al.* (2013) Reactive oxygen species modulate the barrier function of the human glomerular endothelial glycocalyx. *PLoS One* 8(2):e55852.

130. Foster RR, *et al.* (2013) Glycosaminoglycan regulation by VEGFA and VEGFC of the glomerular microvascular endothelial cell glycocalyx in vitro. *The American journal of pathology* 183(2):604-616.
131. Duval M, Le Boeuf F, Huot J, & Gratton JP (2007) Src-mediated phosphorylation of Hsp90 in response to vascular endothelial growth factor (VEGF) is required for VEGF receptor-2 signaling to endothelial NO synthase. *Molecular biology of the cell* 18(11):4659-4668.
132. Ushio-Fukai M (2007) VEGF signaling through NADPH oxidase-derived ROS. *Antioxidants & redox signaling* 9(6):731-739.
133. Chang J & Chaudhuri O (2019) Beyond proteases: Basement membrane mechanics and cancer invasion. *The Journal of cell biology* 218(8):2456-2469.
134. Presta LG, *et al.* (1997) Humanization of an anti-vascular endothelial growth factor monoclonal antibody for the therapy of solid tumors and other disorders. *Cancer research* 57(20):4593-4599.
135. Ferrara N, Hillan KJ, Gerber HP, & Novotny W (2004) Discovery and development of bevacizumab, an anti-VEGF antibody for treating cancer. *Nature reviews. Drug discovery* 3(5):391-400.
136. Lu L, *et al.* (2009) The anti-cancer drug lenalidomide inhibits angiogenesis and metastasis via multiple inhibitory effects on endothelial cell function in normoxic and hypoxic conditions. *Microvascular research* 77(2):78-86.
137. Koldehoff M, Beelen DW, & Elmaagacli AH (2014) Inhibition of mTOR with everolimus and silencing by vascular endothelial cell growth factor-specific siRNA induces synergistic antitumor activity in multiple myeloma cells. *Cancer gene therapy* 21(7):275-282.
138. Schlumberger M, *et al.* (2015) Lenvatinib versus placebo in radioiodine-refractory thyroid cancer. *The New England journal of medicine* 372(7):621-630.
139. Kurasawa M, *et al.* (2009) Regulation of tight junction permeability by sodium caprate in human keratinocytes and reconstructed epidermis. *Biochemical and biophysical research communications* 381(2):171-175.
140. Del Vecchio G, *et al.* (2012) Sodium Caprate Transiently Opens Claudin-5-Containing Barriers at Tight Junctions of Epithelial and Endothelial Cells. *Molecular Pharmaceutics* 9(9):2523-2533.
141. Preston E, Slinn J, Vinokourov I, & Stanimirovic D (2008) Graded reversible opening of the rat blood-brain barrier by intracarotid infusion of sodium caprate. *Journal of neuroscience methods* 168(2):443-449.
142. Warren K, *et al.* (2006) Phase II trial of intravenous lobradimil and carboplatin in childhood brain tumors: a report from the Children's Oncology Group. *Cancer chemotherapy and pharmacology* 58(3):343-347.
143. Lyons D, Roy S, Patel M, Benjamin N, & Swift CG (1997) Impaired nitric oxide-mediated vasodilatation and total body nitric oxide production in healthy old age. *Clinical science (London, England : 1979)* 93(6):519-525.
144. Novella S, *et al.* (2013) Aging enhances contraction to thromboxane A2 in aorta from female senescence-accelerated mice. *Age (Dordrecht, Netherlands)* 35(1):117-128.
145. Yoon HJ, Cho SW, Ahn BW, & Yang SY (2010) Alterations in the activity and expression of endothelial NO synthase in aged human endothelial cells. *Mechanisms of Ageing and Development* 131(2):119-123.

References

146. Donato AJ, *et al.* (2007) Direct evidence of endothelial oxidative stress with aging in humans: relation to impaired endothelium-dependent dilation and upregulation of nuclear factor-kappaB. *Circulation research* 100(11):1659-1666.
147. Ungvari Z, *et al.* (2008) Dysregulation of mitochondrial biogenesis in vascular endothelial and smooth muscle cells of aged rats. *American journal of physiology. Heart and circulatory physiology* 294(5):H2121-2128.
148. Chen B, Lu Y, Chen Y, & Cheng J (2015) The role of Nrf2 in oxidative stress-induced endothelial injuries. *The Journal of endocrinology* 225(3):R83-99.
149. Xu C, *et al.* (2020) SIRT1 is downregulated by autophagy in senescence and ageing. *Nature cell biology* 22(10):1170-1179.
150. Shang YJ, *et al.* (2009) Radical-scavenging activity and mechanism of resveratrol-oriented analogues: influence of the solvent, radical, and substitution. *The Journal of organic chemistry* 74(14):5025-5031.
151. Ungvari Z, *et al.* (2009) Resveratrol attenuates mitochondrial oxidative stress in coronary arterial endothelial cells. *American journal of physiology. Heart and circulatory physiology* 297(5):H1876-1881.
152. Cantó C, *et al.* (2009) AMPK regulates energy expenditure by modulating NAD⁺ metabolism and SIRT1 activity. *Nature* 458(7241):1056-1060.
153. Lagouge M, *et al.* (2006) Resveratrol Improves Mitochondrial Function and Protects against Metabolic Disease by Activating SIRT1 and PGC-1 β . *Cell* 127(6):1109-1122.
154. Toth P, *et al.* (2014) Resveratrol treatment rescues neurovascular coupling in aged mice: role of improved cerebrovascular endothelial function and downregulation of NADPH oxidase. *American journal of physiology. Heart and circulatory physiology* 306(3):H299-308.
155. Walle T (2011) Bioavailability of resveratrol. *Annals of the New York Academy of Sciences* 1215:9-15.
156. Bonkowski MS & Sinclair DA (2016) Slowing ageing by design: the rise of NAD(+) and sirtuin-activating compounds. *Nature reviews. Molecular cell biology* 17(11):679-690.
157. Hickson LJ, *et al.* (2019) Senolytics decrease senescent cells in humans: Preliminary report from a clinical trial of Dasatinib plus Quercetin in individuals with diabetic kidney disease. *EBioMedicine* 47:446-456.
158. Schneider CA, Rasband WS, & Eliceiri KW (2012) NIH Image to ImageJ: 25 years of image analysis. *Nature Methods* 9(7):671-675.
159. Schindelin J, *et al.* (2012) Fiji: an open-source platform for biological-image analysis. *Nat Methods* 9(7):676-682.
160. Szoka F & Papahadjopoulos D (1980) Comparative Properties and Methods of Preparation of Lipid Vesicles (Liposomes). *Annual review of biophysics and bioengineering* 9:467-508.
161. Stetefeld J, McKenna SA, & Patel TR (2016) Dynamic light scattering: a practical guide and applications in biomedical sciences. *Biophysical Reviews* 8(4):409-427.
162. Lowry GV, *et al.* (2016) Guidance to improve the scientific value of zeta-potential measurements in nanoEHS. *Environmental Science: Nano* 3(5):953-965.
163. Farid M, Faber T, Dietrich D, & Lamprecht A (2020) Cell membrane fusing liposomes for cytoplasmic delivery in brain endothelial cells. *Colloids and surfaces. B, Biointerfaces* 194:111193.
164. Soule HD, *et al.* (1990) Isolation and characterization of a spontaneously immortalized human breast epithelial cell line, MCF-10. *Cancer research* 50(18):6075-6086.

165. Gaiko-Shcherbak A, *et al.* (2015) The Acinar Cage: Basement Membranes Determine Molecule Exchange and Mechanical Stability of Human Breast Cell Acini. *PLoS One* 10(12):e0145174.
166. Pal M, *et al.* (2019) Epithelial-mesenchymal transition of cancer cells using bioengineered hybrid scaffold composed of hydrogel/3D-fibrous framework. *Scientific reports* 9(1):8997.
167. Chavez KJ, Garimella SV, & Lipkowitz S (2010) Triple negative breast cancer cell lines: one tool in the search for better treatment of triple negative breast cancer. *Breast disease* 32(1-2):35-48.
168. Ayala A, Muñoz MF, & Argüelles S (2014) Lipid Peroxidation: Production, Metabolism, and Signaling Mechanisms of Malondialdehyde and 4-Hydroxy-2-Nonenal. *Oxidative Medicine and Cellular Longevity* 2014:360438.
169. Pardillo-Díaz R, Carrascal L, Ayala A, & Nunez-Abades P (2015) Oxidative stress induced by cumene hydroperoxide evokes changes in neuronal excitability of rat motor cortex neurons. *Neuroscience* 289:85-98.
170. Kolašinac R, *et al.* (2019) Influence of Environmental Conditions on the Fusion of Cationic Liposomes with Living Mammalian Cells. *Nanomaterials (Basel, Switzerland)* 9(7).
171. Hersch N, *et al.* (2013) The constant beat: cardiomyocytes adapt their forces by equal contraction upon environmental stiffening. *Biology Open* 2(3):351-361.
172. Huff J (2015) The Airyscan detector from ZEISS: confocal imaging with improved signal-to-noise ratio and super-resolution. *Nature Methods* 12(12):i-ii.
173. Toth P, *et al.* (2015) IGF-1 deficiency impairs neurovascular coupling in mice: implications for cerebrovascular aging. *Aging cell* 14(6):1034-1044.
174. Tarantini S, *et al.* (2015) Pharmacologically-induced neurovascular uncoupling is associated with cognitive impairment in mice. *Journal of cerebral blood flow and metabolism : official journal of the International Society of Cerebral Blood Flow and Metabolism* 35(11):1871-1881.
175. Tarantini S, *et al.* (2017) Demonstration of impaired neurovascular coupling responses in TG2576 mouse model of Alzheimer's disease using functional laser speckle contrast imaging. *GeroScience* 39(4):465-473.
176. Heeman W, Steenbergen W, Dam G, & Boerma C (2019) Clinical applications of laser speckle contrast imaging: a review. *Journal of Biomedical Optics* 24:1.
177. Dunn AK, Bolay H, Moskowitz MA, & Boas DA (2001) Dynamic imaging of cerebral blood flow using laser speckle. *Journal of cerebral blood flow and metabolism : official journal of the International Society of Cerebral Blood Flow and Metabolism* 21(3):195-201.
178. Mostany R & Portera-Cailliau C (2008) A craniotomy surgery procedure for chronic brain imaging. *Journal of visualized experiments : JoVE* (12).
179. Mostany R & Portera-Cailliau C (2008) A method for 2-photon imaging of blood flow in the neocortex through a cranial window. *Journal of visualized experiments : JoVE* (12).
180. Wilhelm S, *et al.* (2016) Analysis of nanoparticle delivery to tumours. *Nature Reviews Materials* 1(5):16014.
181. Strom SC & Michalopoulos G (1982) [29] Collagen as a substrate for cell growth and differentiation. *Methods in Enzymology*, (Academic Press), Vol 82, pp 544-555.
182. Rodgers LS, Beam MT, Anderson JM, & Fanning AS (2013) Epithelial barrier assembly requires coordinated activity of multiple domains of the tight junction protein ZO-1. *Journal of cell science* 126(7):1565-1575.

References

183. Zenebergh A, Baurain R, & Trouet A (1982) Cellular pharmacokinetics of aclacinomycin A in cultured L1210 cells. Comparison with daunorubicin and doxorubicin. *Cancer chemotherapy and pharmacology* 8(2):243-249.
184. Hu Y-B, Dammer EB, Ren R-J, & Wang G (2015) The endosomal-lysosomal system: from acidification and cargo sorting to neurodegeneration. *Translational Neurodegeneration* 4(1):18.
185. Alves C, *et al.* (2017) Influence of doxorubicin on model cell membrane properties: Insights from in vitro and in silico studies. *Scientific reports* 7.
186. Norinder U, Tuck A, Norgren K, & Munic Kos V (2020) Existing highly accumulating lysosomotropic drugs with potential for repurposing to target COVID-19. *Biomedicine & Pharmacotherapy* 130:110582.
187. Binaschi M, *et al.* (1998) Human DNA topoisomerase II α -dependent DNA cleavage and yeast cell killing by anthracycline analogues. *Cancer research* 58(9):1886-1892.
188. Doroshow JH (1983) Effect of anthracycline antibiotics on oxygen radical formation in rat heart. *Cancer research* 43(2):460-472.
189. Sato S, Iwaizumi M, Handa K, & Tamura Y (1977) Electron spin resonance study on the mode of generation of free radicals of daunomycin, adriamycin, and carboquone in NAD(P)H-microsome system. *Gan* 68(5):603-608.
190. Dong J, *et al.* (1995) Difference between the resistance mechanisms of aclacinomycin- and adriamycin-resistant P388 cell lines. *Oncol Res* 7(5):245-252.
191. Frolov VA, Dunina-Barkovskaya AY, Samsonov AV, & Zimmerberg J (2003) Membrane permeability changes at early stages of influenza hemagglutinin-mediated fusion. *Biophysical journal* 85(3):1725-1733.
192. Frankfurt OS (1980) Flow cytometric analysis of double-stranded RNA content distributions. *The journal of histochemistry and cytochemistry : official journal of the Histochemistry Society* 28(7):663-669.
193. Invitrogen (2010) Chapter 8: Nucleic Acid Detection and Analysis. *The Molecular Probes Handbook*, (ThermoFisher Scientific), 11 Ed.
194. Paine PL, Moore LC, & Horowitz SB (1975) Nuclear envelope permeability. *Nature* 254(5496):109-114.
195. Mukherjee P, Nathamgari SSP, Kessler JA, & Espinosa HD (2018) A Combined Numerical and Experimental Investigation of Localized Electroporation-based Transfection and Sampling. *bioRxiv*:346981.
196. Rieger AM, Hall BE, Luong LT, Schang LM, & Barreda DR (2010) Conventional apoptosis assays using propidium iodide generate a significant number of false positives that prevent accurate assessment of cell death. *Journal of Immunological Methods* 358(1):81-92.
197. Yang C, Tabatabaei SN, Ruan X, & Hardy P (2017) The Dual Regulatory Role of MiR-181a in Breast Cancer. *Cellular Physiology and Biochemistry* 44(3):843-856.
198. Li Y, *et al.* (2015) miR-181a-5p Inhibits Cancer Cell Migration and Angiogenesis via Downregulation of Matrix Metalloproteinase-14. *Cancer research* 75(13):2674-2685.
199. Seddon JM (1990) Structure of the inverted hexagonal (HII) phase, and non-lamellar phase transitions of lipids. *Biochimica et Biophysica Acta (BBA) - Reviews on Biomembranes* 1031(1):1-69.
200. Noordam PC, van Echteld CJ, de Kruijff B, Verkleij AJ, & de Gier J (1980) Barrier characteristics of membrane model systems containing unsaturated phosphatidylethanolamines. *Chem Phys Lipids* 27(3):221-232.

201. Gozen I & Dommersnes P (2014) Pore dynamics in lipid membranes. *The European Physical Journal Special Topics* 223(9):1813-1829.
202. McNeil PL & Steinhardt RA (1997) Loss, restoration, and maintenance of plasma membrane integrity. *The Journal of cell biology* 137(1):1-4.
203. Mattei B, Lira RB, Perez KR, & Riske KA (2017) Membrane permeabilization induced by Triton X-100: The role of membrane phase state and edge tension. *Chemistry and Physics of Lipids* 202:28-37.
204. Mesa-Galloso H, Pedrera L, & Ros U (2021) Pore-forming proteins: From defense factors to endogenous executors of cell death. *Chem Phys Lipids* 234:105026.
205. Shillcock JC & Lipowsky R (2005) Tension-induced fusion of bilayer membranes and vesicles. *Nature materials* 4(3):225-228.
206. Kliesch T-T, *et al.* (2017) Membrane tension increases fusion efficiency of model membranes in the presence of SNAREs. *Scientific reports* 7(1):12070.
207. Wang M, *et al.* (2018) Sonoporation-induced cell membrane permeabilization and cytoskeleton disassembly at varied acoustic and microbubble-cell parameters. *Scientific reports* 8(1):3885.
208. Liu Y, *et al.* (2001) Ultrasound-Induced Hyperthermia Increases Cellular Uptake and Cytotoxicity of P-Glycoprotein Substrates in Multi-Drug Resistant Cells. *Pharmaceutical Research* 18:1255-1261.
209. Chauhan V, Stylianopoulos T, Boucher Y, & Jain R (2011) Delivery of Molecular and Nanoscale Medicine to Tumors: Transport Barriers and Strategies. *Annual review of chemical and biomolecular engineering* 2:281-298.
210. Pilz M, *et al.* (2020) Transport of nanoprobe in multicellular spheroids. *Nanoscale* 12(38):19880-19887.
211. Venugopal MG, Ramshaw JA, Braswell E, Zhu D, & Brodsky B (1994) Electrostatic interactions in collagen-like triple-helical peptides. *Biochemistry* 33(25):7948-7956.
212. Lieleg O, Vladescu I, & Ribbeck K (2010) Characterization of particle translocation through mucin hydrogels. *Biophysical journal* 98(9):1782-1789.
213. Wang H-X, *et al.* (2016) Surface charge critically affects tumor penetration and therapeutic efficacy of cancer nanomedicines. *Nano Today* 11(2):133-144.
214. Labouta HI, *et al.* (2018) Surface-grafted polyethylene glycol conformation impacts the transport of PEG-functionalized liposomes through a tumour extracellular matrix model. *RSC Advances* 8(14):7697-7708.
215. Zinger A, *et al.* (2019) Collagenase Nanoparticles Enhance the Penetration of Drugs into Pancreatic Tumors. *ACS nano* 13(10):11008-11021.
216. Goodman TT, Olive PL, & Pun SH (2007) Increased nanoparticle penetration in collagenase-treated multicellular spheroids. *International journal of nanomedicine* 2(2):265-274.
217. Yatvin M, Kreutz W, Horwitz B, & Shinitzky M (1980) pH-sensitive liposomes: possible clinical implications. *Science* 210(4475):1253-1255.
218. Kale AA & Torchilin VP (2007) Design, synthesis, and characterization of pH-sensitive PEG-PE conjugates for stimuli-sensitive pharmaceutical nanocarriers: the effect of substitutes at the hydrazone linkage on the pH stability of PEG-PE conjugates. *Bioconjugate chemistry* 18(2):363-370.
219. Roy R, Yang J, & Moses MA (2009) Matrix metalloproteinases as novel biomarkers and potential therapeutic targets in human cancer. *Journal of clinical oncology : official journal of the American Society of Clinical Oncology* 27(31):5287-5297.

References

220. Wang Y, *et al.* (2015) A Prodrug-type, MMP-2-targeting Nanoprobe for Tumor Detection and Imaging. *Theranostics* 5(8):787-795.
221. Akers WJ, *et al.* (2012) Detection of MMP-2 and MMP-9 activity in vivo with a triple-helical peptide optical probe. *Bioconjugate chemistry* 23(3):656-663.
222. Hu J-J, Liu L-H, Li Z-Y, Zhuo R-X, & Zhang X-Z (2016) MMP-responsive theranostic nanoplatform based on mesoporous silica nanoparticles for tumor imaging and targeted drug delivery. *Journal of Materials Chemistry B* 4(11):1932-1940.
223. Tauro JR, Lee BS, Lateef SS, & Gemeinhart RA (2008) Matrix metalloprotease selective peptide substrates cleavage within hydrogel matrices for cancer chemotherapy activation. *Peptides* 29(11):1965-1973.
224. Hippenstiel S, *et al.* (1998) VEGF induces hyperpermeability by a direct action on endothelial cells. *The American journal of physiology* 274(5):L678-684.
225. Nagy JA, *et al.* (2006) Permeability properties of tumor surrogate blood vessels induced by VEGF-A. *Laboratory Investigation* 86(8):767-780.
226. Lampugnani MG, Orsenigo F, Gagliani MC, Tacchetti C, & Dejana E (2006) Vascular endothelial cadherin controls VEGFR-2 internalization and signaling from intracellular compartments. *The Journal of cell biology* 174(4):593-604.
227. Li L, *et al.* (2015) The effect of the size of fluorescent dextran on its endocytic pathway. *Cell biology international* 39(5):531-539.
228. Poisson J, *et al.* (2017) Liver sinusoidal endothelial cells: Physiology and role in liver diseases. *Journal of Hepatology* 66(1):212-227.
229. Campbell RB, *et al.* (2002) Cationic Charge Determines the Distribution of Liposomes between the Vascular and Extravascular Compartments of Tumors. *Cancer research* 62(23):6831-6836.
230. Abra RM & Hunt CA (1981) Liposome disposition in vivo. III. Dose and vesicle-size effects. *Biochimica et biophysica acta* 666(3):493-503.
231. Hirn S, *et al.* (2011) Particle size-dependent and surface charge-dependent biodistribution of gold nanoparticles after intravenous administration. *Eur J Pharm Biopharm* 77(3):407-416.
232. Roberts MS, Magnusson BM, Burczynski FJ, & Weiss M (2002) Enterohepatic circulation: physiological, pharmacokinetic and clinical implications. *Clinical pharmacokinetics* 41(10):751-790.
233. Zhu N, Liggitt D, Liu Y, & Debs R (1993) Systemic gene expression after intravenous DNA delivery into adult mice. *Science* 261(5118):209-211.
234. Song YK & Liu D (1998) Free liposomes enhance the transfection activity of DNA/lipid complexes in vivo by intravenous administration. *Biochimica et Biophysica Acta (BBA) - Biomembranes* 1372(1):141-150.
235. Ishiwata H, Suzuki N, Ando S, Kikuchi H, & Kitagawa T (2000) Characteristics and biodistribution of cationic liposomes and their DNA complexes. *Journal of controlled release : official journal of the Controlled Release Society* 69(1):139-148.
236. Carroll RG (2007) 8 - Vascular System. *Elsevier's Integrated Physiology*, ed Carroll RG (Mosby, Philadelphia), pp 77-89.
237. Haluska CK, *et al.* (2006) Time scales of membrane fusion revealed by direct imaging of vesicle fusion with high temporal resolution. *Proceedings of the National Academy of Sciences* 103(43):15841-15846.
238. Montagne A, *et al.* (2015) Blood-brain barrier breakdown in the aging human hippocampus. *Neuron* 85(2):296-302.

-
239. Lemańska K, *et al.* (2001) The influence of pH on antioxidant properties and the mechanism of antioxidant action of hydroxyflavones. *Free Radical Biology and Medicine* 31(7):869-881.
240. Tyrakowska B, *et al.* (1999) TEAC antioxidant activity of 4-hydroxybenzoates. *Free radical biology & medicine* 27(11-12):1427-1436.
241. Zhong S, *et al.* (2019) An update on lipid oxidation and inflammation in cardiovascular diseases. *Free Radical Biology and Medicine* 144:266-278.
242. Pratt DA, Tallman KA, & Porter NA (2011) Free radical oxidation of polyunsaturated lipids: New mechanistic insights and the development of peroxy radical clocks. *Accounts of chemical research* 44(6):458-467.
243. Ke PC, Lin S, Parak WJ, Davis TP, & Caruso F (2017) A Decade of the Protein Corona. *ACS nano* 11(12):11773-11776.

9 **Figures**

Figure 3.1. Representatives of lipid categories as proposed by the Lipid Metabolites and Pathways Strategy (LIPID MAPS) consortium.....	3
Figure 3.2. Schematic lipid assembly in lamellar and hexagonal phases.	4
Figure 3.3. Different functionalizations of liposomes for drug delivery and diagnostics.	6
Figure 3.4. Schematic representation of fusogenic liposomes (FL).....	8
Figure 3.5. Proposed stalk mechanism of lipid bilayer fusion.....	9
Figure 3.6. Comparison of cellular cargo uptake mediated by membrane fusion or endocytosis.	10
Figure 3.7. Anatomy of the human mammary gland.	11
Figure 3.8. Schematic representation of endothelial junctions to adjacent cells, the extracellular matrix, and the glycocalyx.....	17
Figure 3.9. Schematic representation of reactive origin species (ROS) generation and scavenging.	20
Figure 4.1. Preparation of liposomes.....	35
Figure 4.2. Exemplary size and zeta potential distribution plots of fusogenic liposomes (FL) and pegylated, endocytic liposomes (PEG-EL) are shown.....	37
Figure 4.3. Plots of calibration measurements of fluorescence intensities of doxorubicin (DOX), propidium iodide (PI), aclacinomycin a (ACL) and resveratrol (RSV).	38
Figure 4.4. Differentiation process of MCF 10A acini during cell cultivation on a Geltrex bed, derived from single MCF 10A cells.	43
Figure 4.5. Setup of the endothelial barrier model.....	44
Figure 4.6. Working principle of the EdU incorporation assay used for the quantification of proliferating cells in MCF 10A acini after anthracycline treatment.	49
Figure 4.7. The reaction of the CM-H₂DCFDA general oxidative stress indicator after cellular uptake.....	51
Figure 4.8. Schematic workflow of laser speckle contrast imaging.....	53

Figure 4.9. Jablonski diagram with a combined schematic view of single-photon and two-photon excitation.	55
Figure 5.1. Uptake of membrane-impermeable propidium iodide (PI) by MCF 10A cells using fusogenic liposomes (FL).....	59
Figure 5.2. Formulation-independent localization of the anthracyclines aclacinomycin a (ACL) and doxorubicin (DOX).	61
Figure 5.3. Anti-proliferative effects of the anthracyclines aclacinomycin a (ACL) and doxorubicin (DOX) in different formulations in MCF 10A cells.....	62
Figure 5.4. Penetration of fusogenic liposomes containing DiR or DiI after indicated incubation times, after administration onto a gel layer of Geltrex and collagen I.	65
Figure 5.5. Formation of MCF 10A acini and MDA-MB-231 spheroids on a Geltrex bed, cultured for 10 or 9 days, respectively.....	66
Figure 5.6. MCF 10A acini with or without EGF treatment and a MDA-MB-231 spheroid after FL treatment.....	67
Figure 5.7. Collagen IV and laminin 332 secretion of MDA-MB-231 cells cultured on a Geltrex bed.	67
Figure 5.8. Interaction of fusogenic and endocytic liposomes with the basement membrane of low- (ld) and high-developed (hd) MCF 10A acini.	68
Figure 5.9. Analysis of median DiR fluorescence intensity in cells of low- (ld) or high-developed (hd) MCF 10A acini and subsequent treatment with fusogenic liposomes (FL) or pegylated endocytic liposomes (PEG-EL).....	69
Figure 5.10. Digestion of the basement membrane by collagenase IV (C4ase) of an MCF 10A acinus with a high-developed basement membrane is shown.....	70
Figure 5.11. Anti-proliferative effects of the anthracyclines aclacinomycin a (ACL) and doxorubicin (DOX) in different formulations in the low-developed MCF 10A acini model.	71
Figure 5.12. Anti-proliferative effects of the anthracycline doxorubicin (DOX) in different formulations in the high-developed MCF 10A acini model.....	72
Figure 5.13. Barrier function of primary human umbilical vein endothelial cells (HUVECs).....	74

Figure 5.14. Permeability of a primary HUVECs after ROS induction and VEGF stimulation.....	75
Figure 5.15. Delivery of resveratrol (RSV) to primary human umbilical vein endothelial cells (HUVECs).....	78
Figure 5.16. Influence of fetal bovine serum (FBS) on the fusion of fusogenic liposomes (FL) with primary human umbilical vein endothelial cells (HUVECs).....	80
Figure 5.17. Intensity measurement of liposomal tracer dye DiD in murine tissue after repetitive treatment with fusogenic liposomes.....	81
Figure 5.18. Localization of liposomal tracer dyes in the murine brain.....	82
Figure 5.19. Localization of liposomal tracer dye DiD in the murine brain.....	83
Figure 5.20. Cerebral blood flow (CBF) response of mice after somatosensory stimulation.....	85

10 Tables

Table 4.1. Lipids, lipid derivatives and dyes, and liposomal cargo.....	26
Table 4.2. Excitation wavelengths and emission ranges for the fluorophores measured with a spectrometer for entrapment efficiency determination.	38
Table 4.3. Excitation wavelengths and emission ranges for the fluorophores detected with confocal laser-scanning microscopy in 4.2.3.1.	41
Table 4.4. Excitation wavelengths and emission ranges for the fluorophores detected with confocal laser-scanning microscopy in 4.2.3.2.	43
Table 4.5. Excitation wavelengths and emission ranges for the fluorophores detected with confocal laser-scanning microscopy in 4.2.3.3.	45
Table 4.6. Excitation wavelengths and emission ranges for the fluorophores detected with confocal laser-scanning microscopy in 4.2.4.2.	47
Table 4.7. Excitation wavelengths and emission ranges for the fluorophores detected with confocal laser-scanning microscopy in 4.2.4.3.	48
Table 4.8. Excitation wavelengths and bandpass filters for the fluorophores detected with confocal laser-scanning microscopy in 4.2.5.1.	49
Table 4.9. Bandpass filters used for fluorophores in intravital imaging.	55
Table 5.1. Liposome characterization of fusogenic liposomes after loading with 1.5 μ M PI or unloaded liposomes.	58
Table 5.2. Liposome characterization of FL and PEG-EL after encapsulation of 0.6 μ M ACL and 1.8 μ M DOX or unloaded liposomes.....	61
Table 5.3. Liposome characterization of FL after encapsulation of RSV or unloaded liposomes.	77

11 List of publications

Wiedenhoef T, et al. (2019) Fusogenic liposomes effectively deliver resveratrol to the cerebral microcirculation and improve endothelium-dependent neurovascular coupling responses in aged mice. *GeroScience* 41(6):711-725. (DOI: 10.1007/s11357-019-00102-1)

Wiedenhoef T, et al. (2020) The Basement Membrane in a 3D Breast Acini Model Modulates Delivery and Anti-Proliferative Effects of Liposomal Anthracyclines. *Pharmaceuticals (Basel, Switzerland)* 13(9). (DOI: 10.3390/ph13090256)